

# **Tuning The Electronic Structure and Reactivity of Oxidized Chromium Salen Nitride Complexes**

**by**

**Warren VandeVen**

B.Sc., University of the Fraser Valley, 2020

Thesis Submitted in Partial Fulfillment of the  
Requirements for the Degree of  
Master of Science

in the  
Department of Chemistry  
Faculty of Science

© Warren VandeVen 2023  
SIMON FRASER UNIVERSITY  
Summer 2023

Copyright in this work is held by the author. Please ensure that any reproduction or re-use is done in accordance with the relevant national copyright legislation.

## Declaration of Committee

**Name:** Warren VandeVen

**Degree:** Master of Science (Chemistry)

**Title:** Tuning The Electronic Structure and Reactivity of Oxidized Chromium Salen Nitride Complexes

**Committee:**

**Chair:** Corina Andreoiu  
Professor, Chemistry

**Tim Storr**  
Supervisor  
Professor, Chemistry

**Daniel Leznoff**  
Committee Member  
Professor, Chemistry

**Jeffrey Warren**  
Committee Member  
Associate Professor, Chemistry

**Byron Gates**  
Examiner  
Professor, Chemistry

## Abstract

Transition metal nitride ( $N^{3-}$ ) complexes exhibit useful reactivity towards heteroatom transfer, as well as providing valuable insight into the mechanisms of dinitrogen reduction and ammonia oxidation. Salen ligands are capable of forming complexes with a large number of metal ions in different oxidation states and are thus a versatile platform in coordination chemistry research. By incorporating salen ligands with a variety of R-group substituents at the *para* position of the phenolate moieties, the electronic structure and thus the reactivity of the nitride ligand can be modified. This thesis will focus on the synthesis, characterization and reactivity of Cr nitride complexes bearing modified salen ligands (R =  $NO_2$ ,  $CF_3$ ,  $tBu$ ,  $OMe$ ,  $O^iPr$ ,  $NMe_2$ , and  $NEt_2$ ). Salen ligands are well-known for their ability to form ligand radicals upon oxidation, as opposed to metal-based oxidation. Oxidation of  $CrNSal^{NMe_2}$  and  $CrNSal^{NEt_2}$  yields  $Cr^V$  ligand radical species, whereas the other less donating R-groups yield high-valent  $Cr^{VI}$  nitride complexes. Oxidized complexes were characterized by both experimental and theoretical techniques including UV-vis-NIR spectroscopy, electron paramagnetic resonance spectroscopy, electrochemistry, and density functional theory calculations. Depending on the locus of oxidation, desirable reactivity may be observed such as C-H bond activation. The addition of exogenous ligands may further activate the nitride ligand and facilitate homocoupling or C-H bond activation pathways.

**Keywords:** nitride; salen; Cr; electronic structure; C-H bond activation

## Acknowledgements

Wow, it's been a long journey to get here today. Who knew that a teenager in Grade 11 wanting to study languages would have ended up becoming a chemistry master's degree holder? In between, he studied to be a pharmacist, had to change plans when things didn't work out, and decided to push forward and complete a Bachelor of Science degree majoring in biology and minoring in chemistry. Finally, he decided to take a step back and pursue a career teaching in high school after everything is said and done. We'll see what's next!

In order to get through these challenging years following graduation from secondary school, I have many people to thank. My parents John and Lisa were a huge part of my success during my time at University of the Fraser Valley and Simon Fraser University. I am lucky to have such supportive parents that let me live with them (and come back home after I lived in Burnaby for a year), which saved me a great deal of financial stress as well as time. Their encouragement to pursue further education made it a lot easier to pursue my passions, even if they couldn't understand what I was doing!

The rest of my family also played a role in getting me to where I am today. My brothers Travis and Spencer were always game to go fishing or play music, helping me to catch a break from the lab. My grandparents also pushed me to pursue further education, but I think they also just liked to tell their friends that they had a grandson who was doing a chemistry master's degree. Many of my aunts and uncles were also there to provide emotional support along the way and their care does not go unnoticed.

I also have many employers and professors to thank. Roy Groothof from Groothof Trucking employed me for 5 years greasing trucks on Saturdays, helping me pay for my schooling and saving money. While it wasn't easy and didn't relate to my studies, it helped me get my head out of the books and develop the grit needed for graduate school. Alex Yousif at Neova Technologies also employed me for two co-op work terms where I worked as a biology R&D lab technician. I learned a lot at this job about having a good work ethic and had a lot of responsibility despite being a student. I felt like a valuable member of the team and was able to get a glimpse of how science operates at the industrial level performing pilot scale experiments. Saurabh Chitnis at Dalhousie University hosted me as an Inorganic Chemistry Exchange student in summer 2020 when COVID-19 started. It

was so frustrating for both of us, as I was supposed to head to Halifax, but the restrictions for entering the Atlantic provinces were strict and changing every day. While I unfortunately never made it to Nova Scotia, he was very flexible with alternative plans and trained me to perform computational chemistry, which would later become extremely important during my M.Sc. degree. Linus Chiang at University of the Fraser Valley initiated my journey to becoming a chemist when he first hired me for a research work-study job one summer. I would later do a co-op work term and independent study course with him and he was instrumental in getting me my master's degree position at Simon Fraser University. He also hosted me at UFV when I was working with Saurabh during the Inorganic Chemistry Exchange program, so I was still able to do some synthetic chemistry with antimony and bismuth complexes. I've never met anyone with as much passion for chemistry as him, and I have a great deal of respect for him as both a chemist and a person. Even though I didn't publish any work with him while I was in his lab, I've had the pleasure of collaborating with him during my masters and it is always great to see him again.

I also owe many people at SFU thanks, especially my masters supervisor Tim Storr for his guidance and extracurricular activities he let me pursue. I was able to complete the certificate program in university teaching and learning during my degree, which led me to eventually pursue teaching career. In addition, he sent me to France for two months to work with Fabrice Thomas and Olivier Jarjayes studying ammonia oxidation with nickel and manganese carbenes. They were great to work with, and I met so many other nice people there who made me feel very welcome. I lived in a British Columbia bubble most of my life, and I was able to travel to France, Germany, Austria, Spain and Italy in the trip of a lifetime. Other Storr group students that deserve special thanks are Nick, Khrystyna and Sam who trained me on various instruments and DFT, as well as Diego, Romain, Calvin, Mark, Lauryn and Omar who were always great to shoot the breeze with at coffee time. Best wishes to all of them wherever they go.

To top it all off, I even managed to find someone to settle down with, my fiancée Brittany during the last year of my masters. I wish I would have found her sooner, but I think I would have been too distracted to get much research or homework done. She has become a huge support to me and makes me happy, even when it seems like my research is a total mess, and has been supportive of my educational endeavours. It was so hard leaving her when I was in France, but I can't wait to spend the rest of my life with her.

# Table of Contents

Declaration of Committee .....	ii
Abstract .....	iii
Acknowledgements .....	iv
Table of Contents .....	vi
List of Tables .....	ix
List of Figures .....	x
List of Acronyms and Abbreviations .....	xvi
<b>Chapter 1. Introduction .....</b>	<b>1</b>
1.1. Overview of Transition Metal Nitrides .....	1
1.2. Bonding in TM Nitride Complexes .....	3
1.3. Reactivity and Stability of Nitride Complexes .....	5
1.3.1. Early Transition Metal Nitrides .....	5
1.3.2. Late Transition Metal Nitrides .....	8
1.4. Redox-Active Ligands and Salens .....	9
1.5. Cr Salen Complexes .....	15
1.6. Thesis Outline .....	18
<b>Chapter 2. Synthesis and Characterization of Neutral CrNSal<sup>R</sup> Complexes (R = NO<sub>2</sub>, H, OMe, O<sup>i</sup>Pr, NEt<sub>2</sub>) .....</b>	<b>19</b>
2.1. Introduction .....	19
2.2. Results .....	21
2.2.1. General Strategies for H <sub>2</sub> Sal <sup>R</sup> Synthesis .....	21
2.2.2. General Strategies for CrNSal <sup>R</sup> Synthesis .....	22
2.2.3. Solid-state Structures .....	23
2.2.4. Electron Paramagnetic Resonance .....	28
2.2.5. Electronic Absorption Spectroscopy .....	30
2.2.6. Theoretical Analysis .....	32
2.3. Conclusion .....	33
2.4. Experimental .....	34
2.4.1. Materials .....	34
2.4.2. Instrumentation .....	34
2.4.3. Syntheses .....	34
2.4.4. X-ray Structure Determination .....	36
2.4.5. Theoretical Analysis .....	37
<b>Chapter 3. Electronic Structure of [CrSal<sup>R</sup>N]<sup>+</sup> (R = NO<sub>2</sub>, H, <sup>t</sup>Bu, OMe, O<sup>i</sup>Pr, NEt<sub>2</sub>) .....</b>	<b>38</b>
3.1. Introduction .....	38
3.2. Results .....	40
3.2.1. Electrochemistry .....	40
3.2.2. Electronic Absorption Spectroscopy .....	45
3.2.3. Electron Paramagnetic Resonance .....	48

3.2.4.	Solution Infrared Spectroscopy .....	51
3.2.5.	Theoretical Analysis .....	52
3.3.	Conclusion.....	56
3.4.	Experimental .....	57
3.4.1.	Materials .....	57
3.4.2.	Instrumentation .....	57
3.4.3.	Synthesis of [CrNSal <sup>R</sup> ] <sup>+</sup> .....	57
3.4.4.	Theoretical Analysis .....	57
<b>Chapter 4.</b>	<b>Reactivity of [CrNSal<sup>R</sup>]<sup>+</sup> (R = <sup>t</sup>Bu, NMe<sub>2</sub>) Towards Exogenous Ligands and C-H Bond Activation .....</b>	<b>59</b>
4.1.	Introduction.....	59
4.2.	Results .....	62
4.2.1.	Electronic Absorption Spectroscopy with Ligands .....	62
4.2.2.	GC-MS Headspace Analysis .....	65
4.2.3.	Theoretical Analysis with Exogenous Ligands.....	66
4.2.4.	Electronic Absorption Spectroscopy with Xanthene.....	69
4.2.5.	Mass Spectrometry of Reaction Between [CrNSal <sup>R</sup> ] <sup>+</sup> and Xanthene.....	70
4.3.	Conclusion.....	73
4.4.	Experimental .....	74
4.4.1.	Materials .....	74
4.4.2.	Instrumentation .....	74
4.4.3.	UV-vis-NIR Monitored Reaction of [CrNSal <sup>R</sup> ] <sup>+</sup> with Exogenous Ligands .....	74
4.4.4.	GC-MS Headspace Analysis .....	75
4.4.5.	UV-vis-NIR Monitored Reaction of [CrNSal <sup>R</sup> ] <sup>+</sup> with Xanthene .....	75
4.4.6.	Theoretical Analysis .....	75
<b>Chapter 5.</b>	<b>Future Directions .....</b>	<b>76</b>
5.1.	Introduction.....	76
5.2.	Novel R-Group Substituents and Valence Tautomerism .....	76
5.2.1.	Synthesis of R = N=Bn Derivative .....	76
	Synthesis of 2-(tert-butyl)-6-(1,3-dioxolan-2-yl)-4-nitrophenol .....	77
	Synthesis of 4-amino-2-(tert-butyl)-6-(1,3-dioxolan-2-yl)phenol .....	78
5.2.2.	Synthesis of R = NPh Derivative.....	78
	Synthesis of 2-(benzyloxy)-5-bromo-3-(tert-butyl)benzaldehyde .....	79
5.3.	Ligand Accelerated C-H Bond Activation and Homocoupling.....	80
5.3.1.	Reactivity Studies Using UV-vis-NIR and GC-MS .....	80
5.3.2.	Homocoupling and C-H Bond Activation .....	82
5.4.	Conclusion.....	83
<b>References</b>	.....	<b>85</b>
<b>Appendix A.</b>	<b>Supporting Information for Chapter 2.....</b>	<b>97</b>
<b>Appendix B.</b>	<b>Supporting Information for Chapter 3.....</b>	<b>99</b>

<b>Appendix C. Supporting Information for Chapter 4.....</b>	<b>104</b>
<b>Appendix D. Supporting Information for Chapter 5.....</b>	<b>106</b>



## List of Tables

Table 2.1.	Key crystallographic information for CrNSal <sup>NO2</sup> , CrNSal <sup>CF3</sup> , CrNSal <sup>H-</sup> , CrNSal <sup>OMe</sup> and CrNSal <sup>OiPr</sup> .....	27
Table 2.2.	Full instrumentation details for EPR analysis of CrNSal <sup>R</sup> (R = NO <sub>2</sub> , H, OMe, O <sup>i</sup> Pr, NEt <sub>2</sub> ).....	29
Table 2.3.	Key UV-vis-NIR spectroscopic information for CrNSal <sup>R</sup> .....	31
Table 2.4.	Predicted and experimental (parentheses) coordination sphere bond lengths (Å) for CrNSal <sup>R</sup> . Refer to Figures 2.5-2.9 for atom numbering scheme. ....	32
Table 3.1.	Tabulated redox potentials for CrNSal <sup>R</sup> vs Fc <sup>+</sup> /Fc in volts. Peak-to-peak separation in parentheses. Only the first two redox events (as applicable) are included. ....	42
Table 3.2.	$\Delta E_{ox}$ and $K_c$ values for obtained from differential pulse voltammetry.....	45
Table 3.3.	Key UV-vis-NIR data for [CrNSal <sup>R</sup> ] <sup>+</sup> .....	47
Table 3.4.	Full instrumentation details for EPR analysis of [CrNSal <sup>R</sup> ] <sup>+</sup> (R = NO <sub>2</sub> , H, OMe, O <sup>i</sup> Pr, NEt <sub>2</sub> ). ....	50
Table 3.5.	Relative energies of different spin states for [CrNSal <sup>R</sup> ] <sup>+</sup> (kcal/mol). ....	53
Table 3.6.	Predicted coordination sphere bond lengths (Å) for [CrNSal <sup>R</sup> ] <sup>+</sup> . Changes from neutral to oxidized (oxidized – neutral) in parentheses. Refer to Table 2.4 for neutral metrics, and to Figures 2.5-2.9 for atom numbering scheme. Ligand radical metrics obtained from BSS state.....	54
Table 3.7.	Predicted change ( $\Delta$ ) in Cr≡N Stretch Frequencies (cm <sup>-1</sup> ) upon oxidation of CrNSal <sup>R</sup> to [CrNSal <sup>R</sup> ] <sup>+</sup> . ....	55
Table 4.1.	Predicted coordination sphere bond lengths (Å) for [CrNSal <sup>tBu</sup> ] <sup>+</sup> and ligand adducts. Changes from [CrNSal <sup>tBu</sup> ] <sup>+</sup> on ligand coordination (adduct – free complex) in parentheses. ....	67
Table 4.2.	Additional geometric information for [CrNSal <sup>tBu</sup> ] <sup>+</sup> -L coordination sphere. ....	68
Table 4.3.	Cr≡N Bonding Metrics for [CrNSal <sup>tBu</sup> ] <sup>+</sup> -L.....	68
Table 4.4.	Reaction energetics for the interaction between oxidized CrNSal <sup>tBu</sup> and pyridine, chloride and bromide ligands. ....	69

## List of Figures

Figure 1.1.	Haber Bosch process for ammonia production from H <sub>2</sub> and N <sub>2</sub> gas. <sup>19</sup> .....	1
Figure 1.2.	Nitrogenase enzyme and MoFe active site of dinitrogen fixation (orange = Fe; blue = Mo; grey = C) (A). <sup>21,22</sup> Transition metal complexes such as Schrock's Molybdenum catalyst (left) and Peter's Fe catalyst (right) can mimic this reactivity (B). <sup>25,26</sup> .....	2
Figure 1.3.	Fe and Ru molecular transition metal catalysts and their respective catalytic TON for the ammonia oxidation reaction. <sup>33,35,36</sup> .....	3
Figure 1.4.	Simplified MO diagram for a d <sup>0</sup> transition metal nitride complex with a nucleophilic nitride ligand. <sup>40</sup> .....	4
Figure 1.5.	Gray and Winkler's "oxo wall." Early transition metal nitrides of Groups 3-8 are stable and isolable, whereas late transition metal nitrides are transient species.....	5
Figure 1.6.	Potassium bridged Ti <sup>IV</sup> complex containing terminal nitride ligands. <sup>42-44</sup> The nitride ligand is nucleophilic and reacts with a variety of electrophiles such as methyl iodide. ....	5
Figure 1.7.	Nucleophilic reactivity of Cr <sup>V</sup> nitride ligands towards boranes and late transition metals. <sup>50,51</sup> .....	6
Figure 1.8.	Shi <i>et al.</i> 's tetraamido cyclic Mn nitride complex that is reactive towards phosphine nucleophiles (A). <sup>53</sup> Meng <i>et al.</i> 's Re PNP pincer nitride complex that catalyzes ammonia oxidation (B). <sup>55</sup> .....	7
Figure 1.9.	First stable terminal Fe nitride complex synthesized by Betley and Peters (A). <sup>63</sup> Ambiphilic reactivity of an Os nitride pincer complex. Electrophilic substrates such as silyl halides as well as nucleophilic phosphines react at the nitride (B). <sup>65</sup> .....	8
Figure 1.10.	Stability of late transition metal nitride complexes. Photolysis of Co(I) azido complexes yields ligand insertion products(A). <sup>69</sup> Ni pincer azido complexes form unstable nitride intermediates that perform ligand insertion after photolysis (B). <sup>70</sup> Rh(IV) and Ir(IV) complexes are unstable and homocouple to release N <sub>2</sub> gas (C). <sup>72,73</sup> .....	9
Figure 1.11.	Oxidation of transition metal complexes containing redox-active ligands can yield high-valent metals or ligand radicals. ....	9
Figure 1.12.	Heme active sites in cytochrome P450 visualized using PyMOL (A). <sup>22,82</sup> The Fe <sup>IV</sup> radical cation performs the oxygen insertion step of the catalytic cycle (B). <sup>81</sup> .....	10
Figure 1.13.	Active site of galactose oxidase visualized using PyMOL (A). <sup>22,83</sup> Galactose oxidase catalyzes the oxidation of primary alcohols to aldehydes utilizing ligand radical intermediates (B). <sup>84,90</sup> .....	11
Figure 1.14.	Select examples of salen ligands and their synthesis. Salen ligands are formed from the condensation reaction between a diamine and 2 equivalents of salicylaldehyde (A). The <i>para</i> and <i>ortho</i> groups can be substituted with one or more different R-groups to form symmetric or asymmetric ligands (B). <sup>91</sup> Different backbones can be used to enforce different electronics or geometries to the metal center (C). <sup>92</sup> .....	12

Figure 1.15.	Redox-active properties and electronic structures observed in transition metal salen complexes. Metal identity can influence the degree of ligand radical delocalization (A). <sup>100,101</sup> Cu salen complexes exhibit temperature-induced valence tautomerism between ligand radical and metal oxidized states (B). <sup>102</sup> Exogenous ligand coordination can trigger a change in locus of oxidation from ligand radical to metal oxidized in some Ni salen complexes (C). <sup>100</sup> .....	13
Figure 1.16.	The locus of oxidation depends on the <i>para</i> substituent for transition metal salen complexes. Cu salen complexes undergo ligand-based oxidation for electron-donating groups (A) and metal oxidation for withdrawing groups (B). <sup>102,104</sup> .....	14
Figure 1.17.	MnNSal <sup>R</sup> complexes previously synthesized in the Storr group. The electron-donating strength of the R-group influences the locus of oxidation. <sup>106,107</sup> .....	14
Figure 1.18.	Homocoupling decay for [Mn <sup>VI</sup> NSal <sup>R</sup> ] <sup>+</sup> (R = <sup>t</sup> Bu, CF <sub>3</sub> ) to yield N <sub>2</sub> gas and [Mn <sup>III</sup> Sal] <sup>+</sup> . <sup>106,107</sup> .....	15
Figure 1.19.	Chromium analog of Jacobsen's catalyst for the epoxidation of alkenes. <sup>113</sup> .....	16
Figure 1.20.	Previously synthesized and characterized chromium salen nitride complexes. <sup>108</sup> The R-group substituent on the phenolate ring dictates the locus of oxidation. ....	16
Figure 1.21.	Reactivity of [Cr <sup>VI</sup> NSal <sup>R</sup> ] <sup>+</sup> (R = CF <sub>3</sub> , <sup>t</sup> Bu) (A) and [CrNSal <sup>NMe2</sup> ] <sup>•+</sup> (B) towards Lewis acidic boranes and Lewis basic phosphines. <sup>108</sup> High valent metals are electrophilic and react with phosphines, whereas ligand radicals are nucleophilic and react with boranes.....	17
Figure 1.22.	Target chromium salen nitrides with Hammett parameter values of the different <i>para</i> phenolate substituents.....	18
Figure 2.1.	Synthetic route to transition metal nitride complexes. Photolysis of azido ligands results in the metal nitride and release of N <sub>2</sub> gas (A). <sup>120</sup> Reaction of MnClSal in ammonium hydroxide with bleach oxidizes ammonial ligands to nitrides (B). <sup>122,123</sup> Nitrides can be transferred from one metal complex to another (C). <sup>127,128,128,130</sup> .....	20
Figure 2.2.	Intermetal N-atom transfer scheme developed by Birk & Bendix to generate a labile [CrN <sup>V</sup> ] <sup>2+</sup> fragment (highlighted in purple). <sup>127</sup> Chelating ligands such as salens, pyrrolidinedithiocarbamate and acetylacetonate will displace weakly coordinated ligands to form Cr <sup>V</sup> nitride complexes.....	21
Figure 2.3.	Synthetic route and $\sigma_p$ values of R-group substituents for target salen ligands. ....	22
Figure 2.4.	Synthetic routes to target CrNSal <sup>R</sup> complexes. Either a [CrN] <sup>2+</sup> fragment can be generated <i>in situ</i> and reacted with substituted salen ligand (A), or the CrSal <sup>R</sup> Cl intermediate can be synthesized and reacted with the nitride transfer reagent (B). <sup>127,129</sup> .....	23
Figure 2.5.	XRD structure of CrNSal <sup>NO2</sup> visualized using POV-Ray. Thermal ellipsoids shown at 50% probability level. Hydrogen atoms omitted for clarity. Cr, pink; C grey; O, red; N, blue. Select interatomic distances [Å] and angles [deg]: Cr(1)-O1: 1.910(2), Cr(1)-O(2): 1.906(2), Cr(1)-N(1): 2.015(3), Cr(1)-N(2): 2.002(3), Cr(1)-N(3): 1.560(4), O(1)-C(1): 1.314(4), O(2)-C(2):	

- 1.314(4). Angles: O(1)-Cr(1)-O(2): 89.1(5), O(1)-Cr(1)-N(1): 88.0(6), O(1)-Cr(1)-N(2): 152.4(4), O(1)-Cr(1)-N(3): 104.8(7), O(2)-Cr(1)-N(2): 89.2(7), O(2)-Cr(1)-N(1): 149.3(9), O(2)-Cr(1)-N(3): 107.6(8), N(1)-Cr(1)-N(2): 79.5(0), N(1)-Cr(1)-N(3): 102.4(7), N(2)-Cr(1)-N(3): 101.8(0). .....24
- Figure 2.6. XRD structure of CrNSal<sup>CF3</sup> visualized using POV-Ray. Thermal ellipsoids shown at 50% probability level. Hydrogen atoms omitted for clarity. Cr, pink; C grey; O, red; N, blue. Select interatomic distances [Å] and angles [deg]: Cr(1)-O1: 1.909(2), Cr(1)-O(2): 1.910(2), Cr(1)-N(1): 2.021(3), Cr(1)-N(2): 2.010(3), Cr(1)-N(3): 1.539(3), O(1)-C(1): 1.309(4), O(2)-C(2): 1.307(5). Angles: O(1)-Cr(1)-O(2): 89.3(6), O(1)-Cr(1)-N(1): 87.6(2), O(1)-Cr(1)-N(2): 153.3(9), O(1)-Cr(1)-N(3): 104.5(8), O(2)-Cr(1)-N(2): 88.4(6), O(2)-Cr(1)-N(1): 146.1(7), O(2)-Cr(1)-N(3): 110.0(3), N(1)-Cr(1)-N(2): 79.6(4), N(1)-Cr(1)-N(3): 103.2(8), N(2)-Cr(1)-N(3): 101.0(5). .....25
- Figure 2.7. XRD structure of CrNSal<sup>H</sup> visualized using POV-Ray. Thermal ellipsoids shown at 50% probability level. Hydrogen atoms omitted for clarity. Cr, pink; C grey; O, red; N, blue; F, green. Select interatomic distances [Å] and angles [deg]: Cr(1)-O1: 1.896(1), Cr(1)-O(2): 1.915(1), Cr(1)-N(1): 2.008(1), Cr(1)-N(2): 2.031(1), Cr(1)-N(3): 1.549(2), O(1)-C(1): 1.317(2), O(2)-C(2): 1.316(2). Angles: O(1)-Cr(1)-O(2): 87.8(1), O(1)-Cr(1)-N(1): 88.3(5), O(1)-Cr(1)-N(2): 141.5(8), O(1)-Cr(1)-N(3): 111.9(3), O(2)-Cr(1)-N(2): 88.7(7), O(2)-Cr(1)-N(1): 156.4(7), O(2)-Cr(1)-N(3): 104.5(7), N(1)-Cr(1)-N(2): 79.9(7), N(1)-Cr(1)-N(3): 98.3(8), N(2)-Cr(1)-N(3): 105.9(7). 25
- Figure 2.8. XRD structure of CrNSal<sup>OMe</sup> visualized using POV-Ray. Thermal ellipsoids shown at 50% probability level. Hydrogen atoms omitted for clarity. Cr, pink; C grey; O, red; N, blue. Select interatomic distances [Å] and angles [deg]: Cr(1)-O1: 1.907(3), Cr(1)-O(2): 1.911(3), Cr(1)-N(1): 2.010(3), Cr(1)-N(2): 2.006(5), Cr(1)-N(3): 1.556(5), O(1)-C(1): 1.317(5), O(2)-C(2): 1.318(6). Angles: O(1)-Cr(1)-O(2): 89.5(1), O(1)-Cr(1)-N(1): 88.6(3), O(1)-Cr(1)-N(2): 147.0(8), O(1)-Cr(1)-N(3): 108.9(8), O(2)-Cr(1)-N(2): 86.7(6), O(2)-Cr(1)-N(1): 152.7(4), O(2)-Cr(1)-N(3): 105.0(4), N(1)-Cr(1)-N(2): 80.2(2), N(1)-Cr(1)-N(3): 101.2(1), N(2)-Cr(1)-N(3): 103.5(5). .....26
- Figure 2.9. XRD structure of CrNSal<sup>O<sup>i</sup>Pr</sup> visualized using POV-Ray. Thermal ellipsoids shown at 50% probability level. Hydrogen atoms omitted for clarity. Cr, pink; C grey; O, red; N, blue; F, green. Select interatomic distances [Å] and angles [deg]: Cr(1)-O1: 1.839(6), Cr(1)-O(2): 1.823(6), Cr(1)-N(1): 2.036(6), Cr(1)-N(2): 2.051(6), Cr(1)-N(3): 1.538(1), O(1)-C(1): 1.340(9), O(2)-C(2): 1.340(9). Angles: O(1)-Cr(1)-O(2): 92.0(2), O(1)-Cr(1)-N(1): 89.9(6), O(1)-Cr(1)-N(2): 153.5(5), O(1)-Cr(1)-N(3): 101.3(8), O(2)-Cr(1)-N(2): 89.9(8), O(2)-Cr(1)-N(1): 157.8(6), O(2)-Cr(1)-N(3): 98.5(0), N(1)-Cr(1)-N(2): 78.7(5), N(1)-Cr(1)-N(3): 102.7(1), N(2)-Cr(1)-N(3): 104.3(9). .....26
- Figure 2.10. Frozen EPR spectra for CrNSal<sup>R</sup> where R = NO<sub>2</sub>, H (black = experiment, red = simulated). Conditions: T = 77 K; 0.45 mM complex; 0.1 M TBAP. See Table 2.1 for full instrumentation details, g-values and hyperfine couplings. ....28
- Figure 2.11. Frozen EPR spectra for CrNSal<sup>R</sup> where R = OMe, O<sup>i</sup>Pr, NEt<sub>2</sub> (black = experiment, red = simulated). Conditions: T = 77 K; 0.45 mM complex; 0.1 M TBAP. See Table 2.1 for full instrumentation details, g-values and hyperfine couplings. ....29

Figure 2.12.	UV-vis-NIR spectra for CrNSal <sup>NO<sub>2</sub></sup> , CrNSal <sup>CF<sub>3</sub></sup> , CrNSal <sup>H</sup> and CrNSal <sup>tBu</sup> . Inset is zoomed in view of <i>d</i> → <i>d</i> transitions. Conditions: 0.45 mM complex; T = 253 K; CH <sub>2</sub> Cl <sub>2</sub> .....	30
Figure 2.13.	UV-vis-NIR spectra for CrNSal <sup>OMe</sup> , CrNSal <sup>OiPr</sup> , CrNSal <sup>NMe<sub>2</sub></sup> and CrNSal <sup>NEt<sub>2</sub></sup> . Inset is zoomed in view of the <i>d</i> → <i>d</i> transition (note that for R = NMe <sub>2</sub> and NEt <sub>2</sub> , the <i>d</i> → <i>d</i> transition is likely hidden by the broad LMCT band). Conditions: 0.45 mM complex; T = 253 K; CH <sub>2</sub> Cl <sub>2</sub> . ....	31
Figure 2.14.	Spin density (top) and SOMO (bottom) plots for CrNSal <sup>NEt<sub>2</sub></sup> . All R-group derivatives exhibit similar plots (Figures A1-A4). ....	33
Figure 3.1.	Examples of mixed-valence species. Class II species such as Crowan's biferrrocene cannot readily exchange electrons between metal centers (A). <sup>154,155</sup> Class III species such as the Taube ion have fully delocalized electronic structures and metal center oxidation states are indistinguishable (B). <sup>156,157</sup> .....	39
Figure 3.2.	Oxidation of Cr <sup>V</sup> NSal <sup>R</sup> will yield high-valent metal [Cr <sup>VI</sup> NSal <sup>R</sup> ] <sup>+</sup> or ligand radical [Cr <sup>V</sup> NSal <sup>R</sup> ] <sup>•+</sup> complexes depending on the <i>para</i> R-group substituent. ....	39
Figure 3.3.	Potential Robin-Day classifications for ligand radical salen complexes. No coupling occurs between the aromatic rings for Class I (A). Limited coupling occurs between the aromatic rings for Class II (B), and full delocalization between the aromatic rings occurs for Class III systems (C). ....	40
Figure 3.4.	Cyclic voltammograms of first redox events for CrNSal <sup>tBu</sup> , CrNSal <sup>H</sup> , CrNSal <sup>CF<sub>3</sub></sup> and CrNSal <sup>NO<sub>2</sub></sup> . Conditions: 0.1 M TBAP; CH <sub>2</sub> Cl <sub>2</sub> ; 1 mM complex; T = 298 K; scan rate = 100 mV/s.....	41
Figure 3.5.	Cyclic voltammograms of first redox events for CrNSal <sup>NEt<sub>2</sub></sup> , CrNSal <sup>NMe<sub>2</sub></sup> , CrNSal <sup>OiPr</sup> and CrNSal <sup>OMe</sup> . Conditions: 0.1 M TBAP; CH <sub>2</sub> Cl <sub>2</sub> ; 1 mM complex; T = 298 K; scan rate = 100 mV/s.....	42
Figure 3.6.	Stacked plots of cyclic voltammograms (black) and differential pulse voltammograms (red) for CrNSal <sup>OMe</sup> , CrNSal <sup>OiPr</sup> , CrNSal <sup>NMe<sub>2</sub></sup> and CrNSal <sup>NEt<sub>2</sub></sup> . Conditions: 1mM complex; 0.1 M TBAP; T = 293 K, CH <sub>2</sub> Cl <sub>2</sub> . ....	44
Figure 3.7.	Magic green oxidant titrations monitored by UV-vis-NIR spectroscopy for CrNSal <sup>NO<sub>2</sub></sup> , CrNSal <sup>CF<sub>3</sub></sup> , CrNSal <sup>H</sup> and CrNSal <sup>tBu</sup> . Black = neutral; grey = intermediate aliquots of oxidant; red = one equivalent of oxidant. Conditions: 0.45 mM complex; T = 233 K; CH <sub>2</sub> Cl <sub>2</sub> . ....	46
Figure 3.8.	Magic green oxidant titrations monitored by UV-vis-NIR spectroscopy for CrNSal <sup>OMe</sup> , CrNSal <sup>OiPr</sup> , CrNSal <sup>NMe<sub>2</sub></sup> and CrNSal <sup>NEt<sub>2</sub></sup> . Black = neutral; grey = intermediate aliquots of oxidant; red = one equivalent of oxidant. Conditions: 0.45 mM complex; T = 233 K; CH <sub>2</sub> Cl <sub>2</sub> . ....	47
Figure 3.9.	Frozen solution EPR spectra for concentration matched CrNSal <sup>R</sup> (black = experiment, red = oxidized). Conditions: T = 77 K; 0.45 mM complex; 0.1 M TBAP. See Table 3.4 for full instrumentation details. ....	49
Figure 3.10.	Frozen solution EPR spectra for concentration matched CrNSal <sup>R</sup> (black = experiment, red = oxidized). Conditions: T = 77 K; 0.45 mM complex; 0.1 M TBAP. See Table 3.4 for full instrumentation details. ....	50
Figure 3.11.	Solution IR spectra for neutral (black) and chemically oxidized with magic green (red) CrNSal <sup>OMe</sup> and CrNSal <sup>OiPr</sup> . Conditions: 5 mM complex; T = 293 K; CH <sub>2</sub> Cl <sub>2</sub> . ....	52

Figure 3.12.	Spin density plots for oxidized CrNSal <sup>NEt2</sup> in the BSS (A) and triplet (B) spin states. ....	55
Figure 4.1.	[Ru <sup>VI</sup> NSal <sup>H</sup> ] <sup>+</sup> is stable in the absence of an exogenous ligand (A). <sup>170</sup> Axial binding of an exogenous ligand activates the nitride towards homocoupling (B). ....	59
Figure 4.2.	Man's Ru <sup>VI</sup> nitride complex that performs C-H bond activation (A). <sup>68</sup> In the absence of exogenous ligands, the complex cannot activate strong C-H bonds such as those in cyclohexane (B) until exogenous ligands bind to vacant axial site (C). ....	60
Figure 4.3.	[CrNSal <sup>R</sup> ] <sup>+</sup> is relatively stable towards homocoupling at room temperature (A). Exogenous ligands should bind <i>trans</i> to the nitride and activate it towards homocoupling (B). ....	61
Figure 4.4.	[CrNSal <sup>R</sup> ] <sup>+</sup> may activate the weak C-H bonds in xanthene and form an N-insertion product (A). The addition of exogenous ligands should activate the nitride and increase reactivity(B). ....	61
Figure 4.5.	Titration of one equivalent of pyridine, bromide, and chloride into [CrNSal <sup>tBu</sup> ] <sup>+</sup> monitored by UV-vis-NIR spectroscopy. Conditions: 0.1 mM [CrNSal <sup>R</sup> ] <sup>+</sup> ; T = 253 K; CH <sub>2</sub> Cl <sub>2</sub> . Red = [CrNSal <sup>tBu</sup> ] <sup>+</sup> ; grey = intermediate aliquots of ligand; purple = one equivalent of ligand. ....	62
Figure 4.6.	UV-vis-NIR spectra for [CrNSal <sup>tBu</sup> ] <sup>+</sup> after 3 minutes of reaction with 1 equivalent of pyridine, bromide and chloride. Conditions: 0.1 mM [CrNSal <sup>tBu</sup> ] <sup>+</sup> ; T = 253 K; CH <sub>2</sub> Cl <sub>2</sub> . Red = [CrNSal <sup>tBu</sup> ] <sup>+</sup> ; purple = one equivalent of ligand. Decay of the 8,100 cm <sup>-1</sup> NIR band was also monitored over time for each ligand (bottom right). ....	63
Figure 4.7.	UV-vis-NIR spectra for [CrNSal <sup>NMe2</sup> ] <sup>+</sup> after 1 hour reaction with 1 equivalent of pyridine, bromide and chloride. Conditions: 0.1 mM [CrNSal <sup>NMe2</sup> ] <sup>+</sup> ; T = 253 K; CH <sub>2</sub> Cl <sub>2</sub> . Red = [CrNSal <sup>tBu</sup> ] <sup>+</sup> ; purple = one equivalent of ligand. ....	63
Figure 4.8.	ESI-MS spectrum of the reaction between [CrNSal <sup>tBu</sup> ] <sup>+</sup> and one equivalent of pyridine. Cr <sup>V</sup> NSal <sup>tBu</sup> starting material and various [Cr <sup>III</sup> Sal] <sup>+</sup> homocoupling decay products are observed. ....	64
Figure 4.9	GC-MS heaspace analysis of a Cr <sup>14</sup> Nsal <sup>tBu</sup> blank and oxidized Mn <sup>15</sup> Nsal <sup>tBu</sup> reference. Cr <sup>15</sup> Nsal <sup>tBu</sup> was oxidized with magic green and 100 equivalents of pyridine or 10 equivalents of tetraethylammonium chloride were added. ....	66
Figure 4.10.	Optimized structures for adducts between [CrNSal <sup>tBu</sup> ] <sup>+</sup> and pyridine, bromide and chloride. ....	67
Figure 4.11.	Reaction between oxidized CrNSal <sup>tBu</sup> and exogenous ligands to form adducts. ....	69
Figure 4.12.	UV-vis-NIR spectra for the reaction between [CrNSal <sup>R</sup> ] <sup>+</sup> and xanthene. Conditions: 0.1 mM [CrNSal <sup>R</sup> ] <sup>+</sup> ; 10 mM xanthene; T = 253 K; CH <sub>2</sub> Cl <sub>2</sub> . Red = [CrNSal <sup>R</sup> ] <sup>+</sup> ; grey = intermediate scans over time; purple = 2 hours after addition of xanthene. ....	70
Figure 4.13.	Positive-mode ESI-MS spectrum of reaction between [CrNSal <sup>CF3</sup> ] <sup>+</sup> and xanthene. ....	71
Figure 4.14.	Positive-mode ESI-MS spectrum of reaction between [CrNSal <sup>tBu</sup> ] <sup>+</sup> and xanthene. ....	71

Figure 4.15.	Positive-mode ESI-MS spectrum of reaction between $[\text{CrNSal}^{\text{NMe}_2}]^+$ and xanthene. No signal corresponding to the $\text{CrNSal}^{\text{NMe}_2}$ -xanthene N-insertion adduct is observed. ....	72
Figure 4.16.	C-H bond activation and N-insertion scheme for the reaction between $[\text{CrNSal}^{\text{R}}]^+$ ( $\text{R} = \text{CF}_3, \text{tBu}, \text{NMe}_2$ ). The nitride ligand first abstracts hydrogen from xanthene to form an alkyl radical and the imine complex $[\text{Cr}^{\text{V}}\text{N}=\text{HSal}^{\text{R}}]^+$ (A). Radical rebound occurs next and the $[\text{Cr}^{\text{IV}}\text{N}-\text{HXanSal}^{\text{R}}]^+$ adduct is formed (B). An additional HAT reaction can occur between $[\text{Cr}^{\text{IV}}\text{N}-\text{HXanSal}^{\text{R}}]^+$ and a second equivalent of $[\text{CrNSal}^{\text{R}}]^+$ to form the weakly coordinated adduct $[\text{Cr}^{\text{III}}\text{NH}=\text{XanSal}^{\text{R}}]^+$ (C). ....	73
Figure 5.1.	Proposed synthetic route to chromium salen nitride complexes bearing para imine groups. ....	77
Figure 5.2.	Proposed synthetic route to secondary amine groups at <i>para</i> positions of the aromatic rings. ....	79
Figure 5.3.	Potential increase of C-H bond activation reactivity upon axial binding of exogenous ligand. No reaction with stronger C-H bonds substrates such as cyclohexane occurs with oxidized $\text{CrNSal}^{\text{R}}$ in absence of exogenous ligand (A). The addition of exogenous ligand could increase the reactivity of the nitride ligand towards C-H bond activation or could accelerate the competing homocoupling pathway (B). ....	81
Figure 5.4.	UV-vis-NIR spectra for the reaction between $[\text{CrNSal}^{\text{R}}]^+$ and 9,10-dihydroanthracene. Conditions: 0.1 mM $[\text{CrNSal}^{\text{R}}]^+$ ; 10 mM 9,10-dihydroanthracene; $T = 253 \text{ K}$ ; $\text{CH}_2\text{Cl}_2$ . Red = $[\text{CrNSal}^{\text{R}}]^+$ ; grey = intermediate scans over time; purple = 2 hours after addition of 9,10-dihydroanthracene. ....	82
Figure 5.5.	The reaction of $[\text{CrNSal}^{\text{Bu}}]^+$ with the fluoride anion ligand. ....	82
Figure 5.6.	Future work regarding nitride activation and homocoupling. No reaction occurs in the absence of an exogenous ligand L (A). It is unknown if a reaction will occur if only one of the $[\text{CrNSal}^{\text{R}}]^+$ complexes contains an axial ligand (B), or if both complexes must be coordinated by axial ligands (C). ....	83

## List of Acronyms and Abbreviations

A	Hyperfine coupling constant (EPR)
Å	Ångström, $10^{-10}$ meters
atm	Atmospheres
<i>a, b, c</i>	Cell lengths (XRD)
$\alpha, \beta, \gamma$	Cell angles (XRD)
BDE	Bond dissociation energy
BSS	Broken-symmetry singlet
CF <sub>3</sub>	Trifluoromethyl group
CPE	Controlled potential electrolysis
CV	Cyclic voltammetry
cm <sup>-1</sup>	Wavenumbers
cm	Centimeters
$\Delta E$	Difference in energy
$\Delta E_{\text{ox}}$	Difference in potential
°C	Degrees Celsius
DCM	Dichloromethane
DFT	Density functional theory
DMSO	Dimethyl sulfoxide
DPV	Differential pulse voltammetry
deg	degrees
$\epsilon_r$	Dielectric constant
$\epsilon$	Molar extinction coefficient
$\delta$	Chemical shift
EPR	Electron paramagnetic resonance
$E_{1/2}$	Half-wave potential
$E_{\text{pa}}$	Anodic peak potential
$E_{\text{pc}}$	Cathodic peak potential
ESI-MS	Electrospray ionization-mass spectrometry
Et	Ethyl group



en	Ethylenediamine
F	Faraday's constant
F <sub>c</sub>	Ferrocene
F <sub>c</sub> <sup>+</sup>	Ferrocenium
F <sup>2</sup>	Squared structure-factor amplitude (XRD)
FeMoco	Iron-Molybdenum cofactor
GC-MS	Gas chromatography-mass spectrometry
GHz	Gigahertz
g	Grams
<i>g</i> <sub>⊥</sub>	<i>g</i> perpendicular (EPR)
<i>g</i> <sub>  </sub>	<i>g</i> parallel (EPR)
HAT	Hydrogen atom transfer
HIPT	Hexaisopropylterphenyl
HOMO	Highest occupied molecular orbital
Hz	Hertz
I	Reflection intensity (XRD)
IR	Infrared
<i>I</i> <sub>pa</sub>	Anodic peak current
<i>I</i> <sub>pc</sub>	Cathodic peak current
<i>J</i>	Coupling constant
K	Kelvin
<i>K</i> <sub>c</sub>	Comproportionation constant
kcal	Kilocalorie
kHz	Kilohertz
L	Ligand
λ	Incident beam wavelength (XRD)
λ <sub>max</sub>	Wavelength at maximum absorbance
LMCT	Ligand-to-metal charge transfer
LUMO	Lowest unoccupied molecular orbital
M	Molar
MHz	Megahertz

MO	Molecular Orbital
Me	Methyl group
MeCN	Acetonitrile
Melm	Methyl imidazole
MeOH	Methanol
Mes	Mesityl group
Mod. amp.	Modulation amplitude
Mod. freq.	Modulation frequency
mL	Millilitres
mM	Millimolar
mT	Milliteslas
mV	Millivolts
mW	Milliwatts
mm	Millimeters
m/z	Mass-to-charge ratio
$\mu$	Absorption coefficient (XRD)
$\mu\text{A}$	Microamperes
$\mu_{\text{eff}}$	Effective magnetic moment
$\nu$	Frequency
NBO	Non-bonding Orbital (MO)
NBO	Natural bond order (DFT)
NEt <sub>2</sub>	Diethylamino group
NIR	Near-infrared
NMe <sub>2</sub>	Dimethylamino group
NMR	Nuclear magnetic resonance
NO <sub>2</sub>	Nitro group
nm	nanometers
O <sup>i</sup> Pr	Isopropoxy group
OMe	Methoxy group
O <sup>t</sup> Bu	<i>Tert</i> -butoxy group
$\rho_{\text{calcd}}$	Calculated density (XRD)

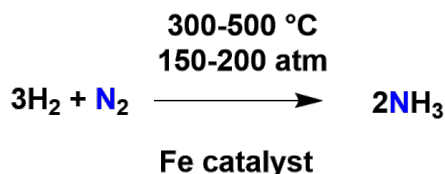
PCM	Polarized continuum model
Ph	Phenyl group
Py	Pyridine
ppm	Parts per million (NMR)
R	Ideal gas constant
$R$	Residual factor (XRD)
$\sigma$	Standard deviation
$\sigma_p$	<i>Para</i> Hammett Value
S	Electron spin quantum number
Sal	Salen Ligand
SOMO	Singly occupied molecular orbital
s	seconds
T	Temperature
TBAP	Tetrabutylammonium perchlorate
THF	Tetrahydrofuran
TM	Transition metal
TON	Turnover number
<sup>t</sup> Bu	<i>Tert</i> -butyl group
$\tau_5$	Index of degree of trigonality
UV-vis	Ultraviolet-visible
V	Volts
$V$	Cell volume (XRD)
$wR$	Weighted residual factor (XRD)
XAS	X-ray absorption spectroscopy
XRD	X-ray diffraction
Z	Formula units in unit cell (XRD)

# Chapter 1. Introduction

## 1.1. Overview of Transition Metal Nitrides

Transition metal nitrides garner significant interest for their properties in materials, photocatalysis, electrocatalysis, energy storage and plasmonics.<sup>1-8</sup> Nitride ligands display different bonding modes depending on the coordination environment and stoichiometric ratio of metal to nitrogen atoms, ranging from complex coordination compounds to discrete molecules.<sup>1,9,10</sup> This thesis will focus on the chemistry of terminal molecular nitrides ( $N^{3-}$ ) bound to a single metal center.

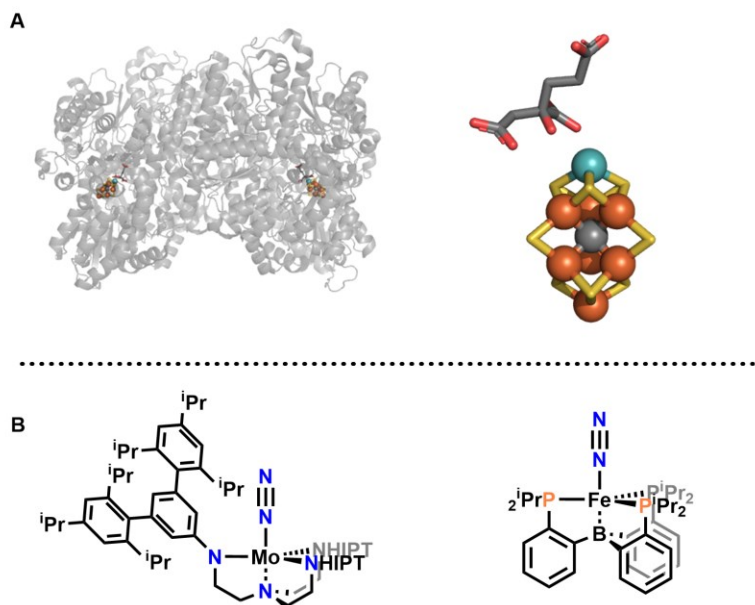
Nitrides are proposed intermediates along the nitrogen reduction pathway, which yields the essential feedstock chemical ammonia.<sup>11,12</sup> Ammonia is used in multiple industries including pharmaceuticals, fertilizers and metal treatment.<sup>13-15</sup> In particular, ammonia has received attention in the alternative energy sector as a green fuel with properties that make it more attractive than hydrogen gas.<sup>16</sup> While hydrogen gas is explosive and lacks infrastructure, ammonia carries a higher energy density, is not explosive, and society is already equipped to transport and store ammonia.<sup>17</sup> Currently, ammonia is produced using the Haber-Bosch process by flowing  $N_2$  and  $H_2$  at high temperatures and pressures over Fe or Ru catalysts according to Figure 1.1, which uses ~2% of the world's energy.<sup>18,19</sup> To meet the growing demand for ammonia, more efficient processes must be discovered.



**Figure 1.1. Haber Bosch process for ammonia production from  $H_2$  and  $N_2$  gas.<sup>19</sup>**

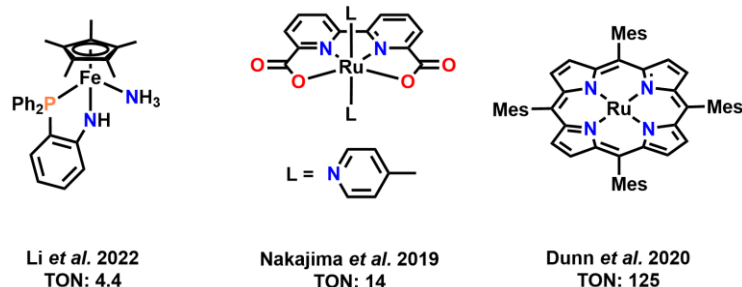
Chemists draw inspiration from natural systems such as the FeMoco active site in nitrogenase shown in Figure 1.2A, which has evolved to reduce nitrogen gas to ammonia under ambient conditions.<sup>20-24</sup> While the goal of reducing nitrogen under mild conditions with small molecules remains elusive, complexes incorporating Fe and Mo centers based on FeMoco have achieved catalytic nitrogen reduction using harsher temperatures and/or oxidants. The first molecular nitrogen reduction catalyst that functions at room temperature

was reported by Schrock & Yandulov and combines a Mo metal center with a tetradentate amide ligand (Figure 1.2B).<sup>25</sup> Peters *et al.* has also published multiple articles concerning nitrogen reduction with catalysts based on Fe and tris-phosphinoborane-type ligands.<sup>26–28</sup> Since then, many other transition metals and ligand scaffolds have proven to be capable of the nitrogen reduction reaction, although work continues to find robust catalysts that function under mild conditions.<sup>13,18,29,30</sup>



**Figure 1.2.** Nitrogenase enzyme and MoFe active site of dinitrogen fixation (orange = Fe; blue = Mo; grey = C) (A).<sup>21,22</sup> Transition metal complexes such as Schrock's Molybdenum catalyst (left) and Peter's Fe catalyst (right) can mimic this reactivity (B).<sup>25,26</sup>

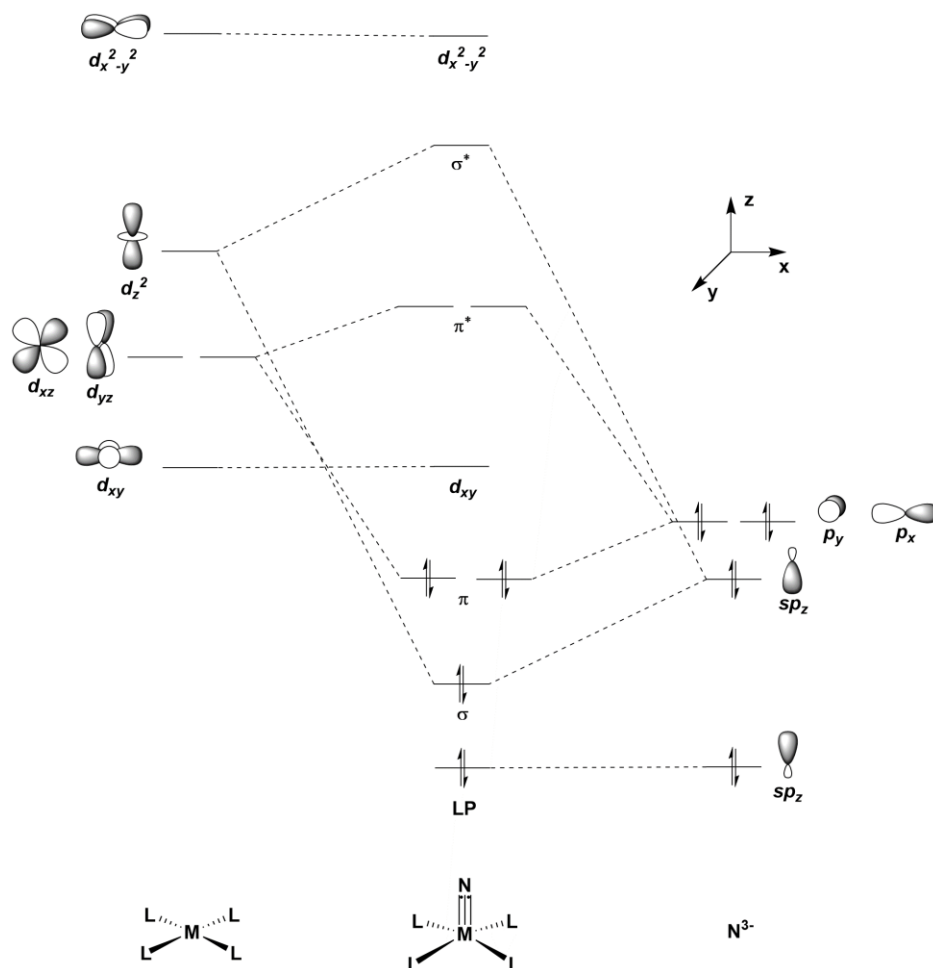
Complementary to the nitrogen reduction reaction, the ammonia oxidation reaction converts ammonia back into N<sub>2</sub> and H<sub>2</sub>. Compared to nitrogen reduction, research into molecular ammonia oxidation catalysts is less explored.<sup>31</sup> The ability to recycle ammonia back into its constituents will play an essential role in designing an ammonia fuel economy despite the initial challenge of ammonia synthesis. Again, nitride species are likely intermediates along the reaction pathway, with Fe, Mo and Ru complexes incorporating ligands such as porphyrins, phosphines and amides acting as catalysts.<sup>31–37</sup> Li *et al.*'s Fe amido, Nakajima *et al.*'s Ru diisoquinoline and Dunn *et al.*'s Ru porphyrin complexes for catalytic ammonia oxidation are depicted in Figure 1.3.<sup>33,35,36</sup>



**Figure 1.3. Fe and Ru molecular transition metal catalysts and their respective catalytic TON for the ammonia oxidation reaction.**<sup>33,35,36</sup>

## 1.2. Bonding in TM Nitride Complexes

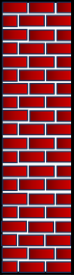



Bonding in transition metal nitride complexes is often compared to isoelectronic oxo ( $O^{2-}$ ) systems. Ballhausen and Gray devised the first bonding scheme for the vanadyl ion, using it to rationalize the electronic structure and reactivity of oxo complexes.<sup>38,39</sup> In principle, transition metal nitride complexes exhibit the same molecular orbital (MO) diagram as their oxo counterparts and an example MO diagram is shown below in Figure 1.4. The simplified MO diagram includes the metal  $d$  orbitals and nitride ligand orbitals in  $C_{4v}$  symmetry. Nitride ligand orbitals and  $d$  orbitals of appropriate energy and symmetry combine to form bonding and antibonding MO's. The  $d_{xy}$  and  $d_{x^2-y^2}$  orbitals of the metal as well as one of the  $sp_z$  hybrid orbitals are non-bonding. Importantly, the MO diagram predicts a non-bonding orbital (NBO) containing the lone pair of the nitride ligand, as well as a  $\sigma$ - and 2  $\pi$ -bonds comprising the  $M\equiv N$  triple bond.



**Figure 1.4. Simplified MO diagram for a  $d^0$  transition metal nitride complex with a nucleophilic nitride ligand.<sup>40</sup>**

The proposed bonding scheme provides insight into the reactivity and stability of early TM oxo and nitride complexes. The two  $\pi$  highest occupied molecular orbitals (HOMO's) are mostly nitride in character, consistent with the nucleophilic reactivity of the nitride ligand observed. The  $d_{xy}$  nonbonding orbital and two  $\pi^*$  antibonding orbitals comprise the lowest unoccupied molecular orbitals (LUMO's) and are largely metal in character, resulting in an electrophilic metal center. In terms of stability, metal complexes with one or two  $d$  electrons populate the  $d_{xy}$  NBO, with minimal effect on the bond order of the complex. However, as three or more  $d$  electrons are added from the metal center, the  $\pi$  antibonding orbitals are filled and the oxo or nitride ligand becomes unstable. Therefore, complexes with early transition metal centers in high oxidation states are favored, and oxo and nitride complexes become increasingly unstable moving right across a period.

Transition metal oxo and nitride complexes past Group 8 are transient or unknown despite past claims, resulting in the “oxo wall” coined by Gray and Winkler shown in Figure 1.5.<sup>39,41</sup>

3	4	5	6	7	8		9	10	11	12
Sc	Ti	V	Cr	Mn	Fe		Co	Ni	Cu	Zn
Y	Zr	Nb	Mo	Tc	Ru		Rh	Pd	Ag	Cd
Lu	Hf	Ta	W	Re	Os		Ir	Pt	Au	Hg

**Figure 1.5.** Gray and Winkler’s “oxo wall.” Early transition metal nitrides of Groups 3-8 are stable and isolable, whereas late transition metal nitrides are transient species.

## 1.3. Reactivity and Stability of Nitride Complexes

### 1.3.1. Early Transition Metal Nitrides

Early transition metal nitride complexes containing Groups 4-7 metal centers can be isolated, with the nitride ligand becoming increasingly unstable as *d* electrons are added as predicted by the bonding theory described in Section 1.2. However, Ti nitride complexes readily aggregate into multinuclear species, with Carroll *et al.* first isolating a mononuclear Ti nitride complex with a terminal nitride ligand in 2015 (Figure 1.6).<sup>42-44</sup> Similarly, Group V monomeric nitride complexes are also rare in literature, with only a few examples of V terminal nitride complexes known.<sup>45,46</sup> For the limited complexes known, the nitride ligand exhibits nucleophilic reactivity.

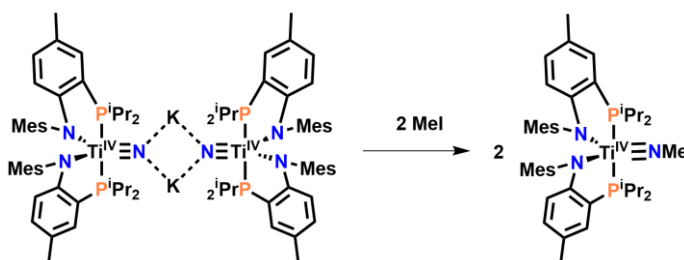


**Figure 1.6.** Potassium bridged Ti<sup>IV</sup> complex containing terminal nitride ligands.<sup>42-44</sup> The nitride ligand is nucleophilic and reacts with a variety of electrophiles such as methyl iodide.



Terminal nitride complexes of Groups 6, 7 and 8 can be readily formed employing a rich diversity of ligand scaffolds, making them more suitable as N-atom transfer reagents and catalysts in comparison to their Group 4 and 5 counterparts. Group 6 complexes of Cr, Mo and W contain nucleophilic nitride ligands that react with acid chlorides, boranes and other transition metals.<sup>47–50</sup> Some select reactions with a Cr<sup>V</sup> nitride acetylacetonate complex are shown below in Figure 1.7.<sup>50,51</sup>

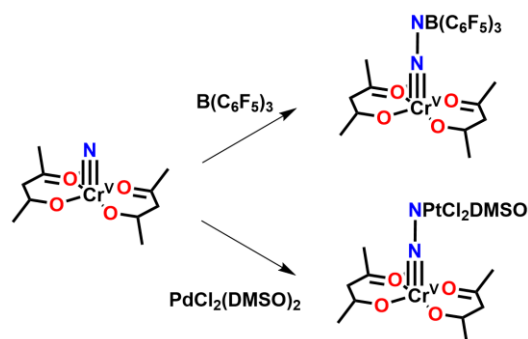


**Figure 1.7. Nucleophilic reactivity of Cr<sup>V</sup> nitride ligands towards boranes and late transition metals.**<sup>50,51</sup>

Group 7 complexes of Mn typically exhibit nucleophilic character at the nitride ligand and undergo N-atom transfer reactions to suitable substrates. Groves first unlocked the N-atom transfer reactivity of Mn nitrides by reaction of trifluoroacetic acid with a Mn<sup>V</sup> nitride complex ligated by a porphyrin ring.<sup>52</sup> The resulting nucleophilic imido complex can then transfer the imido ligand to cyclooctene to form an aziridine, analogous to epoxidation chemistry observed with transition metal oxo complexes. However, Shi *et al.* recently synthesized the Mn<sup>VI</sup> tetraamido complex shown in Figure 1.8 that reacts with electron-rich phosphines, highlighting that Mn nitrides can also act as electrophiles.<sup>53</sup> Shi *et al.* again showed the ambiphilic nature of Mn nitrides using this complex following changes in alkene aziridination reactivity.<sup>53</sup> Styrenes with strong electron withdrawing and strongly electron-donating groups reacted fastest compared to those with intermediate donation strengths, suggesting the nitride can behave as a nucleophile or electrophile. Tc nitride complexes have been synthesized, but their radioactivity limits their application as reagents or catalysts.<sup>54</sup> Multiple examples of nitrogen reduction reactions with Re nitride complexes have also been observed such as Meng *et al.*'s PNP complex shown in Figure 1.8.<sup>55–57</sup>

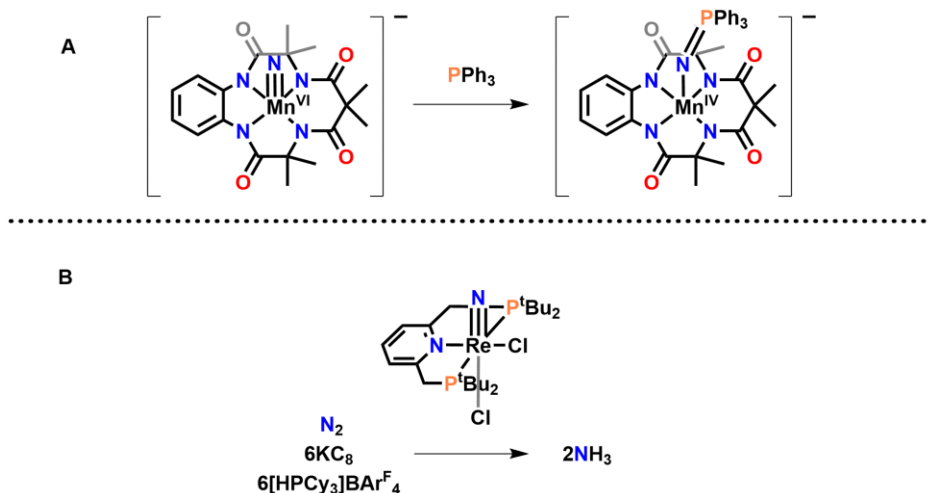


**Figure 1.8.** Shi *et al.*'s tetraamido cyclic Mn nitride complex that is reactive towards phosphine nucleophiles (A).<sup>53</sup> Meng *et al.*'s Re PNP pincer nitride complex that catalyzes ammonia oxidation (B).<sup>55</sup>

Finally, Group 8 transition metal nitride complexes can also participate in C-H bond activation, N-atom transfer and be protonated to form ammonia complexes modelling N<sub>2</sub> reduction.<sup>26–28,58–62</sup> Given that these complexes contain transition metals situated on the oxo wall, these complexes are challenging to isolate, with Peters *et al.* isolating the first room temperature stable Fe nitride complex in 2004 (Figure 1.9A).<sup>63</sup> Fe nitride ligands are electrophilic and react with olefins and alkynes to form valuable aziridine products.<sup>59,64</sup> Fe nitride complexes are prevalent in nitrogen reduction modelling where the nitride ligand is sequentially protonated, providing some inference as to the reactions occurring in the nitrogenase enzyme. Ambiphilic nitride ligands are also found in Os complexes, where an Os<sup>IV</sup> nitride complex could react with silyl halides or phosphines (Figure 1.9B).<sup>65</sup> Finally, Ru nitride complexes can participate in many reactions including C-H bond activation of alkanes and N-insertion with alkenes and alkynes.<sup>66–68</sup>

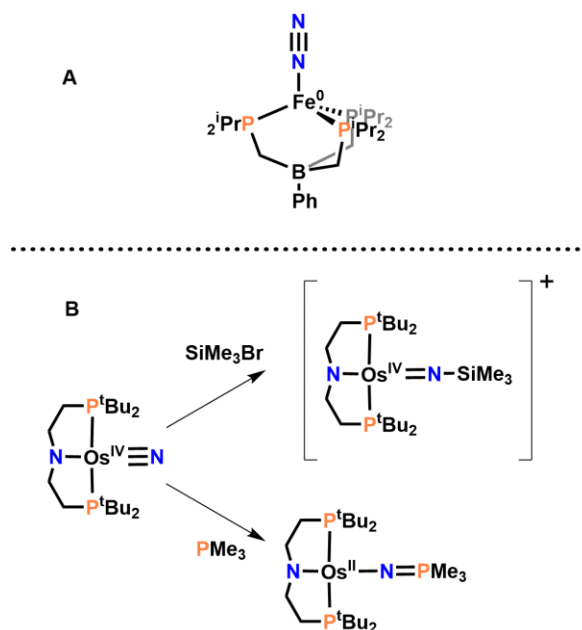


**Figure 1.9.** First stable terminal Fe nitride complex synthesized by Betley and Peters (A).<sup>63</sup> Ambiphilic reactivity of an Os nitride pincer complex. Electrophilic substrates such as silyl halides as well as nucleophilic phosphines react at the nitride (B).<sup>65</sup>

### 1.3.2. Late Transition Metal Nitrides

In accordance with the oxo wall, there are few examples of transition metal nitride complexes containing metals after Group 8 due to the addition of *d* electrons into anti-bonding molecular orbitals. These complexes are highly unstable and cannot be isolated, with spectroscopic detection also difficult. However, the decay products provide some evidence for transient nitride intermediates. For example, attempts to synthesize a Co nitride complex by photolysis of the azido ligand resulted in undesirable C-H bond activation and N-insertion into the pincer ligand as shown in Figure 1.10A with similar N-insertion/C-H bond activation occurring for a Co carbene complex.<sup>69,70</sup> This ligand insertion reactivity was also observed in a Ni PNP pincer complex upon photolysis of the azido complex (Figure 1.10B).<sup>71</sup> In addition to nitride insertion, nitride homocoupling can also occur leading to loss of the nitride ligands as N<sub>2</sub> gas as observed in Scheibel *et al.*'s Rh and Ir PNP pincer complexes (Figure 1.10C).<sup>72,73</sup>

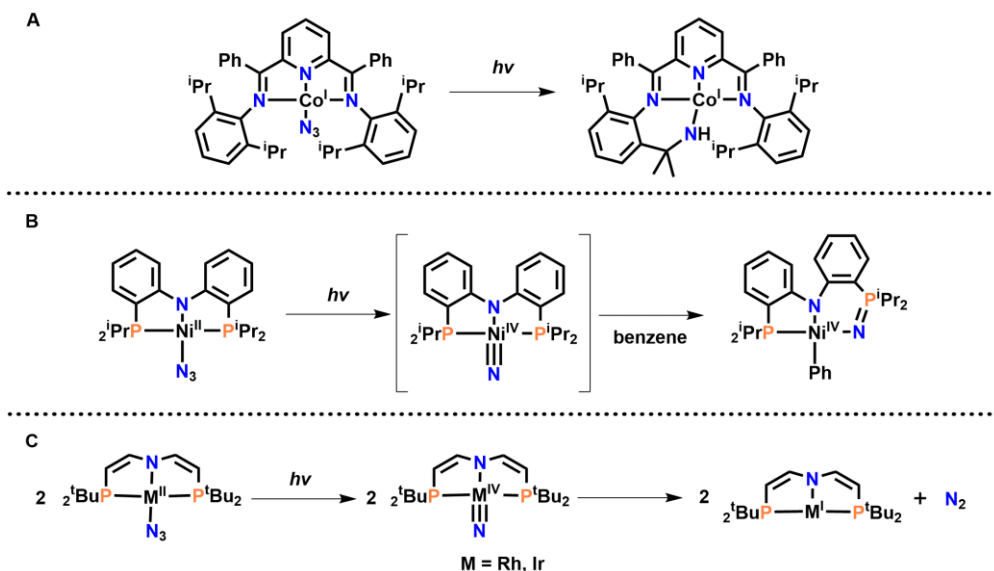


**Figure 1.10. Stability of late transition metal nitride complexes. Photolysis of Co(I) azido complexes yields ligand insertion products (A).<sup>69</sup> Ni pincer azido complexes form unstable nitride intermediates that perform ligand insertion after photolysis (B).<sup>70</sup> Rh(IV) and Ir(IV) complexes are unstable and homocouple to release N<sub>2</sub> gas (C).<sup>72,73</sup>**

## 1.4. Redox-Active Ligands and Salens

Redox-active or redox-non-innocent ligands were first conceptualized in 1966 by Jorgensen.<sup>74</sup> While redox-innocent ligands allow definitive assignment of the metal oxidation state, non-innocent ligands lead to an ambiguous metal oxidation state.<sup>75,76</sup> These redox-active ligands allow formation of complexes containing ligand radicals rather than high-valent metals after oxidation, displaying different properties and reactivity compared to their metal-oxidized analogues (Figure 1.11).<sup>77–80</sup> Similarly, redox-non-innocence also applies to reduction processes. Whether oxidation or reduction leads to ligand radical formation in a metal complex ultimately depends on the ordering of the ligand and metal HOMO and LUMO energies.

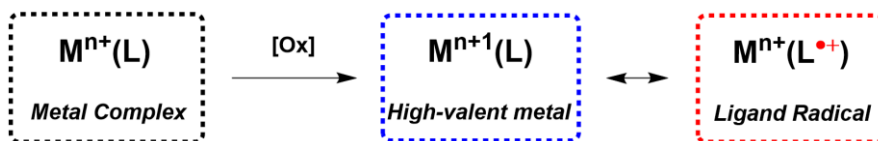


**Figure 1.11. Oxidation of transition metal complexes containing redox-active ligands can yield high-valent metals or ligand radicals.**

Nature utilizes redox-active ligands to facilitate challenging organic transformations, serving as inspiration for novel metal complexes that can mimic this remarkable reactivity. One example is cytochrome P450 which is responsible for the destruction of foreign molecules as well as the synthesis of signaling molecules such as hormones in humans and other organisms.<sup>81</sup> The active site of the enzyme contains a heme group, with an Fe metal center coordinated to a redox-active porphyrin ligand as shown in the PyMOL rendering in Figure 1.12A.<sup>22,82</sup> A cysteine amino acid coordinates axially and anchors the active site to the protein, leaving another axial site vacant for substrate binding. The catalytic cycle involves multiple peroxo and oxo intermediates, with Compound I being an Fe<sup>IV</sup> ligand radical species that performs oxygen insertion into C-H bonds (Figure 1.12B).<sup>81</sup>

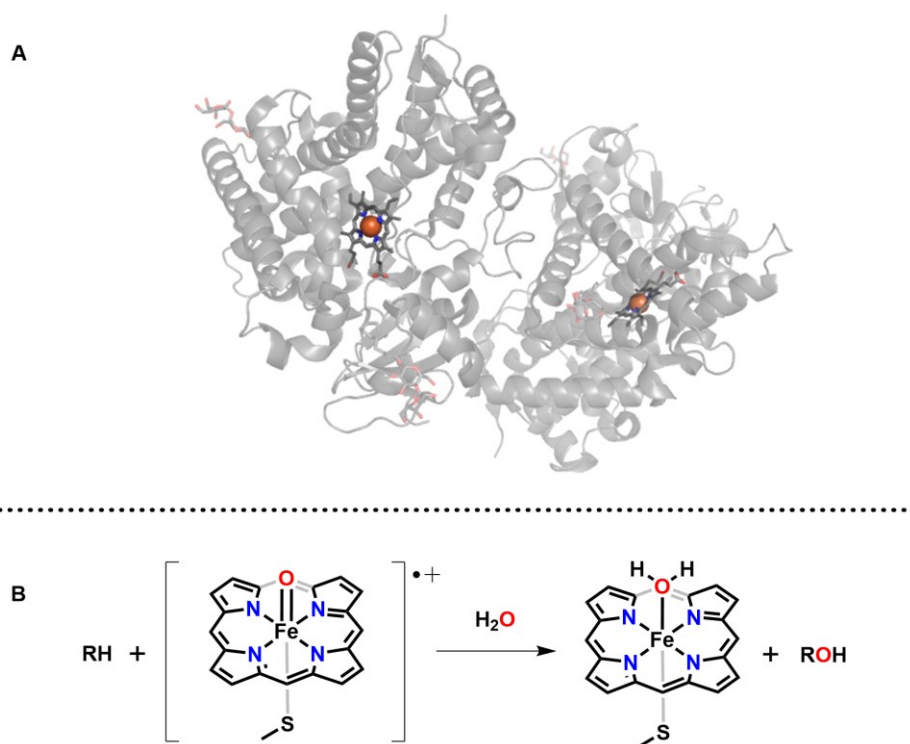


**Figure 1.12. Heme active sites in cytochrome P450 visualized using PyMOL (A).<sup>22,82</sup> The Fe<sup>IV</sup> radical cation performs the oxygen insertion step of the catalytic cycle (B).<sup>81</sup>**

Another example of an enzyme using a ligand radical to facilitate a challenging reaction is galactose oxidase found in certain fungus species.<sup>83,84</sup> This enzyme contains a Cu metal center and oxidizes primary alcohols to aldehydes in the presence of O<sub>2</sub>, releasing hydrogen peroxide.<sup>85,86</sup> The active site coordination sphere consists of two

histidines, two tyrosines and a water ligand that is displaced by the alcohol substrate during the catalytic cycle. A PyMOL rendering of the enzyme active sites and net reaction scheme are shown in Figure 1.13.<sup>22</sup> A ligand radical that is localized on the post-translationally-modified tyrosine amino acid ligand and is essential to the reactivity has been detected using electron paramagnetic resonance (EPR) and other spectroscopies.<sup>87,88</sup> Based on these observations, synthetic transition metal complexes often incorporate these redox-active phenolate groups and modify the electronic structure of the complex and achieve similar reactivity.<sup>89</sup>

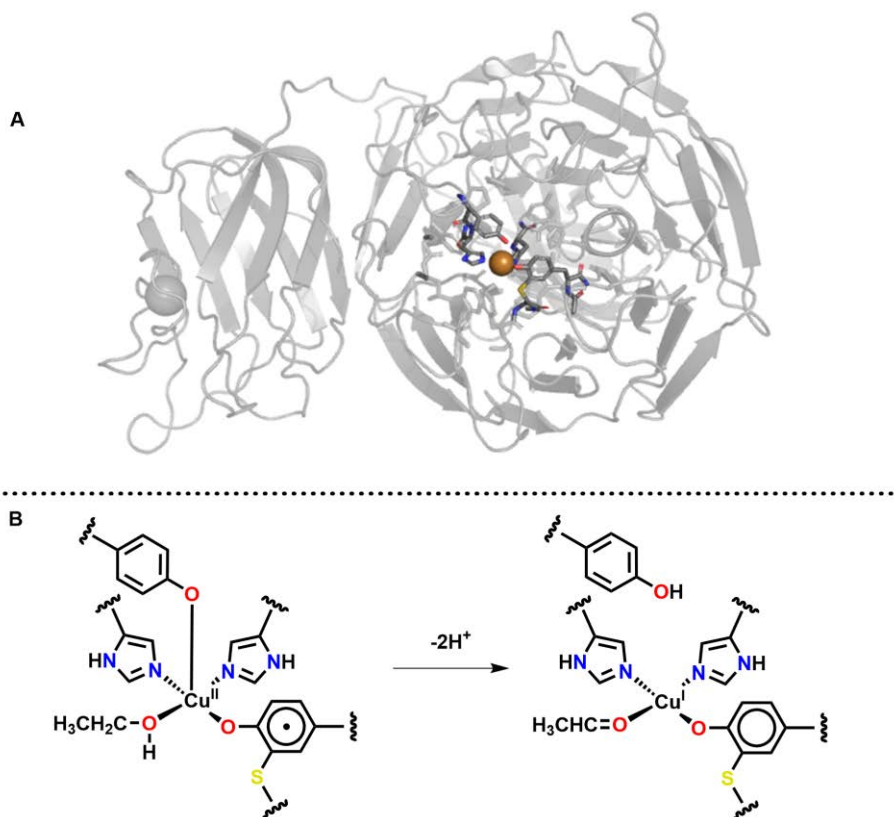


**Figure 1.13. Active site of galactose oxidase visualized using PyMOL (A).<sup>22,83</sup> Galactose oxidase catalyzes the oxidation of primary alcohols to aldehydes utilizing ligand radical intermediates (B).<sup>84,90</sup>**

The Storr group's main interest lies in the chemistry of transition metal complexes bearing salen ligands. Salen ligands are synthesized through the condensation reaction between 2 equivalents of salicylaldehyde (sal) and ethylenediamine (en), though this basic framework has been modified extensively (Figure 1.14A-C).<sup>91-93</sup> Different diamine backbones can be used, and the positions *ortho* and *para* to the phenol of the aromatic rings can easily be substituted with electron-donating or electron-withdrawing groups.

Moreover, salen ligands readily chelate a wide variety of transition metals and even lanthanides.<sup>94–96</sup> This versatility enables chemists to utilize a basic ligand framework and study changes in reactivity and electronic structure.

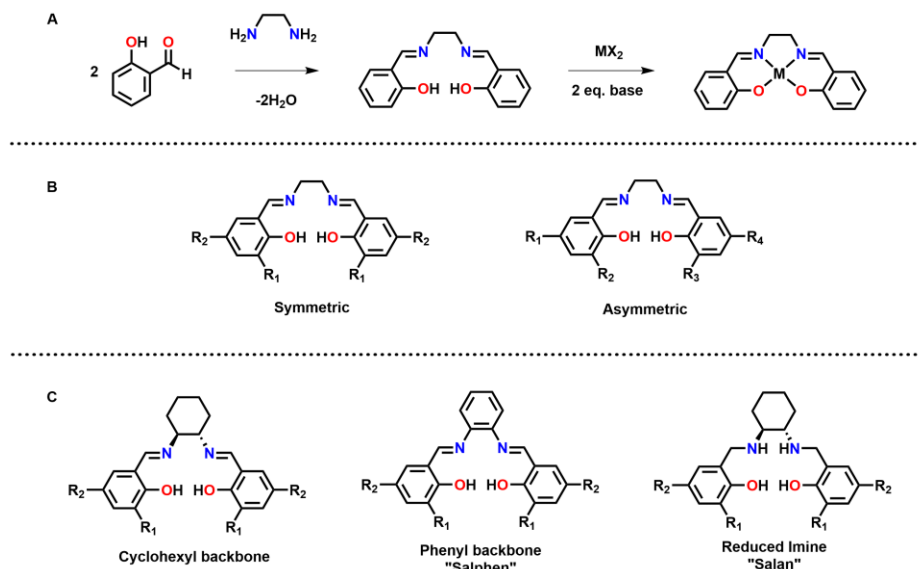


**Figure 1.14.** Select examples of salen ligands and their synthesis. Salen ligands are formed from the condensation reaction between a diamine and 2 equivalents of salicylaldehyde (A). The *para* and *ortho* groups can be substituted with one or more different R-groups to form symmetric or asymmetric ligands (B).<sup>91</sup> Different backbones can be used to enforce different electronics or geometries to the metal center (C).<sup>92</sup>

In addition to modularity, salen ligands are valuable for their redox-activity.<sup>97–99</sup> Ligand radical salen complexes can exhibit interesting electronic structures depending on identity of the metal center and chemical environment. For example, the metal used can determine whether the ligand radical is localized to one half of the salen ligand or delocalized over both phenolate rings as was observed in manganese and nickel systems respectively (Figure 1.15A).<sup>100,101</sup> Valence tautomerism in which external stimuli such as temperature or supporting electrolyte allow switching between metal and ligand oxidized states has also been observed in copper salen complexes (Figure 1.15B).<sup>102,103</sup> Finally, ligand coordination can also result in a change of the locus of oxidation. Oxidation of NiSal<sup>tBu</sup> yields the fully delocalized ligand radical species [NiSal<sup>tBu</sup>]<sup>•+</sup>, but the addition of pyridine yields a metal-oxidized adduct (Figure 1.15C).<sup>100</sup>

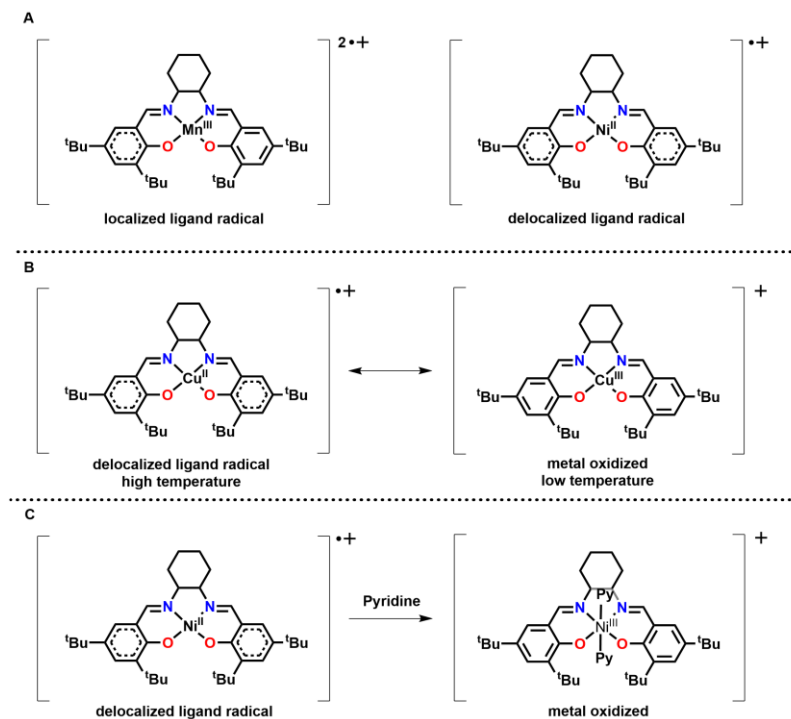


**Figure 1.15. Redox-active properties and electronic structures observed in transition metal salen complexes. Metal identity can influence the degree of ligand radical delocalization (A).<sup>100,101</sup> Cu salen complexes exhibit temperature-induced valence tautomerism between ligand radical and metal oxidized states (B).<sup>102</sup> Exogenous ligand coordination can trigger a change in locus of oxidation from ligand radical to metal oxidized in some Ni salen complexes (C).<sup>100</sup>**

In addition to the metal identity of the salen complex, the locus of oxidation can be influenced by additional factors such as the previously mentioned R-group substituents. For example, a Cu salen complex containing *para* <sup>t</sup>Bu substituents contains significant phenoxy radical character after oxidation at higher temperatures (Figure 1.16A), whereas the identical ligand bearing *para* CF<sub>3</sub> groups forms a high-valent metal after oxidation (Figure 1.16B).<sup>102,104</sup> As predicted, strong electron-donating groups such as NMe<sub>2</sub> facilitate the formation of ligand radicals, whereas electron withdrawing groups such as CF<sub>3</sub> favor the formation of metal oxidized species.<sup>97</sup> This donation strength of a given R-group can be determined empirically and is known as a Hammett parameter value ( $\sigma_p$  and  $\sigma_o$  for the *para* and *ortho* positions respectively).<sup>105</sup> The *ortho* positions often employ <sup>t</sup>Bu substituents to inhibit coupling of the aromatic rings should ligand radicals form.<sup>99</sup>



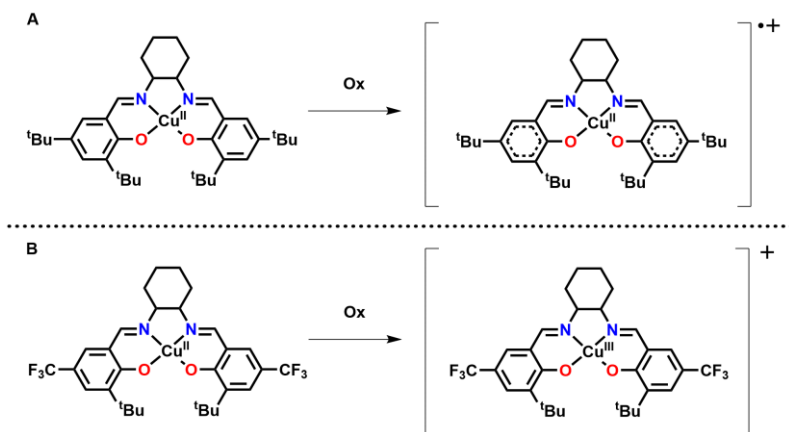


**Figure 1.16.** The locus of oxidation depends on the *para* substituent for transition metal salen complexes. Cu salen complexes undergo ligand-based oxidation for electron-donating groups (A) and metal oxidation for withdrawing groups (B).<sup>102,104</sup>

Manganese salen nitrides continue to be of interest within the Storr group. Previous work found that the <sup>t</sup>Bu, CF<sub>3</sub>, O<sup>t</sup>Bu, OMe and O<sup>i</sup>Pr R-groups *para* to the phenolate result in high-valent metal complexes upon oxidation, in contrast to the NMe<sub>2</sub> derivative which forms a ligand radical after oxidation as shown in Figure 1.17.<sup>106,107</sup> Interestingly, bis-oxidation of the OMe, O<sup>i</sup>Pr and NMe<sub>2</sub> derivatives results in bis-ligand radical species with the ligand radicals localized onto each half of the salen ligand.<sup>107</sup>

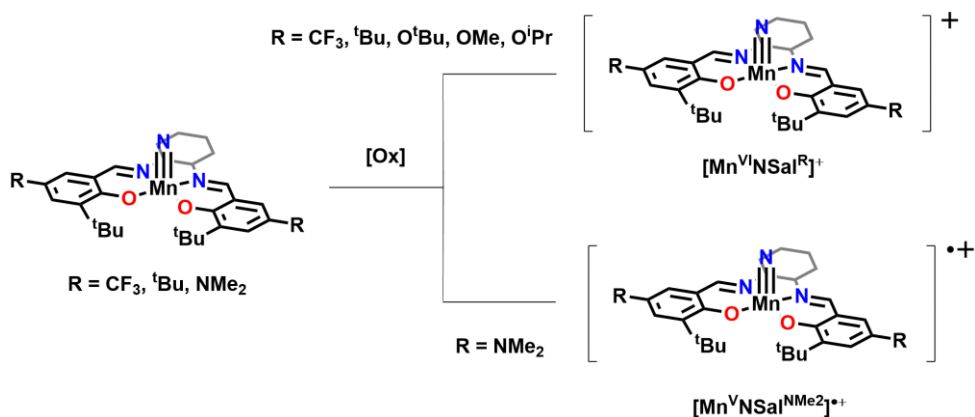


**Figure 1.17.** MnNSal<sup>R</sup> complexes previously synthesized in the Storr group. The electron-donating strength of the R-group influences the locus of oxidation.<sup>106,107</sup>

Moreover, the metal-oxidized species [Mn<sup>VI</sup>Sal<sup>tBu</sup>]<sup>+</sup> and [Mn<sup>VI</sup>Sal<sup>CF3</sup>]<sup>+</sup> rapidly decay at room temperature to release N<sub>2</sub> according to the scheme in Figure 1.18, while the ligand radical [Mn<sup>V</sup>Sal<sup>NMe2</sup>]<sup>•+</sup> is stable.<sup>108</sup> This homocoupling decay pathway results

from two of the oxidized  $[\text{Mn}^{\text{VI}}\text{Sal}^{\text{R}}]^+$  interacting with each other through their nitride ligands sufficiently to break the  $\text{Mn}\equiv\text{N}$  bond, forming  $\text{N}_2$  and two  $[\text{Mn}^{\text{III}}\text{Sal}^{\text{R}}]$ . This thermodynamically driven process has been observed in many other transition metal nitride systems. Based on the stability trends of the oxo wall, chromium salen nitrides should offer greater stability and facilitate electronic structure and reactivity studies.

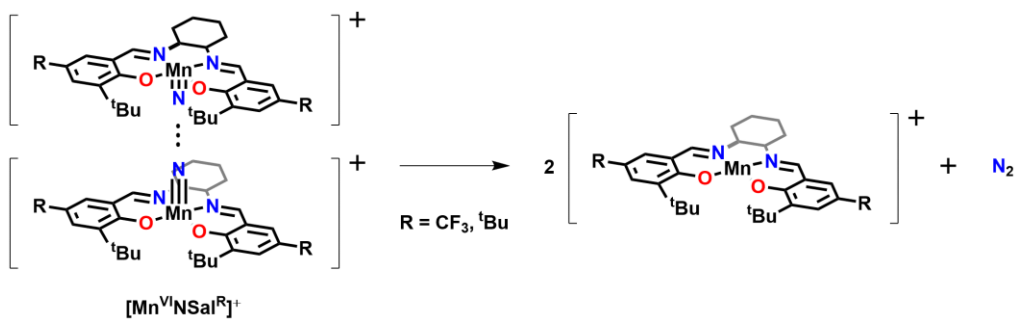


**Figure 1.18. Homocoupling decay for  $[\text{Mn}^{\text{VI}}\text{NSal}^{\text{R}}]^+$  ( $\text{R} = \text{tBu}, \text{CF}_3$ ) to yield  $\text{N}_2$  gas and  $[\text{Mn}^{\text{III}}\text{Sal}]^+$ .**<sup>106,107</sup>

## 1.5. Cr Salen Complexes

Research into Cr salen complexes first began in the 1970's, with the first synthesis and structural identification of  $\text{Cr}^{\text{III}}\text{ClSal}$  via x-ray crystallography achieved by Coggon *et al.* in 1970.<sup>109</sup> Since then,  $\text{Cr}^{\text{III}}$  salen complexes have become widespread in the literature, acting as catalysts for reactions such as hetero-Diels-Alder coupling, epoxide ring-opening, as well as the catalyst precursor to oxo transfer reagents.<sup>110–112</sup>  $\text{Cr}^{\text{V}}$  salen oxo complexes were first isolated and characterized by Siddall *et al.* in 1983, where they were shown to be strong electrophiles that perform oxygen insertion into alkenes to form epoxides catalytically or stoichiometrically as shown in Figure 1.19.<sup>113</sup> One of the most well-known epoxidation agents is Jacobsen's chromium oxo salen complex, which has the advantages of stability which permits study of the oxo complex versus the Mn analog.<sup>114–116</sup> Starting from  $\text{Cr}^{\text{III}}\text{ClSal}^{\text{tBu}}$ , an oxo transfer reagent shuttles the oxo ligand to the chromium salen complex to form  $[\text{Cr}^{\text{V}}\text{OSal}^{\text{tBu}}]^+$  *in situ*. This complex readily converts alkenes to epoxides, and the reactivity and enantioselectivity of these complexes can be tuned by exchanging groups *ortho* and *para* to the phenolate.<sup>117–119</sup> The relative instability of these  $[\text{Cr}^{\text{V}}\text{OSal}^{\text{R}}]^+$  complexes limits comprehensive study, but these serve as a useful comparison to nitride analogues based on their electronic structure and square-pyramidal geometry.

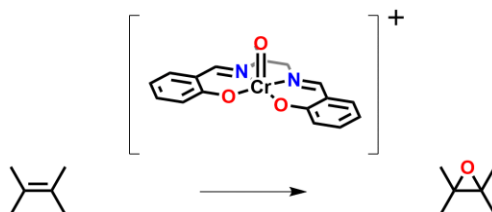


**Figure 1.19. Chromium analog of Jacobsen's catalyst for the epoxidation of alkenes.<sup>113</sup>**

The Storr group recently published work related to the synthesis and characterization of chromium salen nitride complexes bearing  $\text{CF}_3$ ,  $^t\text{Bu}$ , and  $\text{NMe}_2$  substituents at the *para* position of the phenolate. The locus of oxidation was identified using multiple spectroscopic and theoretical methods, ultimately finding that  $\text{CrNSal}^{^t\text{Bu}}$  and  $\text{CrNSal}^{\text{CF}_3}$  undergo metal-based oxidation whereas  $\text{CrNSal}^{\text{NMe}_2}$  forms a ligand radical upon oxidation according to Figure 1.20<sup>108</sup>

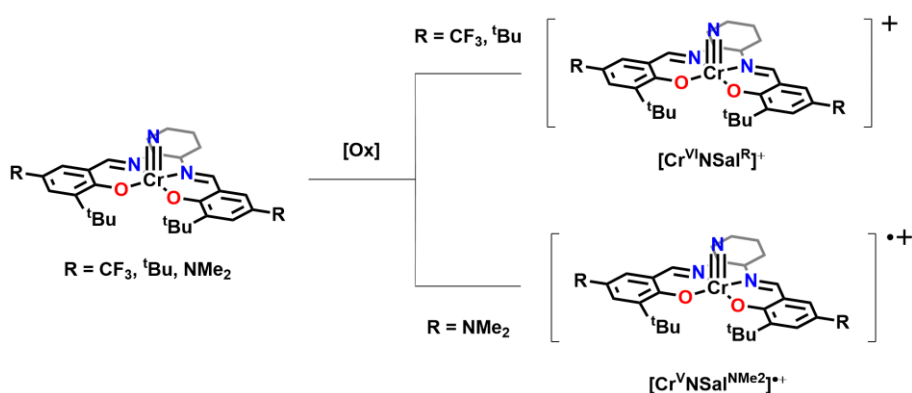


**Figure 1.20. Previously synthesized and characterized chromium salen nitride complexes.<sup>108</sup> The R-group substituent on the phenolate ring dictates the locus of oxidation.**

As discussed previously in Sections 1.2. and 1.3.1, neutral  $\text{Cr}^{\text{V}}$  nitrides are nucleophilic. Depending on the locus of oxidation, a change in reactivity was observed towards boranes and phosphines as shown in Figure 1.21. No reaction observed between boranes and electrophilic  $[\text{Cr}^{\text{VI}}\text{NSal}^{^t\text{Bu}}]^+$  and  $[\text{Cr}^{\text{VI}}\text{NSal}^{\text{CF}_3}]^+$ , while a reaction was observed with phosphines (Figure 1.21A). In contrast, the ligand radical  $[\text{Cr}^{\text{V}}\text{NSal}^{\text{NMe}_2}]^{+\bullet}$  retains sufficient nucleophilic nitride character to react with boranes, but does not react with phosphines (Figure 1.21B). This work provides the foundation for additional studies into electronic structure and reactivity.

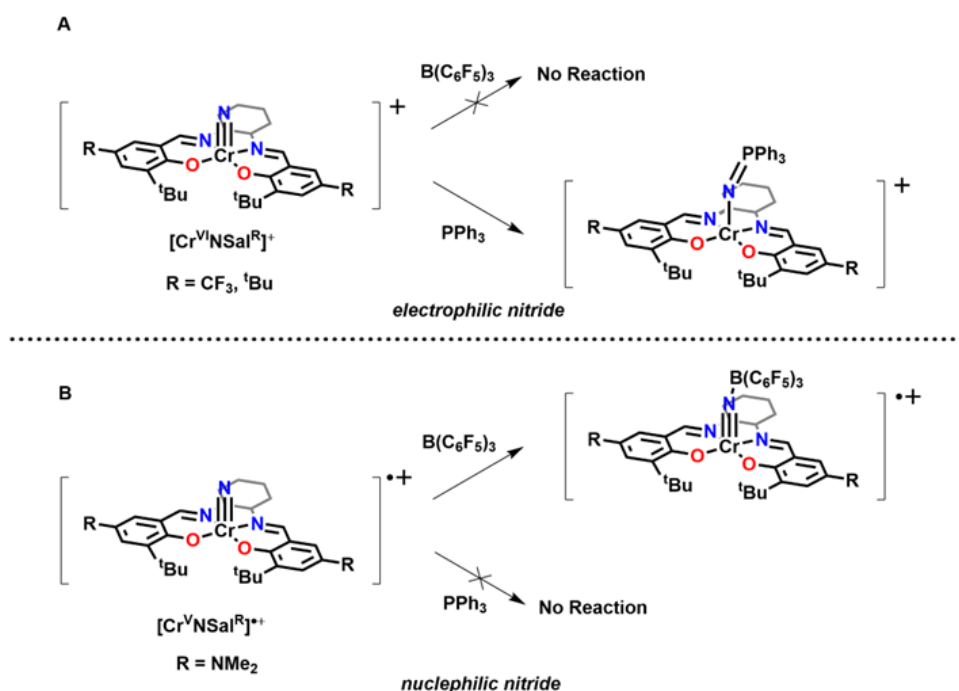


**Figure 1.21. Reactivity of  $[Cr^{VI}NSalR]^+$  (R = CF<sub>3</sub>, <sup>t</sup>Bu) (A) and  $[CrNSal^{NMe_2}]^{\bullet+}$  (B) towards Lewis acidic boranes and Lewis basic phosphines.<sup>108</sup> High valent metals are electrophilic and react with phosphines, whereas ligand radicals are nucleophilic and react with boranes.**

However, interest remains for oxidized chromium salen nitride complexes in various areas. One pertains to further fine-tuning of the locus of oxidation. The currently isolated complexes cover the  $\sigma_p$  values 0.54, -0.20 and -0.83 for the CF<sub>3</sub>, <sup>t</sup>Bu and NMe<sub>2</sub> derivatives respectively.<sup>108</sup> Based on current knowledge of the locus of oxidation, synthesizing new chromium salen nitride complexes with R-group  $\sigma_p$  values between -0.20 and -0.83 could unlock compounds with interesting electronic properties such as valence tautomerism. Secondly, the decay pathway of the oxidized complexes is poorly understood. Kinetics data indicates the oxidized complexes slowly decay according to second-order kinetics which is consistent with homocoupling, but further experiments need to be completed. Given the slow decay observed with oxidized chromium complexes, this presents the opportunity to investigate nitride activation by addition of ligands *trans* to the nitride. Finally, these oxidized chromium salen nitride complexes have unknown reactivity towards C-H bond activation. By synthesizing a larger suite of R-group derivatives as shown in Figure 1.22, a proper Hammett plot analysis can be conducted, as well as provide complexes better tuned for specific reactions. This thesis will explore

the synthesis and characterization of neutral chromium salen nitrides, followed by the electronic structure and reactivity of the complexes after oxidation.

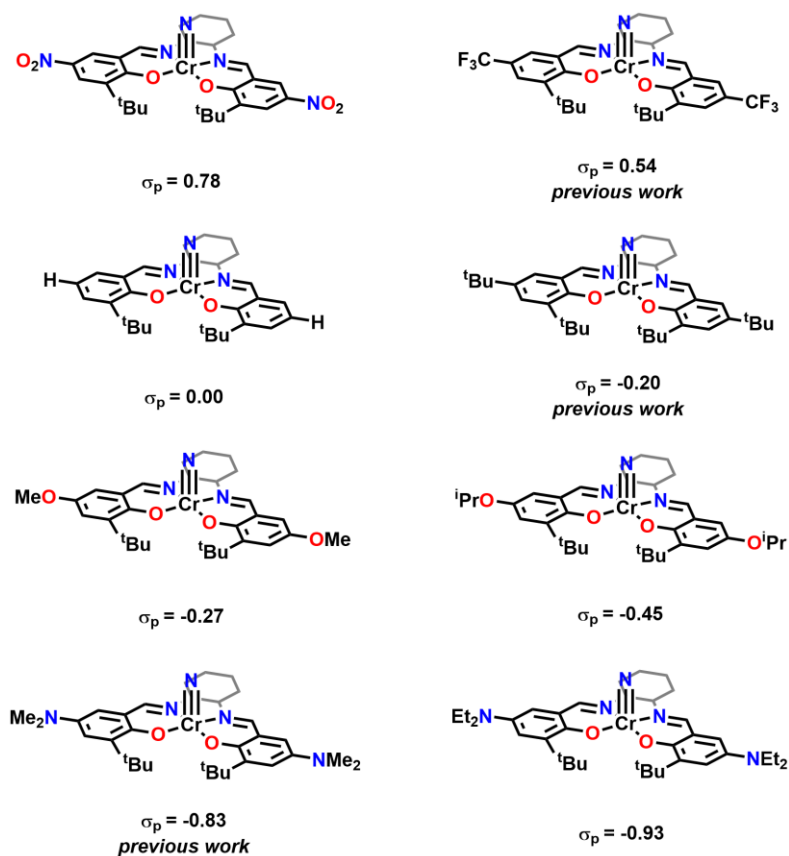


**Figure 1.22.** Target chromium salen nitrides with Hammett parameter values of the different *para* phenolate substituents.

## 1.6. Thesis Outline

Chapter 2 will focus on the synthesis and characterization of the new CrNSal<sup>R</sup> complexes using spectroscopic and computational methods. Chapter 3 focuses on determining the locus of oxidation for the new complexes using electrochemistry, EPR, UV-vis-NIR spectroscopy and computational analyses. Chapter 4 examines the reactivity of exogenous ligands and xanthene substrate with the oxidized chromium salen nitride complexes. Finally, Chapter 5 will detail future work including the synthesis of additional R-group derivatives and whether exogenous ligands could activate the nitride ligand towards C-H bond activation.

## Chapter 2. Synthesis and Characterization of Neutral CrNSal<sup>R</sup> Complexes (R = NO<sub>2</sub>, H, OMe, O<sup>i</sup>Pr, NEt<sub>2</sub>)

W. VandeVen synthesized CrNSal<sup>NO<sub>2</sub></sup>, CrNSal<sup>H</sup>, CrNSal<sup>OMe</sup>, CrNSal<sup>O<sup>i</sup>Pr</sup> and CrNSal<sup>NEt<sub>2</sub></sup>, collected UV-vis-NIR spectra, simulated EPR spectra and performed DFT studies. H<sub>2</sub>Sal<sup>NEt<sub>2</sub></sup> was synthesized according to an unpublished procedure by S. Mahato in the Storr Group. Preliminary data was reported for CrNSal<sup>O<sup>i</sup>Pr</sup> in a previous Storr group publication.<sup>108</sup> CrNSal<sup>tBu</sup>, CrNSal<sup>CF<sub>3</sub></sup>, and CrNSal<sup>NMe<sub>2</sub></sup> were synthesized according to the procedure reported by D. Martelino.<sup>108</sup> G. MacNeil collected EPR data using the Walsby group EPR spectrometer. W. Zhou and J. Pulfer collected and solved X-ray data.

### 2.1. Introduction

Transition metal nitride complexes can be synthesized through various methods depending on the target transition metal nitride.<sup>10,40</sup> Early synthetic routes involved complexation of metal salts with the ligand of interest, followed by treatment with a nitride precursor ligand (see Figure 2.1 for select examples). One method involves the photolysis of complexes containing the azido ligand, which generates the target nitride complex and is thermodynamically driven by the N<sub>2</sub> gas released.<sup>120,121</sup> Mn(III) salen complexes treated with ammonia as the nitrogen source and oxidant can also yield Mn(V) nitride complexes.<sup>122,123</sup> Many other methods based on the cleavage of N-heteroatom bonds such as nitrosyl, hydrazido or imines have also been used towards the isolation of other transition metal nitride complexes.<sup>124–126</sup> Furthermore, intermetal N-atom transfer based on the thermodynamic stability of the transition metal nitride product versus the transition metal nitride transfer reagent has become popular. For example, in accordance with oxo wall stability trends, nitride ligands are readily transferred from Mn nitride complexes to Cr as shown by Neely & Bottomley, and can be further tuned through careful ligand selection.<sup>127–130</sup>

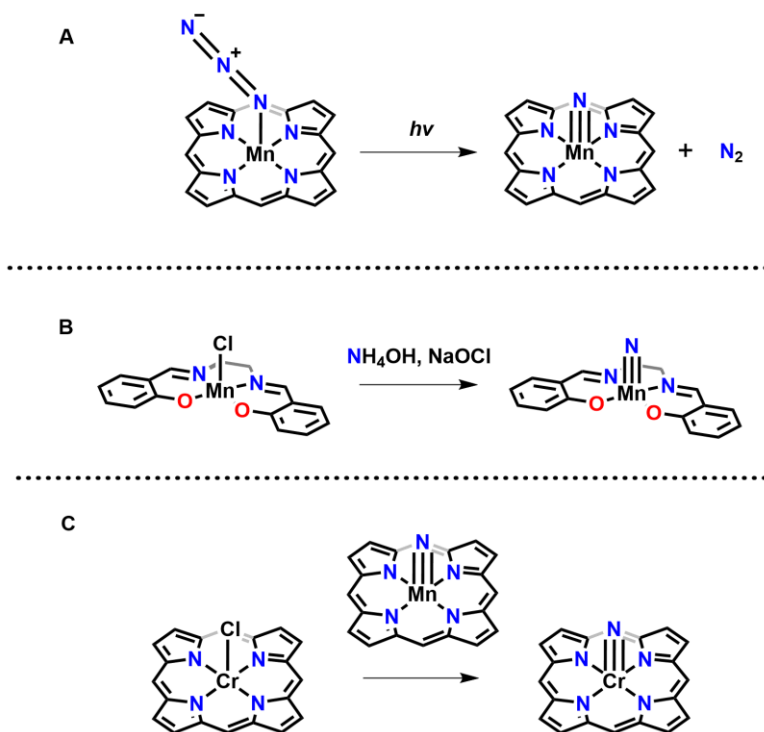


**Figure 2.1. Synthetic route to transition metal nitride complexes. Photolysis of azido ligands results in the metal nitride and release of  $N_2$  gas (A).<sup>120</sup> Reaction of  $MnClSal$  in ammonium hydroxide with bleach oxidizes ammonial ligands to nitrides (B).<sup>122,123</sup> Nitrides can be transferred from one metal complex to another (C).<sup>127,128,128,130</sup>**

The method previously used in the Storr group to isolate  $CrNSal^{CF_3}$ ,  $CrNSal^{tBu}$  and  $CrNSal^{NMe_2}$  was first discovered by Birk & Bendix and is based on intermetal N-atom transfer from  $MnNSal^H$  to  $Cr^{III}Cl_3 \cdot 3THF$ , generating a labile  $[CrN]^{2+}$  fragment in solution coordinated by weakly bound MeCN (Figure 2.2).<sup>127</sup> Simultaneously,  $Mn^{III}ClSal^H$  is formed as a byproduct and is easily removed due to its insolubility, facilitating purification. The  $[CrN]^{2+}$  fragment is readily chelated by salen ligands and will also metallate other ligand scaffolds as shown in Figure 2.2.

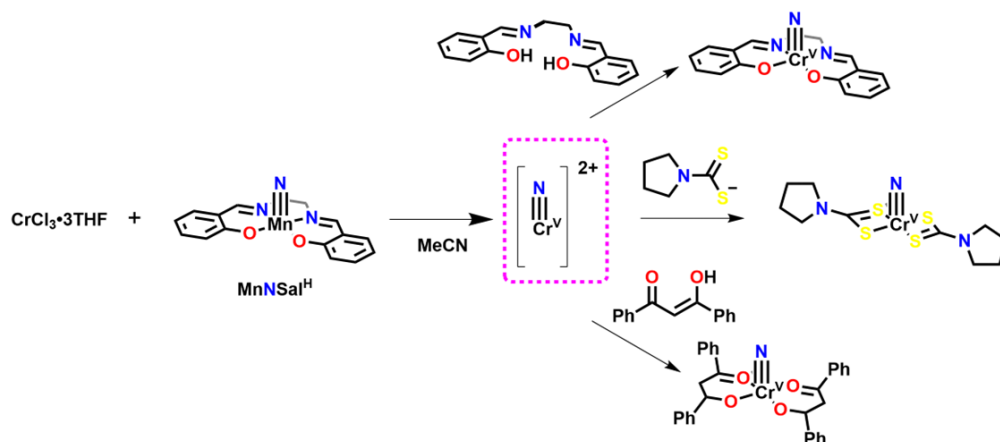


**Figure 2.2.** Intermetal N-atom transfer scheme developed by Birk & Bendix to generate a labile  $[\text{CrN}^{\text{V}}]^{2+}$  fragment (highlighted in purple).<sup>127</sup> Chelating ligands such as salens, pyrrolidinedithiocarbamate and acetylacetonate will displace weakly coordinated ligands to form Cr<sup>V</sup> nitride complexes.

## 2.2. Results

### 2.2.1. General Strategies for $\text{H}_2\text{Sal}^{\text{R}}$ Synthesis

As discussed in Chapter 1.4, salen ligands are synthesized through the condensation reaction between 2 equivalents of the substituted aldehyde of interest with 1 equivalent of diamine (Figure 2.3). All aldehydes and salen ligands were previously reported in the literature or according to methods developed in the Storr group.<sup>107,131–137</sup> ( $\pm$ )-*trans*-1,2-diaminocyclohexane was used as the diamine backbone in all syntheses. R-groups were chosen to expand the current range of  $\sigma_{\text{p}}$  Hammett values (Figure 2.3) and find novel electronic structures, as well as perform more rigorous analysis of how electron-donation strength influences reactivity.<sup>105</sup>



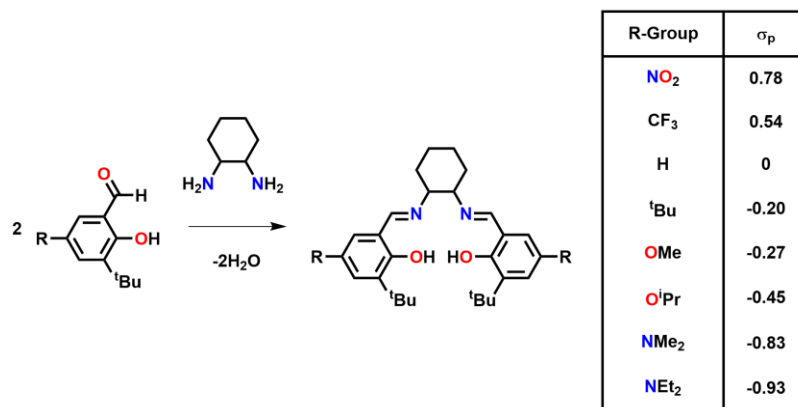


**Figure 2.3.** Synthetic route and  $\sigma_p$  values of R-group substituents for target salen ligands.

Hansch, Leo & Taft report the  $\sigma_p$  value of the NEt<sub>2</sub> substituent as -0.72 and NMe<sub>2</sub> substituent as -0.83.<sup>105</sup> This is unexpected, given that the ethyl groups should impart stronger electron-donation inductively. Another study by Price and Belanger determined the  $\sigma_p$  values of the NEt<sub>2</sub> and NMe<sub>2</sub> groups to be  $\sim$ -0.9 and  $\sim$ -0.8 respectively.<sup>138</sup> Herkstroeter also reported the NEt<sub>2</sub> and NMe<sub>2</sub>  $\sigma_p$  values as -0.72 and -0.63 respectively.<sup>139</sup> Electrochemical data in Section 3.2.1 also indicates that the NEt<sub>2</sub> substituent is more donating for this CrNSal system in comparison to NMe<sub>2</sub>. Therefore, in the absence of direct measurement of the  $\sigma_p$  value, we propose the  $\sigma_p$  value of -0.93 for the NEt<sub>2</sub> group based on the consensus value of -0.83 for the NMe<sub>2</sub> group, and the difference reported by Price and Belanger and Herkstroeter.

### 2.2.2. General Strategies for CrNSal<sup>R</sup> Synthesis

Two general methodologies were used in the synthesis of the CrNSal<sup>R</sup> derivatives discussed below. Both methods employ the use of MnNSal<sup>H</sup> as a nitride transfer reagent due to the thermodynamic favourability of transfer, as well as the low solubility of the MnSal<sup>H</sup>Cl by-product which facilitates purification. Either CrSal<sup>R</sup>Cl can be synthesized and reacted with MnSal<sup>H</sup>N according to Neely & Bottomley's procedure, or CrCl<sub>3</sub>•3THF can be reacted with MnSal<sup>H</sup>N to form a labile [CrN]<sup>2+</sup> species which is readily ligated with H<sub>2</sub>Sal<sup>R</sup> based on the method discussed previously by Bendix (Figure 2.4).<sup>127,128</sup> Where possible, complexes were purified via silica column chromatography. Due to the low solubility of the Cr<sup>III</sup>ClSal<sup>NO<sub>2</sub></sup> and Cr<sup>III</sup>ClSal<sup>H</sup> intermediates the Bendix method is the only way to access these target nitride products. Electrospray ionization mass spectrometry (ESI-MS) and

elemental analysis are consistent with the proposed mass and formula of the target complexes. Evan's method NMR indicated one unpaired electron for each complex as predicted for a  $\text{Cr}^{\text{V}} d^1$  system.

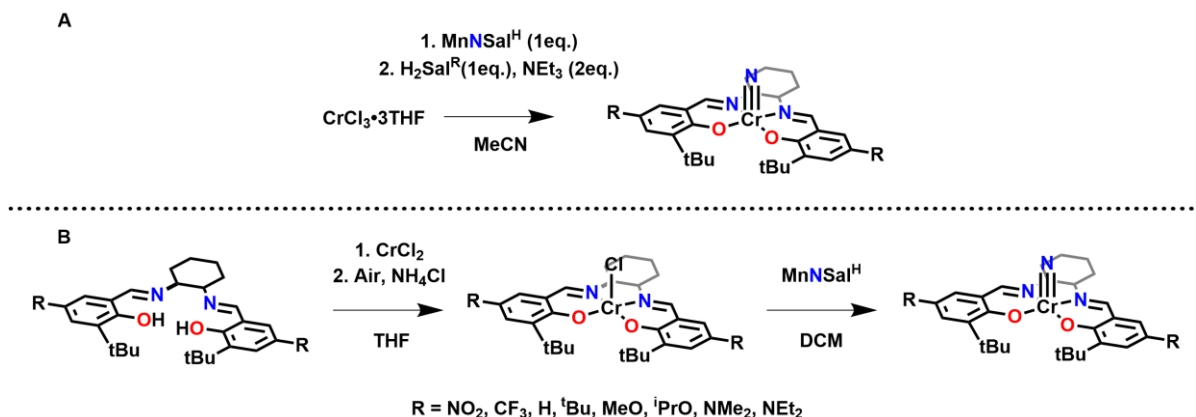


**Figure 2.4.** Synthetic routes to target  $\text{CrNSal}^{\text{R}}$  complexes. Either a  $[\text{CrN}]^{2+}$  fragment can be generated *in situ* and reacted with substituted salen ligand (A), or the  $\text{CrSal}^{\text{R}}\text{Cl}$  intermediate can be synthesized and reacted with the nitride transfer reagent (B).<sup>127,129</sup>

### 2.2.3. Solid-state Structures

Newly reported solid-state structures for  $\text{CrNSal}^{\text{NO}_2}$ ,  $\text{CrNSal}^{\text{CF}_3}$ ,  $\text{CrNSal}^{\text{H}}$ ,  $\text{CrNSal}^{\text{OMe}}$  and  $\text{CrNSal}^{\text{O}^{\text{iPr}}}$  are shown below in Figures 2.5 to 2.9 ( $\text{CrNSal}^{\text{tBu}}$  and  $\text{CrNSal}^{\text{NMe}_2}$  previously reported).<sup>108</sup> Crystals suitable for XRD were obtained using various solvent combinations and slow evaporation.  $\text{CrNSal}^{\text{O}^{\text{iPr}}}$  was crystallized by layering hexane on THF and slow evaporation. Single crystals of  $\text{CrNSal}^{\text{OMe}}$  were grown by dissolving in hot MeCN and slow evaporation.  $\text{CrNSal}^{\text{CF}_3}$  crystals were obtained by layering hexane on DCM and slow evaporation. Crystals of  $\text{CrNSal}^{\text{NO}_2}$  and  $\text{CrNSal}^{\text{H}}$  were grown by layering MeCN on DCM and slow evaporation. Attempts to crystallize  $\text{CrNSal}^{\text{NEt}_2}$  were unsuccessful and led to amorphous powders regardless of solvent systems tested. Comparison to previously reported chromium nitride complexes reveals similar coordination sphere bond lengths, and computational methods agree closely. Key crystallographic information is recorded in Table 2.1 below. Of note is the short  $\text{Cr}\equiv\text{N}$  bond length of  $\sim 1.5\text{\AA}$ , similar to other  $\text{Cr}\equiv\text{N}$  complexes (see Table 2.4 for coordination sphere bond lengths).<sup>121,140</sup> Moreover, the  $\text{Cr}\equiv\text{N}$  bond length decreases as the  $\sigma_p$  increases, in accordance with a more electron-deficient metal center. In all complexes, the Cr atom is

slightly out of the plane of the salen ligand towards the nitride, which is also consistent with the literature.<sup>108,121,140</sup>

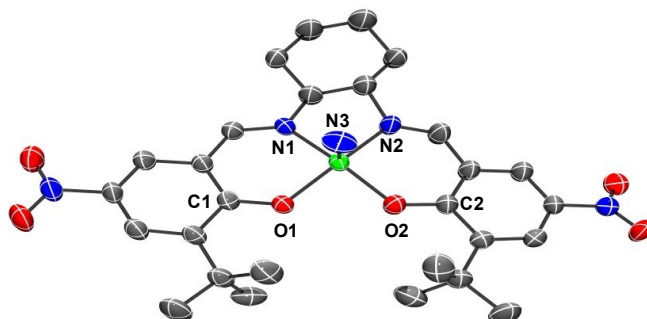


**Figure 2.5.** XRD structure of CrNSal<sup>NO<sub>2</sub></sup> visualized using POV-Ray. Thermal ellipsoids shown at 50% probability level. Hydrogen atoms omitted for clarity. Cr, pink; C grey; O, red; N, blue. Select interatomic distances [Å] and angles [deg]: Cr(1)-O1: 1.910(2), Cr(1)-O(2): 1.906(2), Cr(1)-N(1): 2.015(3), Cr(1)-N(2): 2.002(3), Cr(1)-N(3): 1.560(4), O(1)-C(1): 1.314(4), O(2)-C(2): 1.314(4). Angles: O(1)-Cr(1)-O(2): 89.1(5), O(1)-Cr(1)-N(1): 88.0(6), O(1)-Cr(1)-N(2): 152.4(4), O(1)-Cr(1)-N(3): 104.8(7), O(2)-Cr(1)-N(2): 89.2(7), O(2)-Cr(1)-N(1): 149.3(9), O(2)-Cr(1)-N(3): 107.6(8), N(1)-Cr(1)-N(2): 79.5(0), N(1)-Cr(1)-N(3): 102.4(7), N(2)-Cr(1)-N(3): 101.8(0).

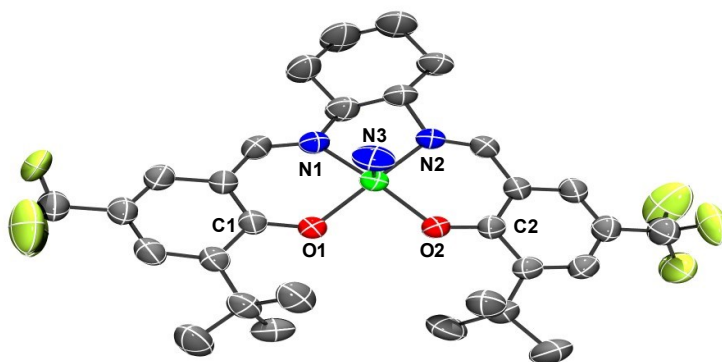


**Figure 2.6.** XRD structure of  $\text{CrNSal}^{\text{CF}_3}$  visualized using POV-Ray. Thermal ellipsoids shown at 50% probability level. Hydrogen atoms omitted for clarity. Cr, pink; C grey; O, red; N, blue. Select interatomic distances [Å] and angles [deg]: Cr(1)-O(1): 1.909(2), Cr(1)-O(2): 1.910(2), Cr(1)-N(1): 2.021(3), Cr(1)-N(2): 2.010(3), Cr(1)-N(3): 1.539(3), O(1)-C(1): 1.309(4), O(2)-C(2): 1.307(5). Angles: O(1)-Cr(1)-O(2): 89.3(6), O(1)-Cr(1)-N(1): 87.6(2), O(1)-Cr(1)-N(2): 153.3(9), O(1)-Cr(1)-N(3): 104.5(8), O(2)-Cr(1)-N(2): 88.4(6), O(2)-Cr(1)-N(1): 146.1(7), O(2)-Cr(1)-N(3): 110.0(3), N(1)-Cr(1)-N(2): 79.6(4), N(1)-Cr(1)-N(3): 103.2(8), N(2)-Cr(1)-N(3): 101.0(5).

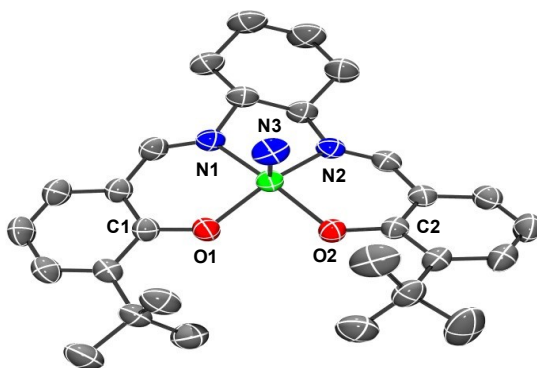


**Figure 2.7.** XRD structure of  $\text{CrNSal}^{\text{H}}$  visualized using POV-Ray. Thermal ellipsoids shown at 50% probability level. Hydrogen atoms omitted for clarity. Cr, pink; C grey; O, red; N, blue; F, green. Select interatomic distances [Å] and angles [deg]: Cr(1)-O(1): 1.896(1), Cr(1)-O(2): 1.915(1), Cr(1)-N(1): 2.008(1), Cr(1)-N(2): 2.031(1), Cr(1)-N(3): 1.549(2), O(1)-C(1): 1.317(2), O(2)-C(2): 1.316(2). Angles: O(1)-Cr(1)-O(2): 87.8(1), O(1)-Cr(1)-N(1): 88.3(5), O(1)-Cr(1)-N(2): 141.5(8), O(1)-Cr(1)-N(3): 111.9(3), O(2)-Cr(1)-N(2): 88.7(7), O(2)-Cr(1)-N(1): 156.4(7), O(2)-Cr(1)-N(3): 104.5(7), N(1)-Cr(1)-N(2): 79.9(7), N(1)-Cr(1)-N(3): 98.3(8), N(2)-Cr(1)-N(3): 105.9(7).

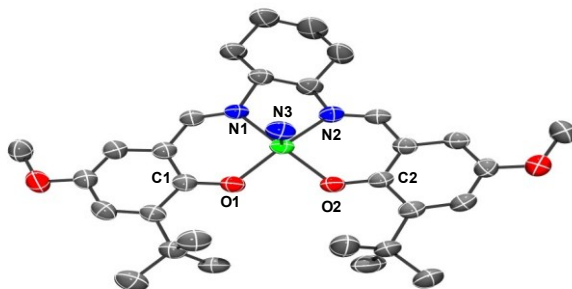


**Figure 2.8.** XRD structure of CrNSal<sup>OMe</sup> visualized using POV-Ray. Thermal ellipsoids shown at 50% probability level. Hydrogen atoms omitted for clarity. Cr, pink; C grey; O, red; N, blue. Select interatomic distances [Å] and angles [deg]: Cr(1)-O(1): 1.907(3), Cr(1)-O(2): 1.911(3), Cr(1)-N(1): 2.010(3), Cr(1)-N(2): 2.006(5), Cr(1)-N(3): 1.556(5), O(1)-C(1): 1.317(5), O(2)-C(2): 1.318(6). Angles: O(1)-Cr(1)-O(2): 89.5(1), O(1)-Cr(1)-N(1): 88.6(3), O(1)-Cr(1)-N(2): 147.0(8), O(1)-Cr(1)-N(3): 108.9(8), O(2)-Cr(1)-N(2): 86.7(6), O(2)-Cr(1)-N(1): 152.7(4), O(2)-Cr(1)-N(3): 105.0(4), N(1)-Cr(1)-N(2): 80.2(2), N(1)-Cr(1)-N(3): 101.2(1), N(2)-Cr(1)-N(3): 103.5(5).

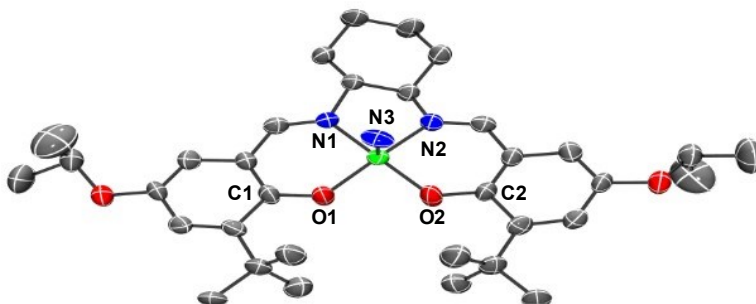


**Figure 2.9.** XRD structure of CrNSal<sup>OiPr</sup> visualized using POV-Ray. Thermal ellipsoids shown at 50% probability level. Hydrogen atoms omitted for clarity. Cr, pink; C grey; O, red; N, blue; F, green. Select interatomic distances [Å] and angles [deg]: Cr(1)-O(1): 1.839(6), Cr(1)-O(2): 1.823(6), Cr(1)-N(1): 2.036(6), Cr(1)-N(2): 2.051(6), Cr(1)-N(3): 1.538(1), O(1)-C(1): 1.340(9), O(2)-C(2): 1.340(9). Angles: O(1)-Cr(1)-O(2): 92.0(2), O(1)-Cr(1)-N(1): 89.9(6), O(1)-Cr(1)-N(2): 153.5(5), O(1)-Cr(1)-N(3): 101.3(8), O(2)-Cr(1)-N(2): 89.9(8), O(2)-Cr(1)-N(1): 157.8(6), O(2)-Cr(1)-N(3): 98.5(0), N(1)-Cr(1)-N(2): 78.7(5), N(1)-Cr(1)-N(3): 102.7(1), N(2)-Cr(1)-N(3): 104.3(9).

**Table 2.1. Key crystallographic information for CrNSal<sup>NO2</sup>, CrNSal<sup>CF3</sup>, CrNSal<sup>H</sup>, CrNSal<sup>OMe</sup> and CrNSal<sup>OiPr</sup>.**

Complex	CrNSal <sup>NO2</sup>	CrNSal <sup>CF3</sup>	CrNSal <sup>H</sup>	CrNSal <sup>OMe</sup>	CrNSal <sup>OiPr</sup>
<b>Formula</b>	C <sub>28</sub> H <sub>34</sub> CrN <sub>5</sub> O <sub>6</sub>	C <sub>30</sub> H <sub>34</sub> CrF <sub>6</sub> N <sub>3</sub> O <sub>2</sub>	C <sub>28</sub> H <sub>36</sub> CrN <sub>3</sub> O <sub>2</sub>	C <sub>30</sub> H <sub>40</sub> CrN <sub>3</sub> O <sub>4</sub>	C <sub>34</sub> H <sub>48</sub> CrN <sub>3</sub> O <sub>4</sub>
<b>Formula weight</b>	588.61	634.61	498.61	558.66	614.77
<b>Space group</b>	P 1 21/c 1	P b c a	P 1 21/n 1	P 1	I 2
<b>a (Å)</b>	11.34(5)	23.55(3)	13.14(3)	11.19(1)	14.90(7)
<b>b (Å)</b>	23.91(4)	10.85(2)	12.80(5)	11.40(5)	13.44(0)
<b>c (Å)</b>	10.82(5)	23.89(4)	15.45(5)	13.41(1)	21.26(4)
<b>α (deg)</b>	90	90	90	87.71(6)	90
<b>β (deg)</b>	104.66(1)	90	99.91(5)	69.85(6)	99.15(5)
<b>γ (deg)</b>	90	90	90	82.00(9)	90
<b>V (Å<sup>3</sup>)</b>	2841.17	6107.5(4)	2562.20	1591.3(2)	4206.0(4)
<b>Z</b>	4	8	33	2	2
<b>T (K)</b>	296	296	296	296	210
<b>ρ<sub>calcd</sub> (g cm<sup>-3</sup>)</b>	1.376	1.380	1.293	1.252	1.142
<b>λ (Å)</b>	1.54178	0.71073	1.54178	1.54178	0.71073
<b>μ (mm<sup>-1</sup>)</b>	3.735	0.443	3.898	3.282	0.315
<b>R indices with I &gt; 2.0σ(I) (data)</b>	0.0604	0.0551	0.0318	0.0491	0.0831
<b>wR<sub>2</sub></b>	0.1472	0.1467	0.0924	0.1449	0.2707
<b>R<sub>1</sub></b>	0.0604	0.0551	0.0318	0.0491	0.0831
<b>Goodness-of-fit on F<sup>2</sup></b>	1.053	1.011	1.046	1.094	1.100

## 2.2.4. Electron Paramagnetic Resonance

Chromium(V) salen nitride complexes contain one unpaired electron in a  $3d$  orbital. Low temperature electron paramagnetic resonance (EPR) can detect this electron and provide information on complex geometry. The addition of supporting electrolyte reduces intermolecular interactions and simplifies analysis of spectra. Spectra for novel compounds are shown below in Figures 2.10 and 2.11, and full instrumental details are collected in Table 2.2. Simulations were performed in MATLAB using the EasySpin package.<sup>141,142</sup> The EPR data for CrNSal<sup>R</sup> (R = CF<sub>3</sub>, <sup>t</sup>Bu, NMe<sub>2</sub>) were reported previously.<sup>108</sup> All neutral complexes have  $g$  values at ca. 1.99, close to the theoretical value of 2.0023 for a free electron and consistent with a  $3d^1$  metal centre.<sup>143</sup> The axial symmetry line shape also supports a square-based pyramidal geometry.

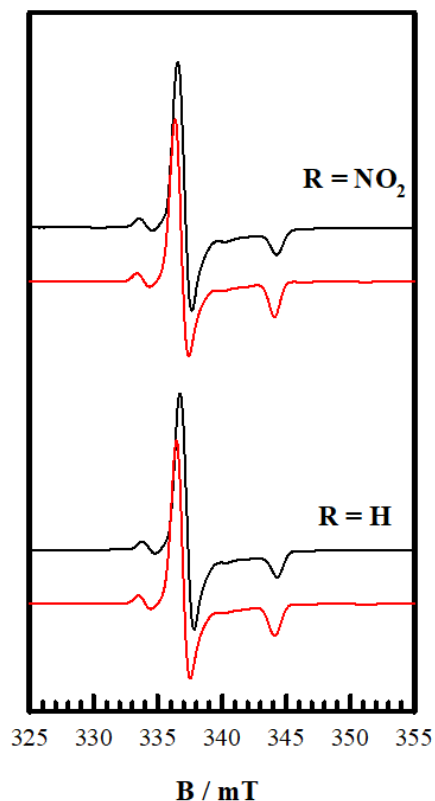


**Figure 2.10.** Frozen EPR spectra for CrNSal<sup>R</sup> where R = NO<sub>2</sub>, H (black = experiment, red = simulated). Conditions: T = 77 K; 0.45 mM complex; 0.1 M TBAP. See Table 2.1 for full instrumentation details,  $g$ -values and hyperfine couplings.

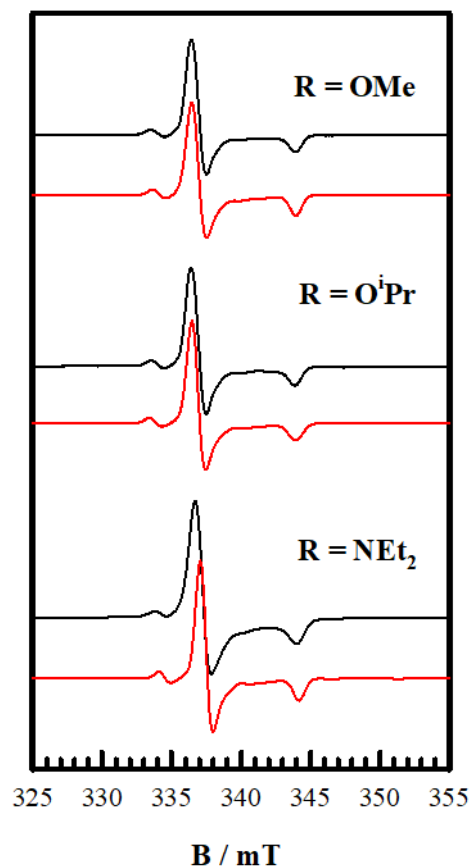


Figure 2.11. Frozen EPR spectra for CrNSal<sup>R</sup> where R = OMe, O<sup>i</sup>Pr, NEt<sub>2</sub> (black = experiment, red = simulated). Conditions: T = 77 K; 0.45 mM complex; 0.1 M TBAP. See Table 2.1 for full instrumentation details, *g*-values and hyperfine couplings.

Table 2.2. Full instrumentation details for EPR analysis of CrNSal<sup>R</sup> (R = NO<sub>2</sub>, H, OMe, O<sup>i</sup>Pr, NEt<sub>2</sub>).

Complex	<i>g</i> <sub>⊥</sub>	A <sup>53</sup> Cr (MHz)	<i>g</i> <sub>  </sub>	A <sup>53</sup> Cr (MHz)	Freq. (MHz)	Power (mW)	Mod. Freq. (kHz)	Mod. Amp. (GHz)
CrNSal <sup>NO<sub>2</sub></sup>	1.994	53	1.951	130	9.394	2.000	100	3.0
CrNSal <sup>H</sup>	1.994	53	1.951	130	9.397	2.000	100	3.0
CrNSal <sup>OMe</sup>	1.992	50	1.950	130	9.388	2.000	100	1.0
CrNSal <sup>O<sup>i</sup>Pr</sup>	1.992	55	1.950	130	9.387	2.000	100	6.0
CrNSal <sup>NEt<sub>2</sub></sup>	1.990	53	1.950	130	9.394	5.024	100	10



## 2.2.5. Electronic Absorption Spectroscopy

UV-vis-NIR spectroscopy was used to verify the electronic structure of neutral CrNSal<sup>R</sup>. Spectra for all CrNSal<sup>R</sup> complexes are shown in Figures 2.12 and 2.13, and key data is recorded in Table 2.3. The visible range absorbance from 17,500 cm<sup>-1</sup> to 27,500 cm<sup>-1</sup> can be attributed to a combination of ligand-to-metal charge transfer (LMCT) and  $\pi \rightarrow \pi^*$  transitions of the salen ligands.<sup>98</sup> This visible range absorbance shifts to higher energies as the electron withdrawing strength of the *para* substituent increases, supporting this LMCT assignment. In addition, weak absorbances in the visible region can be observed around 18,000 cm<sup>-1</sup> for all complexes except CrNSal<sup>NMe<sub>2</sub></sup> and CrNSal<sup>NEt<sub>2</sub></sup>, and there is little shift in the energy of this band with the R-group substituent of the salen ligand. The weak absorbance of this band and energetic R-group independence is consistent with a Laporte forbidden  $d \rightarrow d$  transition from the non-bonding  $d_{xy}$  orbital into the  $\pi^*$  orbitals of  $d_{xz}$  and  $d_{yz}$  character.<sup>144</sup> This transition may not be observed for the R = NMe<sub>2</sub> and R = NEt<sub>2</sub> derivatives due to the broadness of the LMCT into the 18,000 cm<sup>-1</sup> energy range.

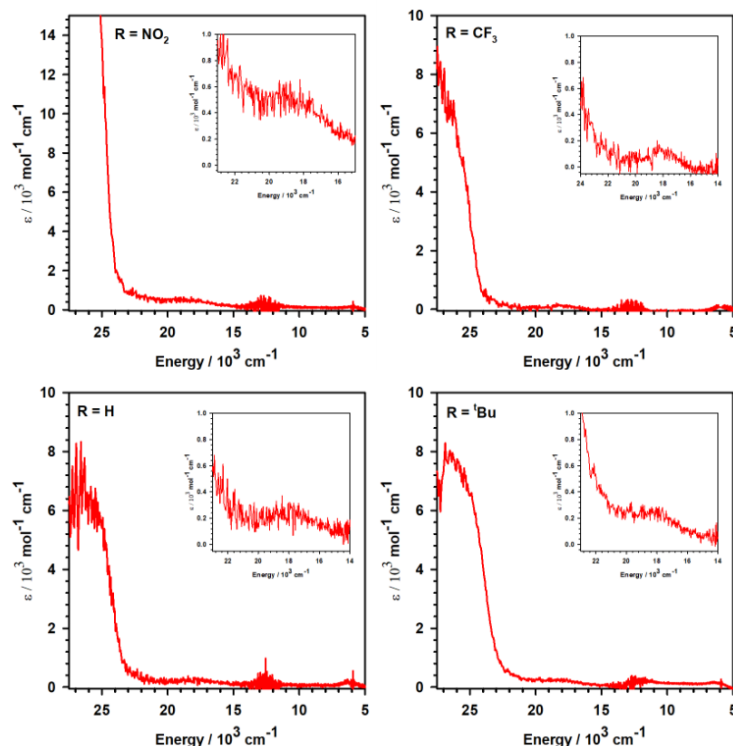


**Figure 2.12.** UV-vis-NIR spectra for CrNSal<sup>NO<sub>2</sub></sup>, CrNSal<sup>CF<sub>3</sub></sup>, CrNSal<sup>H</sup> and CrNSal<sup>tBu</sup>. Inset is zoomed in view of  $d \rightarrow d$  transitions. Conditions: 0.45 mM complex; T = 253 K; CH<sub>2</sub>Cl<sub>2</sub>.

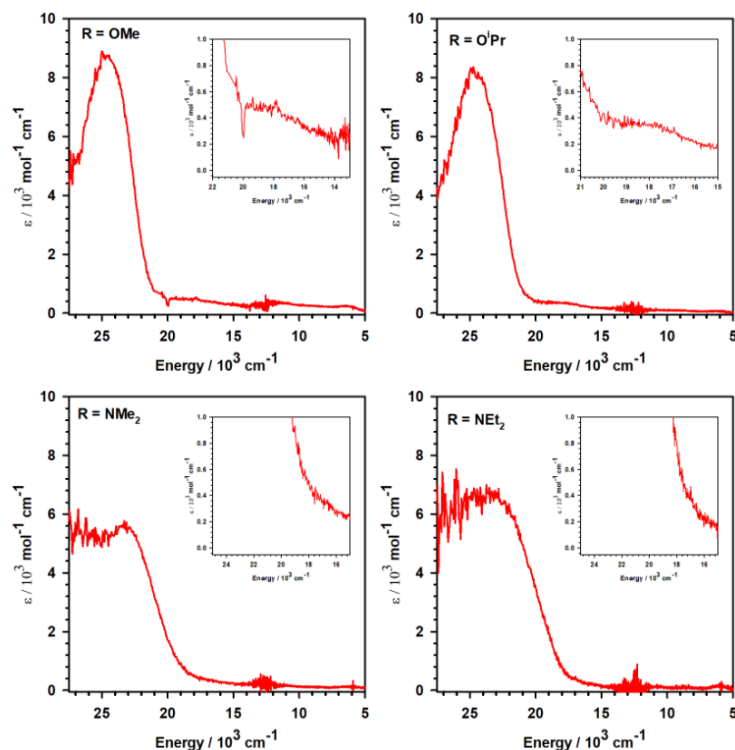


Figure 2.13. UV-vis-NIR spectra for CrNSal<sup>OMe</sup>, CrNSal<sup>O'Pr</sup>, CrNSal<sup>NMe<sub>2</sub></sup> and CrNSal<sup>NEt<sub>2</sub></sup>. Inset is zoomed in view of the  $d \rightarrow d$  transition (note that for R = NMe<sub>2</sub> and NEt<sub>2</sub>, the  $d \rightarrow d$  transition is likely hidden by the broad LMCT band). Conditions: 0.45 mM complex; T = 253 K; CH<sub>2</sub>Cl<sub>2</sub>.

Table 2.3. Key UV-vis-NIR spectroscopic information for CrNSal<sup>R</sup>.

Complex	$\lambda_{\max} / 10^3 \text{ cm}^{-1}$ ( $\epsilon / 10^3 \text{ M}^{-1} \text{ cm}^{-1}$ )
CrNSal <sup>NO<sub>2</sub></sup>	26.5 (27.3), 18.3 (0.4)
CrNSal <sup>CF<sub>3</sub></sup>	27.5 (8.1), 18.0 (0.3)
CrNSal <sup>H</sup>	26.3 (6.4), 18.0 (0.3)
CrNSal <sup>tBu</sup>	25.5 (7.8), 18.0 (0.3)
CrNSal <sup>OMe</sup>	24.6 (8.7), 17.9 (0.5)
CrNSal <sup>O'Pr</sup>	24.7 (8.2), 17.7 (0.3)
CrNSal <sup>NMe<sub>2</sub></sup>	23.3 (6.4)
CrNSal <sup>NEt<sub>2</sub></sup>	23.5 (6.7)

## 2.2.6. Theoretical Analysis

Density functional theory (DFT) was used to obtain optimized geometries. The UB3LYP functional and 6-31g\* basis set employed the polarizable continuum model (PCM) with DCM as solvent. This functional/basis set combination has been previously observed to afford good correlation with experimental metrical parameters.<sup>104,106,108</sup> A frequency job at the same level of theory verified the structure was at the true energetic minimum. As discussed in Chapter 2.2.2 and shown in Table 2.4 below, predicted bond lengths closely match those determined experimentally and all are within 0.04 Å of each other.

**Table 2.4. Predicted and experimental (parentheses) coordination sphere bond lengths (Å) for CrNSal<sup>R</sup>. Refer to Figures 2.5-2.9 for atom numbering scheme.**

Complex	Cr1-O1	Cr1-O2	Cr1-N1	Cr1-N2	Cr1-N3	O1-C1	O2-C2
<b>CrNSal<sup>NO2</sup></b>	1.932	1.941	2.027	2.037	1.519	1.302	1.303
	(1.906)	(1.910)	(2.002)	(2.015)	(1.560)	(1.314)	(1.314)
<b>CrNSal<sup>CF3</sup></b>	1.927	1.936	2.028	2.037	1.521	1.309	1.310
	(1.909)	(1.909)	(2.010)	(2.021)	(1.540)	(1.307)	(1.311)
<b>CrNSal<sup>H</sup></b>	1.922	1.930	2.029	2.041	1.523	1.315	1.316
	(1.896)	(1.915)	(2.008)	(2.031)	(1.549)	(1.316)	(1.317)
<b>CrNSal<sup>tBu</sup></b>	1.922	1.930	2.029	2.038	1.524	1.316	1.316
	(1.909)	(1.898)	(2.008)	(2.019)	(1.549)	(1.314)	(1.307)
<b>CrNSal<sup>OMe</sup></b>	1.916	1.925	2.034	2.043	1.524	1.320	1.321
	(1.907)	(1.911)	(2.006)	(2.010)	(1.556)	(1.317)	(1.318)
<b>CrNSal<sup>OiPr</sup></b>	1.919	1.928	2.030	2.038	1.525	1.318	1.318
	(1.845)	(1.922)	(2.040)	(2.045)	(1.536)	(1.309)	(1.309)
<b>CrNSal<sup>NMe2</sup></b>	1.919	1.928	2.029	2.038	1.525	1.317	1.318
	(1.911)	(1.906)	(2.013)	(2.004)	(1.544)	(1.305)	(1.323)
<b>CrNSal<sup>NEt2</sup></b>	1.914	1.923	2.033	2.042	1.526	1.323	1.323
	-	-	-	-	-	-	-

Spin density and singly occupied molecular orbital (SOMO) plots also provide insight into the location of the unpaired *d* electron. Example plots for CrNSal<sup>NEt<sub>2</sub></sup> are shown below in Figure 2.14 (see Figures A1 to A4 for spin density and SOMO plots for additional novel complexes). In all cases, spin density is located on the Cr metal center and the nitride ligand. Spin density values on the nitride ligand and Cr are similar regardless of R-group. Plots of the SOMO depict the single *d* electron is located in the Cr *d<sub>xy</sub>* orbital which does not participate in bonding to the nitride ligand.

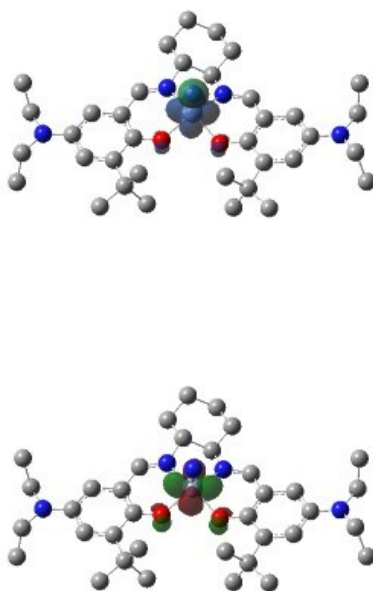


**Figure 2.14. Spin density (top) and SOMO (bottom) plots for CrNSal<sup>NEt<sub>2</sub></sup>. All R-group derivatives exhibit similar plots (Figures A1-A4).**

## 2.3. Conclusion

Novel CrNSal<sup>R</sup> (R = NO<sub>2</sub>, H, OMe, O<sup>i</sup>Pr, NEt<sub>2</sub>) were synthesized according to previously established intermetal N-atom transfer methods. XRD, ESI-MS and elemental analysis are consistent with target complex structures. Evan's method NMR and EPR also predict one unpaired electron. Theoretical analysis also showed good agreement between optimized structures and crystal structures, providing further evidence that the target nitride complexes have been isolated, and useful data to compare to the oxidized forms.

Chapter 3 will focus on the electronic structure of the novel complexes upon chemical oxidation using electrochemistry, UV-vis-NIR, EPR and computational methods.

## 2.4. Experimental

### 2.4.1. Materials

All chemicals used were obtained from commercial suppliers and used without any further purification unless noted otherwise. All ligands and  $\text{MnNSal}^{\text{H}}$  were synthesized according to literature procedures.<sup>107,122,131–137</sup> Dry tetrahydrofuran was obtained by refluxing over sodium in the presence of benzophenone under  $\text{N}_2$ . Dry acetonitrile was obtained by refluxing over calcium hydride under  $\text{N}_2$ .

### 2.4.2. Instrumentation

EPR spectra were collected on a Bruker EMXplus spectrometer operating with a premium X-band microwave bridge and HS resonator. UV-vis-NIR data was collected on a Cary 5000 spectrophotometer equipped with custom designed immersion fiber-optic probes with a 1 mm path length. Constant temperatures were maintained with an FTS Multi-Cool Low Temperature Bath. ESI-MS was performed using an Agilent 6210 TOF ESI-MS system. Elemental analysis was performed by Carol Wu using an EA CHN 1110 analyzer. Evan's method  $^1\text{H}$  NMR spectra were collected on a Bruker AVANCE III 500 MHz instrument.

### 2.4.3. Syntheses

**Synthesis of  $\text{CrNSal}^{\text{NO}_2}$ :** Under a nitrogen atmosphere, 0.214 g (0.571 mmol) of  $\text{CrCl}_3 \cdot \text{THF}$  and 0.192 g (0.572 mmol) of  $\text{MnNSal}^{\text{H}}$  were dissolved in 2 mL of acetonitrile and stirred for 1 hour. 0.200 g (0.381 mmol) of  $\text{H}_2\text{Sal}^{\text{NO}_2}$  was dissolved in 2 mL of 1:1 dichloromethane/acetonitrile and 8 drops of  $\text{NEt}_3$  and added dropwise to the  $[\text{CrN}]$  solution. After refluxing 1 hour, a precipitate formed, and the suspension was placed in a  $-20$  °C freezer. The precipitate was collected by vacuum filtration and washed with 2 x 10mL cold acetonitrile.  $\text{CrNSal}^{\text{NO}_2}$  was isolated as a purple-brown solid. Yield 0.085 g (0.144 mmol, 38%). ESI-MS (negative mode)  $m/z$ :  $\{\text{M}+\text{H}_2\text{O}+\text{MeCN}\}^-$  647.23 100%. Anal.

Calcd (%)  $C_{28}H_{34}CrN_5O_6 \cdot 0.5H_2O$ : C 56.28, H 5.90, N 11.72; Found (%): C 56.23, H 5.82, N 11.76.  $\mu_{\text{eff}} = 1.86$  (Evans method).

**Synthesis of CrNSal<sup>H</sup>:** Under a nitrogen atmosphere, 0.259 g (0.691 mmol) of  $CrCl_3 \cdot THF$  and 0.231 g (0.689 mmol) of  $MnNSal^H$  were dissolved in 2 mL of acetonitrile and stirred for 1 hour. 0.200 g (0.460 mmol) of  $H_2Sal^H$  was dissolved in 2 mL of 1:1 dichloromethane/acetonitrile and added dropwise to the [CrN] solution. After stirring 1 hour, a precipitate formed and 0.128 mL of  $NEt_3$  was added. The suspension was stirred overnight, then concentrated *in vacuo*. The crude product was purified by column chromatography using dichloromethane as eluent ( $R_f$  0.7).  $CrNSal^H$  was isolated as a tan solid. Yield 0.050 g (0.100 mmol, 22%). ESI-MS  $m/z$ : 499.23 {M+H}<sup>+</sup> 100%. Anal. Calcd (%)  $C_{28}H_{36}CrN_3O_2$ : C 67.45, H 7.28, N 8.43; Found (%): C 67.32, H 7.35, N 8.21.  $\mu_{\text{eff}} = 1.98$  (Evans method).

**Synthesis of CrNSal<sup>OMe</sup>:** To a yellow solution of 0.500 g  $H_2Sal^{OMe}$  (1.01 mmol) in 10 mL tetrahydrofuran was added 0.149 g  $CrCl_2$  (1.212 mmol) and the reaction was stirred overnight under inert atmosphere. 30 mL of saturated ammonium chloride was added and stirred for 2 hours in air, followed by the addition of 25 mL of brine. The organic layer was dried over sodium sulfate, filtered and removed *in vacuo* to yield 0.500 g (0.862 mmol) of crude  $CrClSal^{OMe}$  intermediate. The intermediate was dissolved in 30 mL dichloromethane and 0.347 g of  $MnNSal^H$  (1.035 mmol) was added, refluxed for 1 hour, and the solvent was removed *in vacuo*. The crude product was purified by silica gel column chromatography using dichloromethane as the eluent ( $R_f$  0.4).  $CrNSal^{OMe}$  was isolated as a yellow-brown powder. Yield 0.209 g (0.374 mmol, 37%). ESI-MS  $m/z$ : 559.23 {M+H}<sup>+</sup> 100%. Anal. Calcd (%)  $C_{30}H_{40}CrN_3O_4$ : C 64.50, H 7.22, N 7.52; Found (%): 64.43, H 7.32, N 7.20  $\mu_{\text{eff}} = 1.71$  (Evans method).

**Synthesis of CrNSal<sup>O<sup>i</sup>Pr</sup>:** To a yellow solution of 1.000 g  $H_2Sal^{O^iPr}$  (1.82 mmol) in 20 mL tetrahydrofuran was added 0.268 g  $CrCl_2$  (1.82 mmol) and the reaction was stirred overnight under inert atmosphere. 30 mL of saturated ammonium chloride was then added and stirred for 2 hours in air, followed by the addition of 25 mL of brine. The organic layer was dried over sodium sulfate, filtered, and removed *in vacuo* to yield 0.670 g (1.05 mmol) of crude  $CrClSal^{O^iPr}$  intermediate. The intermediate was dissolved in 30 mL dichloromethane and 0.359 g of  $MnNSal^H$  (1.07 mmol) was added, refluxed for 1 hour, and the solvent was removed *in vacuo*. The crude product was purified by silica gel column

chromatography using dichloromethane as the eluent (Rf 0.3). CrNSal<sup>O<sup>IPr</sup></sup> was isolated as a yellow-brown powder. Yield 0.430 g (0.70 mmol, 38%). ESI-MS m/z: 615.31 {M+H}<sup>+</sup> 100%. Anal. Calcd (%) C<sub>34</sub>H<sub>48</sub>CrN<sub>3</sub>O<sub>4</sub>•0.5H<sub>2</sub>O: C 65.47, H 7.92, N 6.74; Found (%): C 65.59, H 7.53, N 6.24  $\mu_{\text{eff}} = 2.04$  (Evans method).

**Synthesis of CrNSal<sup>NEt<sub>2</sub></sup>:** To a yellow solution of 0.200 g H<sub>2</sub>Sal<sup>NEt<sub>2</sub></sup> (0.347 mmol) in 20 mL tetrahydrofuran was added 0.051 g CrCl<sub>2</sub> (0.407 mmol) and stirred overnight under inert atmosphere. 30 mL of saturated ammonium chloride was then added and stirred for 2 hours in air, followed by the addition of 25 mL of brine. The organic layer was dried over sodium sulfate, filtered, and removed *in vacuo* to yield 0.227 g (0.343 mmol) of crude CrClSal<sup>NEt<sub>2</sub></sup> intermediate. The intermediate was dissolved in 30 mL dichloromethane and 0.127 g MnSal<sup>H</sup>N (0.379 mmol) was added, refluxed for 1 hour, and the solvent was removed *in vacuo*. The crude product was purified by silica gel column chromatography using 1% triethylamine/dichloromethane as the eluent (Rf 0.4). CrNSal<sup>NEt<sub>2</sub></sup> was isolated as an orange-brown powder. Yield 0.096 g (0.150 mmol, 43%). ESI-MS m/z: 641.39 {M+H}<sup>+</sup> 100%. Anal. Calcd (%) C<sub>36</sub>H<sub>52</sub>CrN<sub>3</sub>O<sub>2</sub>: C 67.47, H 8.49, N 10.93; Found (%): C 67.29, H 8.42, N 10.72.  $\mu_{\text{eff}} = 1.96$  (Evans method).

#### 2.4.4. X-ray Structure Determination

All crystals were mounted on a 150 mm MiTeGen Dual-Thickness MicroMount using Paratone oil and measurements were made on a Bruker Photon II diffractometer with TRIUMPH-monochromated Mo K $\alpha$  radiation (sealed tube) or Cu K $\alpha$  radiation (Cu-micro source). The data were collected at a temperature of 298 K in a series of scans in 0.50° oscillations. Data were collected and integrated using the Bruker SAINT software package and were corrected for absorption effects using the multi-scan technique (SADABS) or (TWINABS).<sup>145–148</sup> All structures were solved by direct methods and refined using SIR97 and SIR92.<sup>149,150</sup> All non-hydrogen atoms were refined anisotropically. All hydrogen atoms were placed in calculated positions but not refined. All refinements were performed using the SHELXTL crystallographic software package of Bruker-AXS.<sup>151</sup> The molecular drawings were generated using POV and ORTEP.<sup>152</sup>

### **2.4.5. Theoretical Analysis**

All theoretical analyses were performed using Gaussian 16 (version C.01) software using Digital Research Alliance of Canada cluster resources. All analyses used the polarizable continuum model (PCM) with DCM ( $\epsilon=8.93$ ) as the solvent. Optimizations and frequency calculations were performed using the UB3LYP functional and 6-31g\* basis set. Single point energies and NBO calculations were determined using the UBLYP functional and TZVP basis set.



## Chapter 3. Electronic Structure of [CrSal<sup>R</sup>N]<sup>+</sup> (R = NO<sub>2</sub>, H, <sup>t</sup>Bu, OMe, O<sup>i</sup>Pr, NEt<sub>2</sub>)

W. VandeVen performed electrochemistry, chemical oxidation titrations, and DFT studies. Data for CrNSal<sup>CF<sub>3</sub></sup>, CrNSal<sup><sup>t</sup>Bu</sup> and CrNSal<sup>NMe<sub>2</sub></sup> was reported previously by D. Martelino *et al.*<sup>108</sup> G. MacNeil collected EPR data using the Walsby Group spectrometer.

### 3.1. Introduction

The redox-active nature of salen ligands makes them attractive as described in previous chapters, but also presents challenges when determining the locus of oxidation or reduction. In addition to ambiguity of whether the electron transfer occurred at the metal or ligand, the degree of delocalization between the metal and ligand, as well as the ligand itself, can also complicate electronic structure assignment. Robin & Day developed a classification system for redox-ambiguous bimetallic compounds in 1968, separating them into Class I, II, or III, though this nomenclature can be extended to other non-innocent systems.<sup>153</sup> Class I systems have a large energy barrier to intramolecular electron transfer, usually containing metal ions in significantly different coordination spheres and/or the bridge cannot mediate electronic coupling. Class II complexes exhibit intermediate delocalization and the energetic barrier to electron transfer allows detection of different oxidation states. One of the earliest examples of Class II complexes include Cowan's biferrocene shown in Figure 3.1A.<sup>154,155</sup> Finally, Class III complexes contain metal centers in very similar or identical coordination environments such that there is complete delocalization between the metal centers, and the oxidation states are averaged across the system. One of the most well-known examples of a Class III system is the Creutz-Taube dinuclear Ru complex, in which each Ru center has a 2.5+ oxidation state, rather than a 2+ and 3+ Ru center based on a Class I assignment (Figure 3.1B).<sup>156,157</sup> Further subdivision of these classes since highlights the complexity and challenges of these systems.<sup>158,159</sup> Multiple spectroscopies and techniques are required to make an assignment, and there is often some inherent uncertainty.

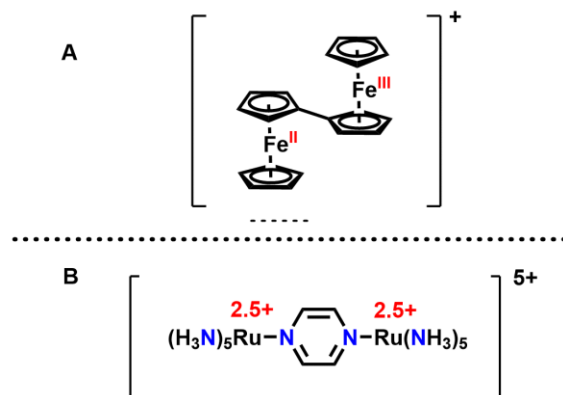


**Figure 3.1.** Examples of mixed-valence species. Class II species such as Crowan's biferrocene cannot readily exchange electrons between metal centers (A).<sup>154,155</sup> Class III species such as the Taube ion have fully delocalized electronic structures and metal center oxidation states are indistinguishable (B).<sup>156,157</sup>

Paramount to this work, transition metal salen complexes are redox-active as discussed in Section 1.4, and ligand radical salen complexes typically fall in between Class II and Class III.<sup>98</sup> Electrochemistry, EPR, UV-vis-NIR, and DFT studies will be combined to assess the locus of oxidation upon oxidation of the Cr(V) salen nitrides discussed in Chapter 2, as well as determine the extent of delocalization for potential ligand radical species (Figures 3.2 and 3.3).

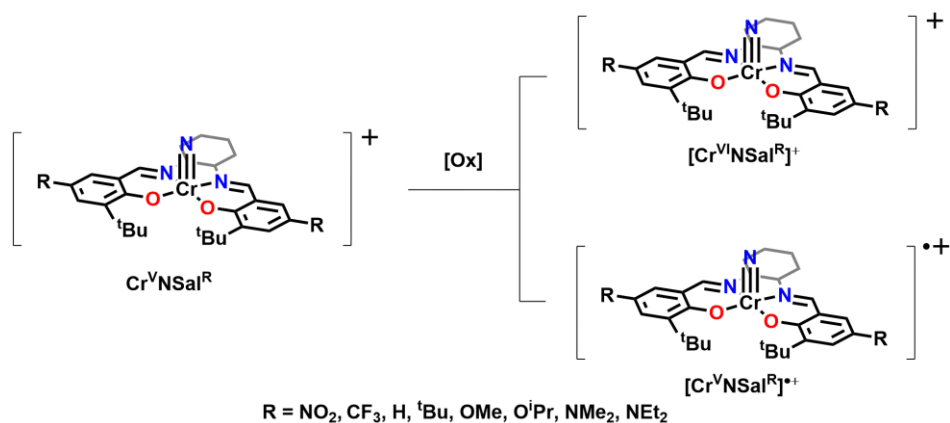


**Figure 3.2.** Oxidation of Cr<sup>V</sup>NSal<sup>R</sup> will yield high-valent metal [Cr<sup>VI</sup>NSal<sup>R</sup>]<sup>+</sup> or ligand radical [Cr<sup>V</sup>NSal<sup>R</sup>]<sup>•+</sup> complexes depending on the *para* R-group substituent.

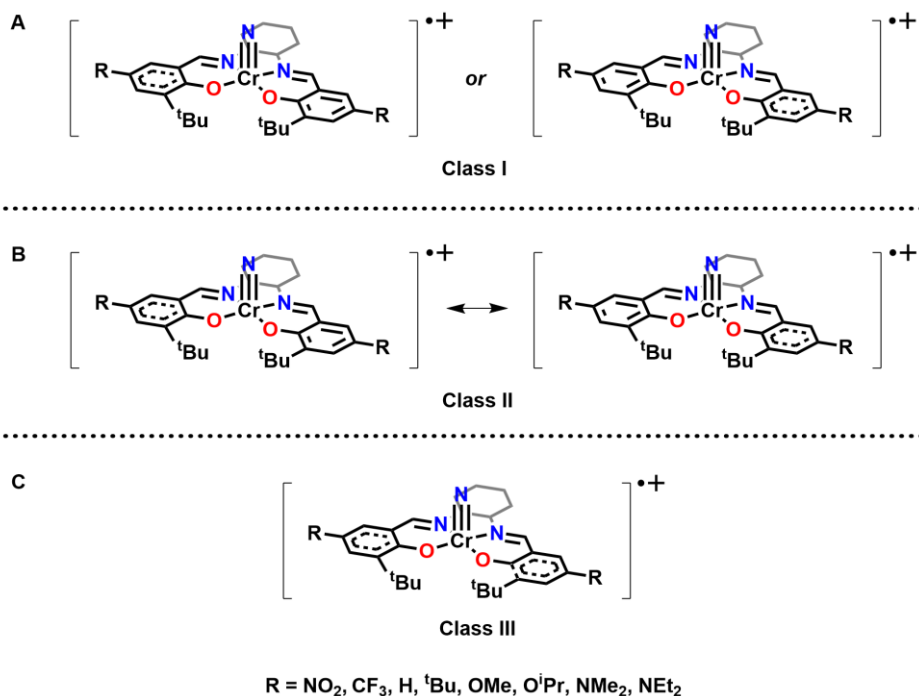


**Figure 3.3.** Potential Robin-Day classifications for ligand radical salen complexes. No coupling occurs between the aromatic rings for Class I (A). Limited coupling occurs between the aromatic rings for Class II (B), and full delocalization between the aromatic rings occurs for Class III systems (C).

## 3.2. Results

### 3.2.1. Electrochemistry

Redox processes for CrNSal<sup>R</sup> were investigated using cyclic voltammetry. Upon scanning to higher potentials, the first redox event for each complex is in agreement with the  $\sigma_p$  value of the R group substituent (Figures 3.4 and 3.5, Table 3.1). All complexes feature reversible first oxidation events, except for CrNSal<sup>H</sup> which exhibits a quasi-reversible wave based on the ratio of peak current ( $I_{pa}/I_{pc}$ ). Notably, the stronger electron-donating groups feature multiple reversible redox waves (only the first two are shown in Figure 3.3; see Appendix B - Figures B1 to B5 for full scan windows for all complexes), with CrNSal<sup>NEt<sub>2</sub></sup> exhibiting four redox events. CrNSal<sup>NO<sub>2</sub></sup> also features a reduction at very low potentials which is not observed in any of the other complexes. Due to the electron-withdrawing nature of the nitro group, it is likely that the Cr(V)/Cr(IV) couple is now observed in the electrochemical window.

As discussed in Section 2.2.1, the literature reports the  $\sigma_p$  value of the  $\text{NEt}_2$  groups as -0.73 whereas the  $\text{NMe}_2$  group has  $\sigma_p$  value of -0.83.<sup>105</sup> This assignment is incorrect based on the electrochemistry data for the two complexes, as the first redox process for  $\text{CrNSal}^{\text{NEt}_2}$  occurs at significantly lower potentials ( $\sim 0.18$  V more negative) than  $\text{CrNSal}^{\text{NMe}_2}$  (Figure 3.5). Moreover, the substitution of methyl groups for ethyl groups are expected to increase the donation of the amine groups into the aromatic rings via an inductive effect. Therefore, we propose a  $\sigma_p$  value of -0.93 for the  $\text{NEt}_2$  group in accordance with previously reported differences in  $\sigma_p$  value and to maintain consistency within the current Hammett parameter scheme.<sup>138,139</sup>

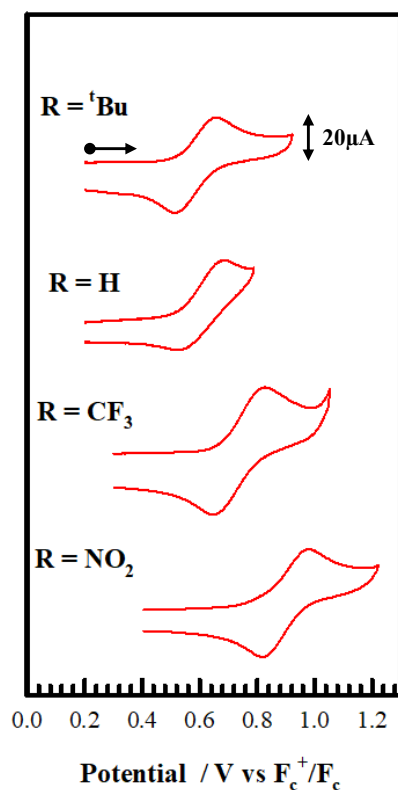


**Figure 3.4.** Cyclic voltammograms of first redox events for  $\text{CrNSal}^{t\text{Bu}}$ ,  $\text{CrNSal}^{\text{H}}$ ,  $\text{CrNSal}^{\text{CF}_3}$  and  $\text{CrNSal}^{\text{NO}_2}$ . Conditions: 0.1 M TBAP;  $\text{CH}_2\text{Cl}_2$ ; 1 mM complex; T = 298 K; scan rate = 100 mV/s.

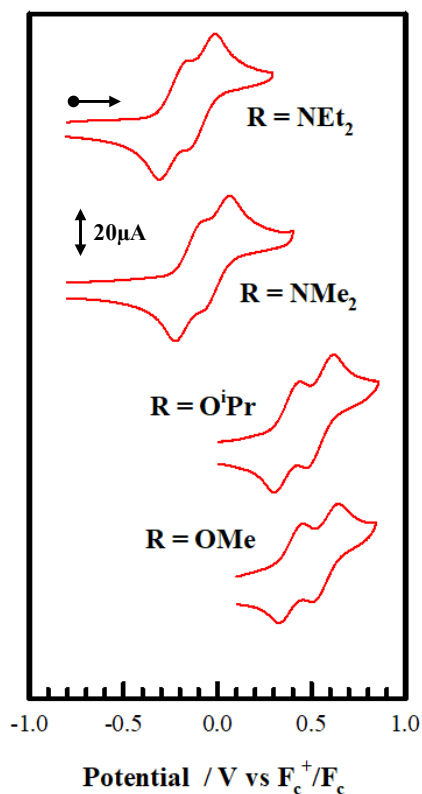


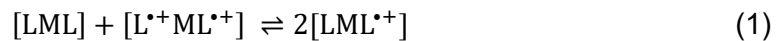
Figure 3.5. Cyclic voltammograms of first redox events for CrNSal<sup>NEt<sub>2</sub></sup>, CrNSal<sup>NMe<sub>2</sub></sup>, CrNSal<sup>O<sup>i</sup>Pr</sup> and CrNSal<sup>OMe</sup>. Conditions: 0.1 M TBAP; CH<sub>2</sub>Cl<sub>2</sub>; 1 mM complex; T = 298 K; scan rate = 100 mV/s.

Table 3.1. Tabulated redox potentials for CrNSalR vs F<sub>c</sub><sup>+</sup>/F<sub>c</sub> in volts. Peak-to-peak separation in parentheses. Only the first two redox events (as applicable) are included.

Compound	$\sigma_p$	$E_{pa}^1$	$E_{pc}^1$	$E_{1/2}^1$	$E_{pa}^2$	$E_{pc}^2$	$E_{1/2}^2$
CrNSal <sup>NO<sub>2</sub></sup>	0.78	0.83	0.99	0.91 (0.16)	-	-	-
CrNSal <sup>CF<sub>3</sub></sup>	0.54	0.75	0.98	0.87 (0.23)	-	-	-
CrNSal <sup>H</sup>	0.00	0.54	0.69	0.62 (0.15)	-	-	-
CrNSal <sup>tBu</sup>	-0.20	0.51	0.70	0.61 (0.19)	-	-	-
CrNSal <sup>OMe</sup>	-0.27	0.34	0.46	0.40 (0.12)	0.53	0.65	0.59 (0.12)
CrNSal <sup>O<sup>i</sup>Pr</sup>	-0.45	0.31	0.45	0.38 (0.14)	0.48	0.62	0.55 (0.14)
CrNSal <sup>NMe<sub>2</sub></sup>	-0.83	-0.12	0.05	-0.04 (0.17)	0.03	0.20	0.12 (0.17)
CrNSal <sup>NEt<sub>2</sub></sup>	-0.93	-0.30	-0.15	-0.23 (0.12)	-0.14	-0.01	-0.08 (0.13)

To gain further insight into the electronic structure of the complexes, differential pulse voltammetry (DPV) was used to resolve poorly separated redox events for CrNSal<sup>OMe</sup>, CrNSal<sup>OiPr</sup>, CrSal<sup>NMe2</sup> and CrSal<sup>NEt2</sup>. Stack plots of the full cyclic voltammogram and DPV scan are shown in Figure 3.6.  $\Delta E_{ox}$  values and comproportionation constants  $K_c$  are tabulated in Table 3.2 (Equations 1-3). CrNSal<sup>OMe</sup> and CrNSal<sup>OiPr</sup> undergo two reversible redox events, CrSal<sup>NMe2</sup> exhibits three redox processes, and CrSal<sup>NEt2</sup> undergoes four one-electron redox events. However, the sharp peak observed in the reverse scan at 0.6V for CrSal<sup>NEt2</sup> cannot be conclusively assigned as a one electron transfer. If the ligand radical is delocalized it would be difficult to oxidize a second time. If not delocalized, there is little to no communication and thus the oxidations should occur at similar potentials. Based on the small  $\Delta E_{ox}$  values for CrNSal<sup>NMe2</sup> and CrNSal<sup>NEt2</sup>, these compounds likely exhibit strong radical localization upon oxidation.<sup>160</sup> Further analysis of doubly-oxidized CrNSal<sup>NMe2</sup> previously established that both electrochemical events are ligand-based.<sup>108</sup> Furthermore, studies of Ni, uranyl and Mn nitride complexes containing R = NMe<sub>2</sub> salen ligands show similar cyclic voltammograms.<sup>94,106,136</sup> Therefore, we expect a similar electronic structure for CrNSal<sup>NEt2</sup> upon oxidation. While further oxidations at higher potentials have not been investigated, these could be metal-based to form Cr<sup>VI</sup> and/or sequential oxidations of the ligand to form quinone-like species.

Interestingly, both CrNSal<sup>OMe</sup> and CrNSal<sup>OiPr</sup> display two reversible redox events at relatively low potentials, in comparison to the MnN complexes of the same ligands which show only one quasi-reversible feature at low temperature, which results in a metal-based oxidation to Mn<sup>VI</sup>.<sup>107</sup> However, due to relatively fast homocoupling, the second feature for the Mn analogues is much weaker.<sup>107</sup>  $\Delta E_{ox}$  and comproportionation equilibrium constant values  $K_c$  (Equations 1-3) are higher for the R = OMe and R = OiPr derivatives in comparison to the R = NMe<sub>2</sub> and NEt<sub>2</sub> derivatives, which could indicate that the presence of alkoxy groups results in a more delocalized ligand radical upon oxidation, or alternatively, that the first oxidation is metal-based (Table 3.2). Thus, the electrochemistry data for CrNSal<sup>OMe</sup> and CrNSal<sup>OiPr</sup> do not provide a definitive assignment of the locus of oxidation (either metal- or ligand-based), and further investigation is required to make an assignment for these derivatives.



$$K_c = \frac{[\text{LML}^{\bullet+}]^2}{[\text{LML}][\text{L}^+\text{ML}^+]} \quad (2)$$

$$K_c = \exp\left(\frac{\Delta E_{\text{ox}} F}{RT}\right) \quad (3)$$

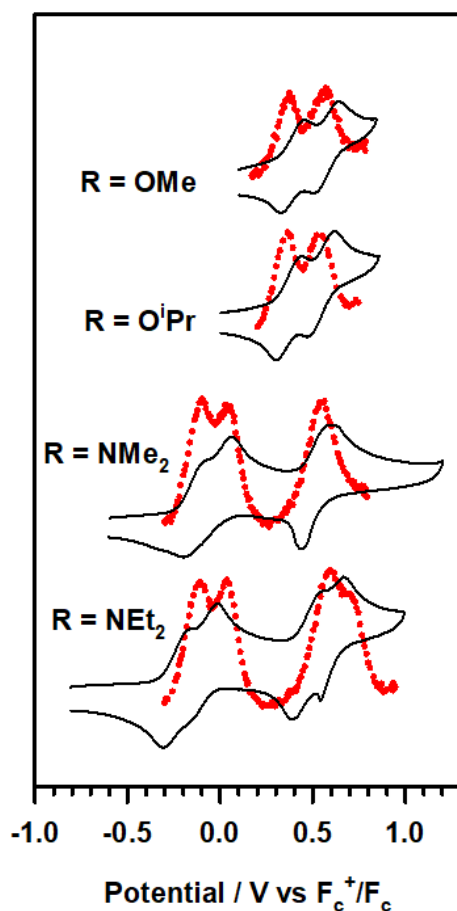


Figure 3.6. Stacked plots of cyclic voltammograms (black) and differential pulse voltammograms (red) for  $\text{CrNSal}^{\text{OMe}}$ ,  $\text{CrNSal}^{\text{O}^i\text{Pr}}$ ,  $\text{CrNSal}^{\text{NMe}_2}$  and  $\text{CrNSal}^{\text{NEt}_2}$ . Conditions: 1mM complex; 0.1 M TBAP; T = 293 K,  $\text{CH}_2\text{Cl}_2$ .

**Table 3.2.  $\Delta E_{ox}$  and  $K_c$  values for obtained from differential pulse voltammetry.**

Complex	$\Delta E_{ox} / V$	$K_c$
CrNSal <sup>OMe</sup>	0.198	2222
CrNSal <sup>O<sup>i</sup>Pr</sup>	0.180	1103
CrNSal <sup>NMe<sub>2</sub></sup>	0.140	232
CrNSal <sup>NEt<sub>2</sub></sup>	0.162	547

### 3.2.2. Electronic Absorption Spectroscopy

UV-vis-NIR spectroscopy was used to monitor changes in absorbance as neutral CrNSal<sup>R</sup> were oxidized and gain insight into the resulting electronic structure. Based on the high redox potentials for the less electron-donating R-groups ( $E_{1/2} = 0.91$  V vs.  $F_c^+/F_c$  for  $R = NO_2$ ), the oxidant magic green (Tris(2,4-dibromophenyl)aminium hexafluoroantimonate) ( $E_{1/2} = 1.1$  V vs.  $F_c^+/F_c$ ) was used to oxidize all complexes.<sup>161,162</sup> A standardized oxidant solution was titrated into a solution of neutral CrNSal<sup>R</sup> until one equivalent was reached, and the solutions of all compounds turned a darker colour. Isosbestic points indicate clean conversion to the oxidized species. All of the weaker donating ligands up to and including CrNSal<sup>O<sup>i</sup>Pr</sup> exhibit broad bands in the vis to NIR region (Figures 3.7 and 3.8), and these bands generally move to lower energy as the electron-donating ability of the *para*-ring substituent is increased (Table 3.3). This trend is consistent with a ligand-to-metal charge transfer (LMCT) assignment for this band, where the ligand donor orbital energy decreases as the donating ability of the *para*-ring substituent is lowered, while the acceptor orbital (Cr  $d_{xy}$ ) energy remains constant.<sup>144,163</sup> Thus, the UV-vis-NIR data is consistent with metal-based oxidation to Cr<sup>VI</sup> for [CrNSal<sup>R</sup>]<sup>+</sup> ( $R = NO_2, CF_3, H, tBu, OMe, O^iPr$ ). In addition, the alkoxy substituted CrNSal<sup>R</sup> ( $R = OMe, O^iPr, NEt_2$ ) feature a second oxidation process accessible with magic green. Discussion of these bis oxidized complexes is beyond the scope of this thesis, but spectra of these bis oxidized complexes are shown in Figures B6-B8.

In contrast, chemical oxidation of CrNSal<sup>NMe<sub>2</sub></sup> and CrNSal<sup>NEt<sub>2</sub></sup> results in spectra with significantly weaker bands in the NIR, and the visible region band centered around 23,000  $cm^{-1}$  shifts to two more absorption bands at lower energies (Figure 3.9). Again, similar visible region bands were also observed for oxidized Ni, uranyl and Mn nitride complexes



containing the R = NMe<sub>2</sub> salen ligands.<sup>94,106,108,136</sup> Given that these complexes as well as [CrNSal<sup>NMe<sub>2</sub></sup>]<sup>+</sup> were all assigned ligand radical structures, CrNSal<sup>NEt<sub>2</sub></sup> likely also forms a ligand radical after oxidation. With respect to delocalization, broad and weak absorptions in the NIR are associated with Class II systems, in comparison to Class III systems which exhibit sharp and intense absorptions in the NIR.<sup>78,160</sup> Taken together, this spectrum is indicative of a Class II ligand radical species [CrNSal<sup>NEt<sub>2</sub></sup>]<sup>•+</sup> with a ligand radical localized to one of the phenolate rings.

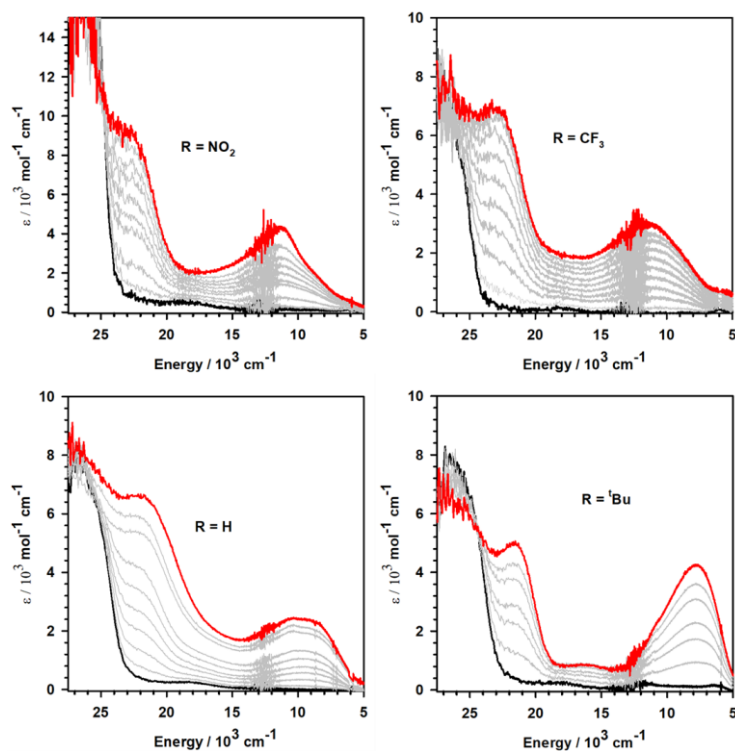


**Figure 3.7.** Magic green oxidant titrations monitored by UV-vis-NIR spectroscopy for CrNSal<sup>NO<sub>2</sub></sup>, CrNSal<sup>CF<sub>3</sub></sup>, CrNSal<sup>H</sup> and CrNSal<sup>tBu</sup>. Black = neutral; grey = intermediate aliquots of oxidant; red = one equivalent of oxidant. Conditions: 0.45 mM complex; T = 233 K; CH<sub>2</sub>Cl<sub>2</sub>.

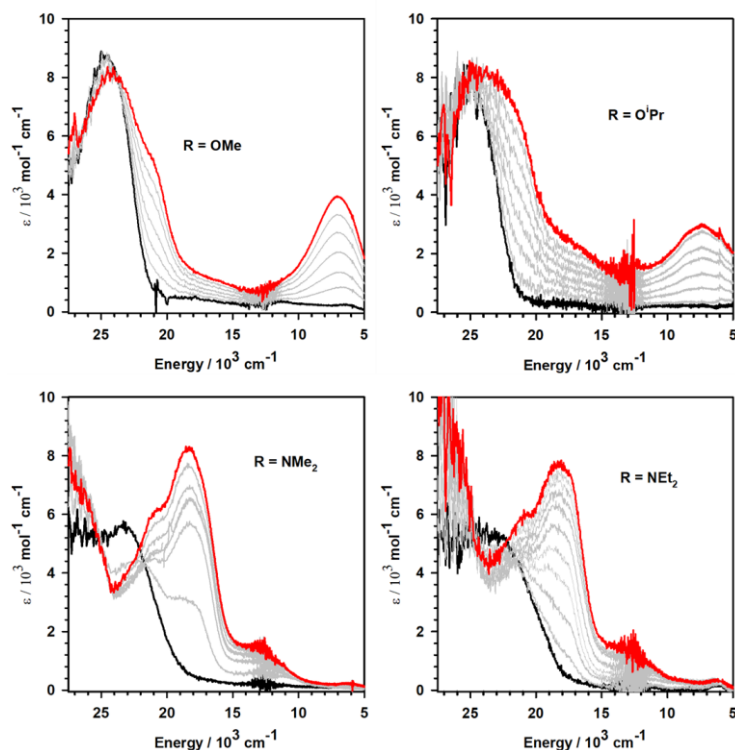


**Figure 3.8.** Magic green oxidant titrations monitored by UV-vis-NIR spectroscopy for CrNSal<sup>OMe</sup>, CrNSal<sup>O<sup>i</sup>Pr</sup>, CrNSal<sup>NMe<sub>2</sub></sup> and CrNSal<sup>NEt<sub>2</sub></sup>. Black = neutral; grey = intermediate aliquots of oxidant; red = one equivalent of oxidant. Conditions: 0.45 mM complex; T = 233 K; CH<sub>2</sub>Cl<sub>2</sub>.

**Table 3.3.** Key UV-vis-NIR data for [CrNSal<sup>R</sup>]<sup>+</sup>.

Complex	$\sigma_p$	$\lambda_{\max} / 10^3 \text{ cm}^{-1}$ ( $\epsilon / 10^3 \text{ M}^{-1} \text{ cm}^{-1}$ )
CrNSal <sup>NO<sub>2</sub></sup>	0.78	23.0 (9.3), 11.4 (4.3)
CrNSal <sup>CF<sub>3</sub></sup>	0.54	23.0 (5.8), 11.0 (2.2)
CrNSal <sup>H</sup>	0.00	22.2 (6.6), 9.9 (2.5)
CrNSal <sup>tBu</sup>	-0.20	21.9 (5.0), 8.1 (4.2)
CrNSal <sup>OMe</sup>	-0.27	24.2 (8.0), 7.0 (3.9)
CrNSal <sup>O<sup>i</sup>Pr</sup>	-0.45	23.9 (8.2), 7.3 (2.9)
CrNSal <sup>NMe<sub>2</sub></sup>	-0.83	21.3 (6.8), 18.8 (6.8), 11.5 (1.0)
CrNSal <sup>NEt<sub>2</sub></sup>	-0.93	20.9 (6.0), 18.2 (7.7), 12.7, (1.4)

### 3.2.3. Electron Paramagnetic Resonance

EPR was used to gain insight into the electronic structure of new complexes upon oxidation. As outlined in Chapter 2.2.3,  $\text{Cr}^{\text{V}}\text{NSal}^{\text{R}}$  are paramagnetic  $d^1$  species ( $S = 1/2$ ) exhibiting axial symmetry. If metal oxidation occurs, a diamagnetic  $d^0$   $\text{Cr}(\text{VI})$  species forms and no EPR signal should be observed. Ligand oxidation may also result in a loss of EPR signal depending on the strength of coupling between the  $d^1$  chromium center and ligand radical. In the case of a triplet spin state ( $S = 1$ ), the electron located in the Cr  $d_{xy}$  orbital ferromagnetically couples to the ligand radical. The resultant zero-field splitting can cause the energy of the EPR signals to fall outside the X-band frequency window.<sup>164–166</sup> The third case involves the antiferromagnetic coupling of the Cr  $d_{xy}$  electron and the ligand radical which can also result in a loss of EPR signal.<sup>167,168</sup>

A significant loss of EPR signal occurs upon oxidation of all the  $\text{CrNSal}^{\text{R}}$  complexes as observed in Figures 3.9 and 3.10. For  $\text{R} = \text{NO}_2$ , ~4 % of the signal remains, and close inspection of the spectrum reveals that the remaining spin is the neutral complex. A higher spin integration is observed for  $\text{R} = \text{H}$  (~18 %), and again close inspection of the oxidized spectrum reveals that the signal is due to the neutral  $\text{Cr}(\text{V})$  complex. When  $\text{R} = \text{OMe}$ , an even higher double spin integration is calculated at ~27 %. Finally, the spin integration drops to ~15% with the  $\text{R} = \text{O}^i\text{Pr}$  derivative. The residual signal observed can be attributed to unreacted  $\text{Cr}^{\text{V}}\text{NSal}^{\text{R}}$ , as well as potential decay that occurs during EPR sample preparation. Unexpectedly,  $\text{CrNSal}^{\text{NEt}_2}$  retains significant signal and spin integration, as well as the same line shape as the neutral  $\text{Cr}(\text{V})$  species. While this could be attributed to incomplete oxidation, the same spectrum was collected after performing a replicate, suggesting the spectrum is accurate. The previously reported spectrum for  $[\text{CrNSal}^{\text{NMe}_2}]^{+\bullet}$  showed different symmetry upon oxidation and could be attributed to the presence of neutral and bis-oxidized species that form upon comproportionation.<sup>108</sup>

EPR alone cannot definitively assign the structure for chemically oxidized  $\text{CrNSal}^{\text{NO}_2}$ ,  $\text{CrNSal}^{\text{H}}$ ,  $\text{CrNSal}^{\text{OMe}}$  and  $\text{CrNSal}^{\text{O}^i\text{Pr}}$  as  $\text{Cr}(\text{VI})$  species, and oxidized  $\text{CrNSal}^{\text{NEt}_2}$  as a  $\text{Cr}(\text{V})$  ligand radical complex due to the reasons mentioned at the beginning of this section. The relatively high double integration ratio for  $\text{CrNSal}^{\text{OMe}}$  could be attributed to unreacted  $\text{Cr}(\text{V})$  nitride and the high degree of error in calculating double spin integration. Given that chemical oxidation of  $\text{CrNSal}^{\text{NEt}_2}$  consistently yields a spectrum with high

double spin integration, controlled potential electrolysis (CPE) could serve as a milder and more controlled method of oxidation to further study this species.

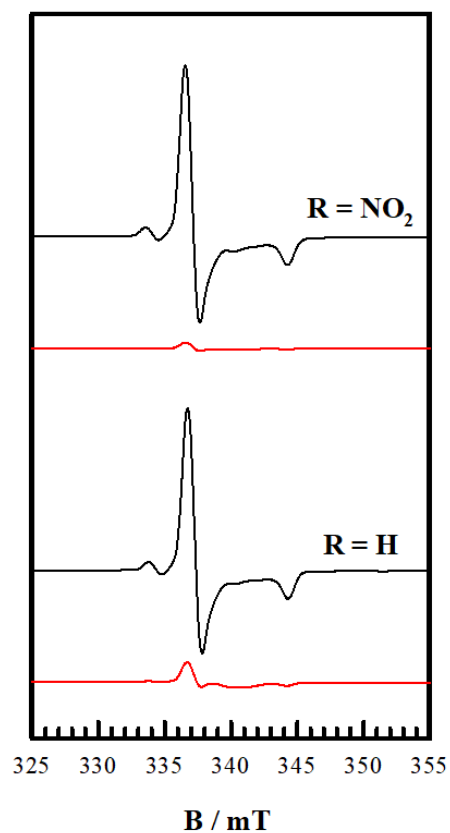


**Figure 3.9.** Frozen solution EPR spectra for concentration matched CrNSal<sup>R</sup> (black = experiment, red = oxidized). Conditions: T = 77 K; 0.45 mM complex; 0.1 M TBAP. See Table 3.4 for full instrumentation details.

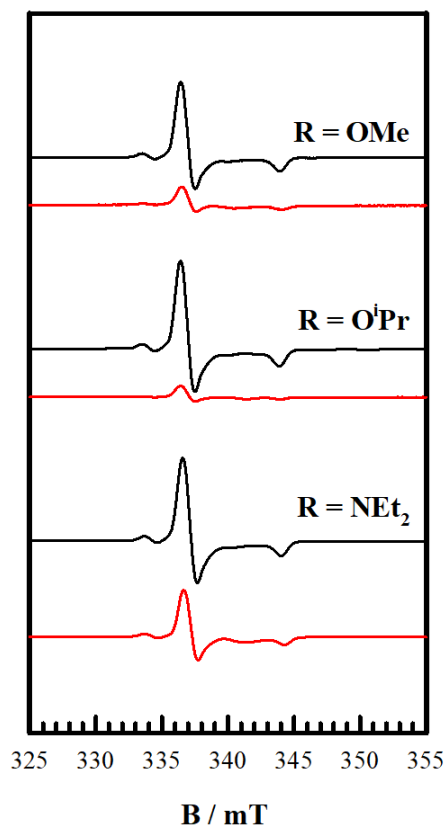


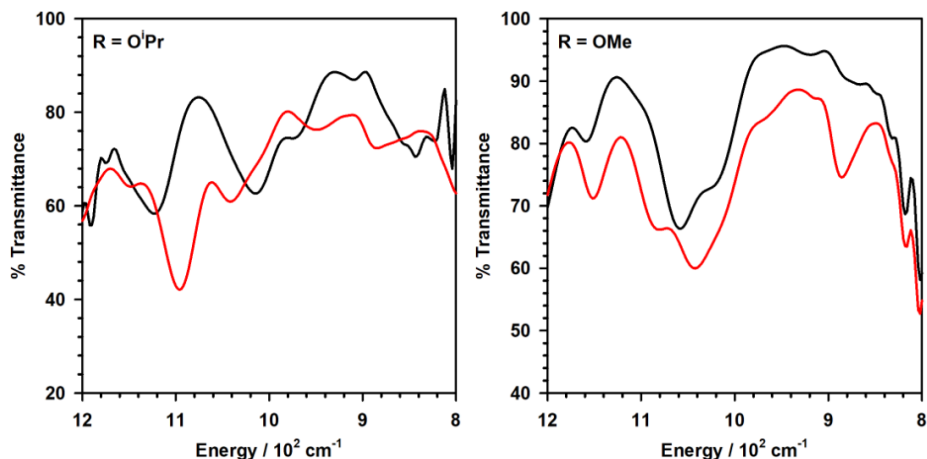
Figure 3.10. Frozen solution EPR spectra for concentration matched CrNSalR (black = experiment, red = oxidized). Conditions: T = 77 K; 0.45 mM complex; 0.1 M TBAP. See Table 3.4 for full instrumentation details.

Table 3.4. Full instrumentation details for EPR analysis of [CrNSal<sup>R</sup>]<sup>+</sup> (R = NO<sub>2</sub>, H, OMe, O<sup>i</sup>Pr, NEt<sub>2</sub>).

Complex	Freq. (MHz)	Power (mW)	Mod. Freq. (kHz)	Mod. Amp. (GHz)
CrNSal <sup>NO<sub>2</sub></sup>	9.394	2.000	100	3.0
CrNSal <sup>H</sup>	9.395	2.000	100	3.0
CrNSal <sup>OMe</sup>	9.390	2.000	100	1.0
CrNSal <sup>O<sup>i</sup>Pr</sup>	9.388	2.000	100	6.0
CrNSal <sup>NEt<sub>2</sub></sup>	9.396	2.000	100	3.0

### 3.2.4. Solution Infrared Spectroscopy

Solution IR can be used to detect changes in Cr≡N bond strength. The Cr≡N stretching frequency for Cr<sup>V</sup>NSal<sup>t</sup>Bu occurs at 1,020 cm<sup>-1</sup> in solution, and at 1,110 cm<sup>-1</sup> for [Cr<sup>VI</sup>NSal<sup>t</sup>Bu]<sup>+</sup>.<sup>108</sup> The Cr≡N stretch for Cr<sup>V</sup>NSal<sup>CF3</sup> is observed at 1,029 cm<sup>-1</sup>, however the stretch for [CrNSal<sup>CF3</sup>]<sup>+</sup> is obscured by adjacent bands.<sup>108</sup> In comparison to the high-valent Cr(VI) complexes, the Cr≡N stretch for Cr<sup>V</sup>NSal<sup>NMe2</sup> only changes from 1,020 cm<sup>-1</sup> to 1,021 cm<sup>-1</sup> after oxidation to the ligand radical [Cr<sup>V</sup>NSal<sup>NMe2</sup>]<sup>•+</sup>.<sup>108</sup> High-valent Cr(VI) contains a stronger Cr≡N bond as predicted by theoretical methods (Section 3.2.5), and a shift to higher energy for the Cr≡N stretching frequency has been observed in the literature.<sup>108</sup> Solution IR data for CrNSal<sup>R</sup> and [CrNSal<sup>R</sup>]<sup>+</sup> (R = OMe, O<sup>i</sup>Pr) is shown in Figure 3.11. CrNSal<sup>O<sup>i</sup>Pr</sup> exhibits a resolved Cr≡N stretch at 1,014 cm<sup>-1</sup>, which is consistent with the previously measured data for the neutral CrNSal<sup>R</sup> complexes (R = CF<sub>3</sub>, <sup>t</sup>Bu, NMe<sub>2</sub>).<sup>108</sup> Upon oxidation to [CrNSal<sup>O<sup>i</sup>Pr</sup>]<sup>+</sup>, the band at 1,014 cm<sup>-1</sup> is lost and two new bands appear at 1,041 cm<sup>-1</sup> and 1,096 cm<sup>-1</sup>. While it is unclear at this time which of the two new bands corresponds to the Cr≡N stretch, it is clear that oxidation leads to a substantial increase in stretching frequency in accord with metal-based oxidation to a Cr(VI) species. The Cr≡N stretch for CrNSal<sup>OMe</sup> is harder to distinguish, but likely manifests as a shoulder around 1,020 cm<sup>-1</sup> (Figure 3.11). Upon oxidation to [CrNSal<sup>OMe</sup>]<sup>+</sup> new stretching bands at 1,041 cm<sup>-1</sup> and 1,081 cm<sup>-1</sup> are apparent which could be due to the Cr≡N stretch. While the IR for the R = OMe is not conclusive for assigning the shift in the Cr≡N stretch upon oxidation, the IR data for R = O<sup>i</sup>Pr provides strong support for the shift in the Cr≡N stretch to higher energy upon oxidation, consistent with metal-based oxidation for this derivative.



**Figure 3.11.** Solution IR spectra for neutral (black) and chemically oxidized with magic green (red)  $\text{CrNSal}^{\text{OMe}}$  and  $\text{CrNSal}^{\text{O}^i\text{Pr}}$ . Conditions: 5 mM complex;  $T = 293 \text{ K}$ ;  $\text{CH}_2\text{Cl}_2$ .

### 3.2.5. Theoretical Analysis

Three geometry optimizations were performed for each oxidized  $\text{CrNSal}^{\text{R}}$  species corresponding to singlet, broken-symmetry singlet (BSS) and triplet spin states. As described in section 3.2.3, the singlet state corresponds to  $d^0 \text{Cr(VI)}$  ( $S = 0$ ), triplet refers to ferromagnetically coupling between the  $d_{xy}$  electron of  $\text{Cr(V)}$  and a ligand radical ( $S = 1$ ), and BSS refers to the antiferromagnetically coupled  $\text{Cr(V)}$   $d_{xy}$  electron and ligand radical ( $S = 0$ ). Relative energies for each spin state are shown in Table 3.4. As expected, the electron-withdrawing and weaker electron-donating R-groups favour metal-based oxidation whereas strong electron-donating groups tend to favour ligand-based oxidation. This is in accord with our previous work on the  $\text{CF}_3$ ,  $^t\text{Bu}$  and  $\text{NMe}_2$  derivatives.<sup>108</sup> Inspection of the full series (Table 3.4), shows that energy gap between the spin states for a given complex increases with electron withdrawing strength. Despite the small energy gap determined computationally between spin states for  $[\text{CrNSal}^{\text{OMe}}]^+$  and  $[\text{CrNSal}^{\text{O}^i\text{Pr}}]^+$ , the  $\text{Cr(VI)}$  singlet is of lowest energy, and experimental evidence also points towards metal-based oxidation under the conditions tested.  $[\text{CrNSal}^{\text{NMe}_2}]^+$  and  $[\text{CrNSal}^{\text{NEt}_2}]^+$  are predicted to form  $\text{Cr(V)}$  ligand radical species, either antiferromagnetically coupled BSS or ferromagnetically coupled triplet species upon oxidation. There is very little energy gap between the BSS and triplet states for  $[\text{CrNSal}^{\text{NMe}_2}]^+$ , and no difference in energy for  $[\text{CrNSal}^{\text{NEt}_2}]^+$ .

**Table 3.5. Relative energies of different spin states for [CrNSal<sup>R</sup>]<sup>+</sup> (kcal/mol).**

Complex	Singlet	BSS	Triplet
CrNSal <sup>NO2</sup>	0	4.1	10.4
CrNSal <sup>CF3</sup>	0	4.4	9.9
CrNSal <sup>H</sup>	0	3.6	8.5
CrNSal <sup><sup>t</sup>Bu</sup>	0	2.8	6.4
CrNSal <sup>OMe</sup>	0	1.9	2.3
CrNSal <sup>O<sup>i</sup>Pr</sup>	0	0.3	2.5
CrNSal <sup>NMe2</sup>	2.3	0	0.6
CrNSal <sup>NEt2</sup>	2.4	0	0

Key coordination sphere bond lengths and their respective changes are shown in Table 3.5. In accordance with forming a high-valent metal, a contracted coordination sphere is observed for lowest energy singlet solutions for [CrNSal<sup>R</sup>]<sup>+</sup> (R = NO<sub>2</sub>, CF<sub>3</sub>, H, <sup>t</sup>Bu, OMe, O<sup>i</sup>Pr). Significant shortening of the chromium-phenolate (Cr-O) bond is observed for [CrNSal<sup>R</sup>]<sup>+</sup> (R = NO<sub>2</sub>, CF<sub>3</sub>, H, <sup>t</sup>Bu, OMe, O<sup>i</sup>Pr) compared to the neutral species, though there is little change in Cr-N bond length with different *para* substituents. Additionally, the lowest energy BSS solutions for the ligand radical species [CrNSal<sup>NMe2</sup>]<sup>+</sup> and [CrNSal<sup>NEt2</sup>]<sup>+</sup> predict an asymmetric coordination sphere due to radical localization on one of the two phenolates. For example, the Cr-O2 bond is predicted to lengthen, with a concomitant decrease in the O2-C2 bond for [CrNSal<sup>NEt2</sup>]<sup>+</sup>, which is consistent with phenoxy radical formation. In comparison the Cr-O1 bond decreases slightly, and the O1-C1 bond remains essentially unchanged. The spin density plots (Figure 3.12) show a visual representation of this ligand radical localization.



**Table 3.6. Predicted coordination sphere bond lengths (Å) for [CrNSal<sup>R</sup>]<sup>+</sup>. Changes from neutral to oxidized (oxidized – neutral) in parentheses. Refer to Table 2.4 for neutral metrics, and to Figures 2.5-2.9 for atom numbering scheme. Ligand radical metrics obtained from BSS state.**

Complex	Cr1-O1	Cr1-O2	Cr1-N1	Cr1-N2	Cr1-N3	O1-C1	O2-C2
[Cr <sup>VI</sup> NSal <sup>NO2</sup> ] <sup>+</sup>	1.815 (-0.117)	1.818 (-0.123)	2.029 (0.002)	2.063 (0.026)	1.502 (-0.017)	1.324 (0.022)	1.334 (0.031)
[Cr <sup>VI</sup> NSal <sup>CF3</sup> ] <sup>+</sup>	1.813 (-0.114)	1.818 (-0.118)	2.026 (-0.002)	2.065 (0.028)	1.503 (-0.018)	1.328 (0.019)	1.340 (0.03)
[Cr <sup>VI</sup> NSal <sup>H</sup> ] <sup>+</sup>	1.813 (-0.109)	1.816 (-0.114)	2.028 (-0.001)	2.062 (0.021)	1.505 (-0.018)	1.332 (0.017)	1.344 (0.028)
[Cr <sup>VI</sup> NSal <sup>tBu</sup> ] <sup>+</sup>	1.815 (-0.107)	1.819 (-0.111)	2.022 (-0.007)	2.062 (0.024)	1.505 (-0.019)	1.331 (0.015)	1.343 (0.027)
[Cr <sup>VI</sup> NSal <sup>OMe</sup> ] <sup>+</sup>	1.821 (-0.095)	1.824 (-0.101)	2.023 (-0.011)	2.060 (0.017)	1.506 (-0.018)	1.328 (0.008)	1.344 (0.023)
[Cr <sup>VI</sup> NSal <sup>OiPr</sup> ] <sup>+</sup>	1.825 (-0.094)	1.829 (-0.099)	2.018 (-0.012)	2.052 (0.014)	1.506 (-0.019)	1.325 (0.007)	1.339 (0.021)
[Cr <sup>V</sup> NSal <sup>NMe2</sup> ] <sup>•+</sup>	1.891 (-0.028)	1.978 (0.050)	2.009 (-0.020)	2.047 (0.009)	1.522 (-0.003)	1.324 (0.006)	1.285 (-0.032)
[Cr <sup>V</sup> NSal <sup>NEt2</sup> ] <sup>•+</sup>	1.893 (-0.021)	1.975 (0.052)	2.010 (-0.023)	2.047 (0.005)	1.523 (-0.003)	1.324 (0.001)	1.287 (-0.036)

Spin density plots were prepared for [CrNSal<sup>NEt2</sup>]<sup>•+</sup> in the BSS and triplet spin states to visualize where the unpaired electron is located on the ligand (Figure 3.12). Similar plots were obtained for [CrNSal<sup>NMe2</sup>]<sup>•+</sup> (see Appendix B - Figure B6). Both spin states show most of the spin lies on one of the phenolate rings. As expected, spin is also observed on Cr. This spin localization has been observed in other transition metal complexes utilizing NMe<sub>2</sub> substituted salen ligands.

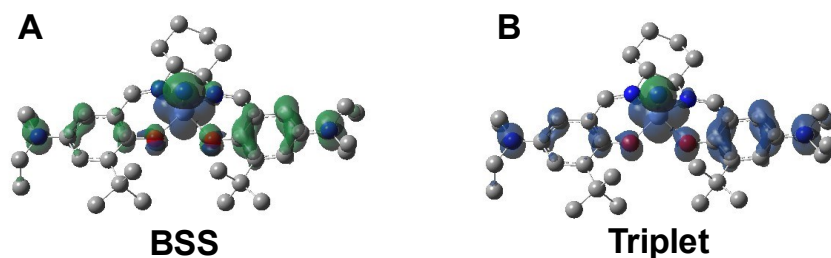


**Figure 3.12.** Spin density plots for oxidized CrNSal<sup>NEt<sub>2</sub></sup> in the BSS (A) and triplet (B) spin states.

IR spectroscopy provides further insight into the Cr≡N bond strength and locus of oxidation as described in Section 3.2.4. The predicted change in energy of the Cr≡N stretch for the lowest energy electronic structures for CrNSal<sup>R</sup> and [CrNSal<sup>R</sup>]<sup>+</sup> are tabulated in Table 3.7. Frequency calculations were performed at the same level of theory as optimizations. All high-valent metal complexes exhibit stretches at higher frequencies in comparison to their neutral analogs by ~80 cm<sup>-1</sup>. In contrast, the ligand radical species [Cr<sup>V</sup>NSal<sup>R</sup>]<sup>•+</sup> display little change in Cr≡N stretch, with a shift to higher energy by only ~8 cm<sup>-1</sup>. As discussed in Section 3.2.4, a shift to higher energy is consistent with a stronger Cr≡N bond upon oxidation. This can be attributed to a decrease in the energy of the Cr d-orbitals upon oxidation from Cr(V) to Cr(VI) resulting in improved overlap with the nitride p-orbitals (see Figure 1.4), and stronger bonding.

**Table 3.7.** Predicted change ( $\Delta$ ) in Cr≡N Stretch Frequencies (cm<sup>-1</sup>) upon oxidation of CrNSal<sup>R</sup> to [CrNSal<sup>R</sup>]<sup>+</sup>.

Complex	Change in Cr≡N Stretch (cm <sup>-1</sup> )
[Cr <sup>VI</sup> NSal <sup>NO2</sup> ] <sup>+</sup>	76
[Cr <sup>VI</sup> NSal <sup>CF3</sup> ] <sup>+</sup>	79
[Cr <sup>VI</sup> NSal <sup>H</sup> ] <sup>+</sup>	78
[Cr <sup>VI</sup> NSal <sup>tBu</sup> ] <sup>+</sup>	79
[Cr <sup>VI</sup> NSal <sup>OMe</sup> ] <sup>+</sup>	77
[Cr <sup>VI</sup> NSal <sup>OiPr</sup> ] <sup>+</sup>	79
[Cr <sup>V</sup> NSal <sup>NMe2</sup> ] <sup>•+</sup>	-8
[Cr <sup>V</sup> NSal <sup>NEt2</sup> ] <sup>•+</sup>	-7

### 3.3. Conclusion

Multiple methods are required to assess the locus of oxidation and extent of ligand radical delocalization in the system under study. Cyclic voltammograms of CrNSal<sup>NO<sub>2</sub></sup> and CrNSal<sup>H</sup> feature one reversible redox event, while CrNSal<sup>OMe</sup>, CrNSal<sup>O<sup>i</sup>Pr</sup> and CrNSal<sup>NEt<sub>2</sub></sup> feature two close redox events at relatively low potentials. Chemical oxidation of CrNSal<sup>R</sup> (R = NO<sub>2</sub>, H, OMe, O<sup>i</sup>Pr) monitored by UV-vis-NIR results in the appearance of broad low energy bands between 17,000 cm<sup>-1</sup> and 5,000 cm<sup>-1</sup>. These broad NIR bands blue shift as the  $\sigma_p$  increases, consistent with a LMCT assignment.

Oxidation of CrNSal<sup>NEt<sub>2</sub></sup>, similarly to CrNSal<sup>NMe<sub>2</sub></sup>, exhibits a different UV-vis-NIR spectrum in comparison to the derivatives above, showing a broad envelope of transitions in the 24,000 cm<sup>-1</sup> to 10,000 cm<sup>-1</sup> region, and thus supporting a different electronic structure for these two derivatives. Upon oxidation, The EPR signals for all [CrNSal<sup>R</sup>]<sup>+</sup> species are substantially diminished compared to the neutral analogues. Interestingly, the oxidized CrNSal<sup>NEt<sub>2</sub></sup> still exhibited a significant amount of spin after oxidation, and this result needs further investigation. Solution IR spectroscopy of neutral and oxidized CrNSal<sup>NEt<sub>2</sub></sup> can provide insight into the locus of oxidation, as a weaker shift in Cr≡N stretch was detected for [CrNSal<sup>NMe<sub>2</sub></sup>]<sup>•+</sup> ( $\Delta\nu = 1$  cm<sup>-1</sup>) than for [CrNSal<sup>tBu</sup>]<sup>+</sup> (90 cm<sup>-1</sup>). Finally, DFT analysis predicts high-valent Cr(VI) complexes after oxidation of CrNSal<sup>R</sup> (R = NO<sub>2</sub>, H, OMe, O<sup>i</sup>Pr) and the BSS ligand radical structure for CrNSal<sup>NEt<sub>2</sub></sup>.

The current data supports metal-based oxidation to Cr(VI) for CrNSal<sup>R</sup> (R = NO<sub>2</sub>, H, OMe, O<sup>i</sup>Pr), and ligand oxidation for CrNSal<sup>NEt<sub>2</sub></sup>. However, additional studies could be used to definitively assign the locus oxidation for [CrNSal<sup>R</sup>]<sup>+</sup>. For example, Evan's method <sup>1</sup>H NMR could be used in this system. Cr<sup>V</sup>NSal<sup>R</sup> is paramagnetic and exhibits broad signals. If metal oxidation occurs, [Cr<sup>VI</sup>NSal<sup>R</sup>]<sup>+</sup> becomes diamagnetic and a spectrum with resolved signals can be obtained, while triplet and BSS species spectra can remain broadened. X-ray absorption (XAS) can also provide insight into the oxidation state of Cr for [CrNSal<sup>R</sup>]<sup>+</sup>. Finally, the reactivity of [CrNSal<sup>R</sup>]<sup>+</sup> towards electrophilic boranes and nucleophilic phosphines can indicate the oxidation state of Cr. As discussed in Section 1.5, [Cr<sup>VI</sup>NSal<sup>R</sup>]<sup>+</sup> (R = CF<sub>3</sub>, <sup>t</sup>Bu) contain electrophilic nitrides and react with phosphines, in contrast to [Cr<sup>V</sup>NSal<sup>NMe<sub>2</sub></sup>]<sup>•+</sup> which has a nucleophilic nitride and reacts with boranes.

## 3.4. Experimental

### 3.4.1. Materials

All chemicals used were obtained from commercial suppliers and used without any further purification unless noted otherwise.  $[(2,4\text{-Br}_2\text{C}_6\text{H}_3)_3\text{N}^+][\text{SbF}_6]^-$  (magic green oxidant) was synthesized according to literature methods.<sup>162</sup> Dry dichloromethane was obtained by refluxing over calcium hydride under  $\text{N}_2$ .

### 3.4.2. Instrumentation

See Section 2.4.2 for full instrumentation details. Electrochemistry experiments were performed on PAR-263A potentiometer equipped with a silver wire reference electrode, a platinum disk counter electrode and glassy carbon working electrode under  $\text{N}_2$  atmosphere. Solution IR spectra were collected on a PerkinElmer UTAR Two FT-IR spectrometer using a 1 mm Specac transmission cell.

### 3.4.3. Synthesis of $[\text{CrNSal}^{\text{R}}]^+$

Oxidation titrations were performed by titration of 3.5 mL of 0.45 mM  $\text{CrNSal}^{\text{R}}$  with one equivalent of magic green oxidant in 20  $\mu\text{L}$  additions at 253 K under a  $\text{N}_2$  atmosphere. A solution of magic green was first standardized by titration with 3.5 mL of 0.45 mM  $\text{NiSal}^{\text{tBu}}$ , in which oxidant was slowly added until no further increase or a decrease in absorbance of the  $4,700\text{ cm}^{-1}$  band was observed. Excess oxidant will also manifest as a strong absorbance at  $11,260\text{ cm}^{-1}$ .<sup>107,162</sup> Frozen samples for EPR analysis were prepared as above in the presence of 0.1 M TBAP supporting electrolyte and stored in liquid  $\text{N}_2$  for analysis.

### 3.4.4. Theoretical Analysis

All theoretical analyses were performed using Gaussian 16 (version C.01) software using Compute Canada cluster resources. All analyses used the polarizable continuum model (PCM) with DCM ( $\epsilon = 8.93$ ) as the solvent. Optimizations and frequency calculations

were performed using the B3LYP functional and 6-31g\* basis set. Single point energies and NBO calculations were determined using the UBLYP functional and TZVP basis set.

# Chapter 4. Reactivity of $[\text{CrNSal}^{\text{R}}]^+$ ( $\text{R} = \text{tBu}, \text{NMe}_2$ ) Towards Exogenous Ligands and C-H Bond Activation

## 4.1. Introduction

$\text{Cr}^{\text{V}}$  salen oxo complexes are effective epoxidation reagents as discussed previously in Chapter 1. However, these compounds require binding of an axial ligand *trans* to the oxo to achieve their full reactivity potential.<sup>116</sup> Computational studies with Mn oxo salen complexes found that the Mn-O bond is weakened after exogenous ligand binding and triggers geometric changes in the coordination sphere.<sup>116</sup> Similar to Cr salen oxo complexes,  $\text{Ru}^{\text{VI}}$  salen nitride complexes are stable in weakly coordinating solvents, but undergo homocoupling in the presence of stronger neutral and anionic ligands as discovered by Man *et al.*<sup>170</sup>

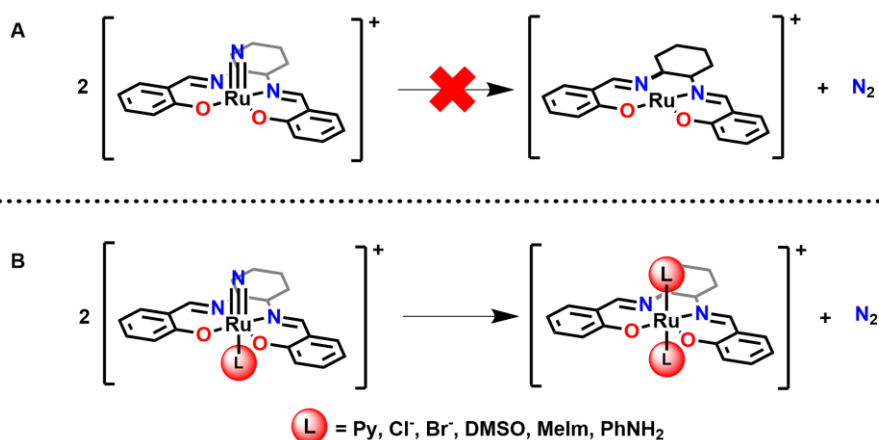


**Figure 4.1.**  $[\text{Ru}^{\text{VI}}\text{NSal}^{\text{H}}]^+$  is stable in the absence of an exogenous ligand (A).<sup>170</sup> Axial binding of an exogenous ligand activates the nitride towards homocoupling (B).

Man *et al.* also found that  $\text{Ru}^{\text{VI}}$  salen nitride complexes can activate weaker C-H bonds such as those in xanthene in acetonitrile to form N-insertion products, but can also activate significantly stronger C-H bonds such as those in cyclohexane when ligands such as pyridine, bromide, or chloride are present as shown in Figure 4.2.<sup>68</sup> In addition to exogenous ligands, the R-group substituent on the salen ligand was shown to significantly affect the reactivity of Cr oxo salen complexes towards oxygen transfer.<sup>119,171–173</sup>

Therefore, oxidized Cr<sup>VI</sup> salen nitrides could prove to be effective N atom transfer reagents as well.

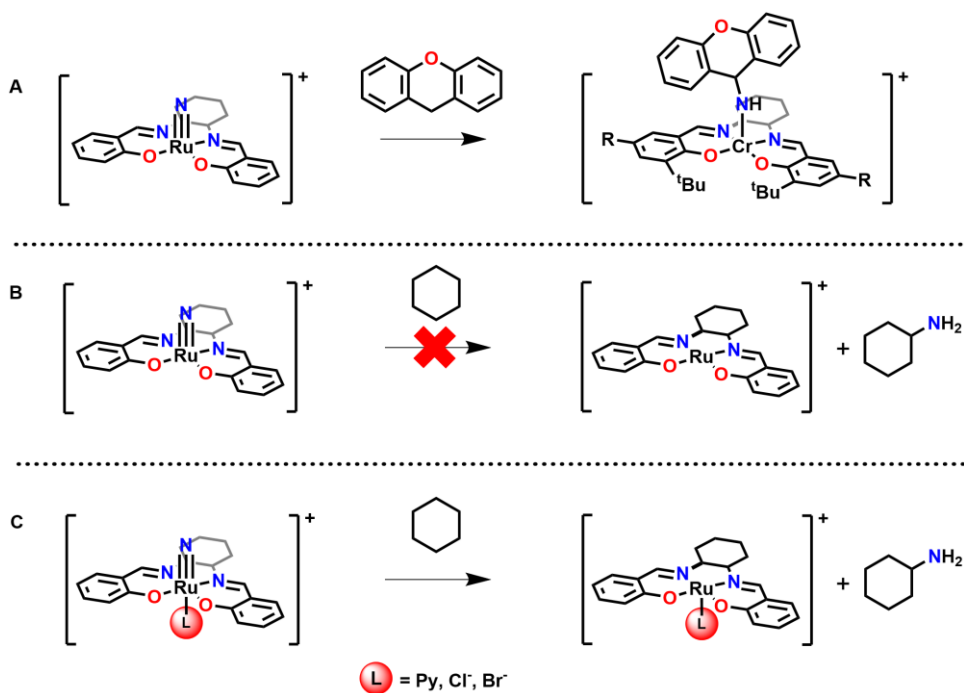


**Figure 4.2.** Man's Ru<sup>VI</sup> nitride complex that performs C-H bond activation (A).<sup>68</sup> In the absence of exogenous ligands, the complex cannot activate strong C-H bonds such as those in cyclohexane (B) until exogenous ligands bind to vacant axial site (C).

This chapter will examine how neutral and anionic ligands interact with [CrNSal<sup>R</sup>]<sup>+</sup> and the decay pathway that occurs, as well as the reactivity of [CrNSal<sup>R</sup>]<sup>+</sup> towards C-H bond activation. Previous research in the Storr group found that [CrNSal<sup>R</sup>]<sup>+</sup> are relatively stable at room temperature and slowly decay according to second-order kinetics.<sup>108</sup> [Mn<sup>VI</sup>NSal<sup>R</sup>]<sup>+</sup> complexes are unstable at room temperature and also decay according to second-order kinetics to liberate N<sub>2</sub> gas.<sup>106</sup> Based on the interaction of Cr oxo complexes and [Ru<sup>VI</sup>NSal<sup>H</sup>]<sup>+</sup> with exogenous ligands, the binding of axial ligands *trans* to the nitride ligand in [CrNSal<sup>R</sup>]<sup>+</sup> should lead to activation and homocoupling (Figure 4.3). [CrNSal<sup>R</sup>]<sup>+</sup> may also react with the weak C-H bond activation substrate xanthene to form an N-insertion product.

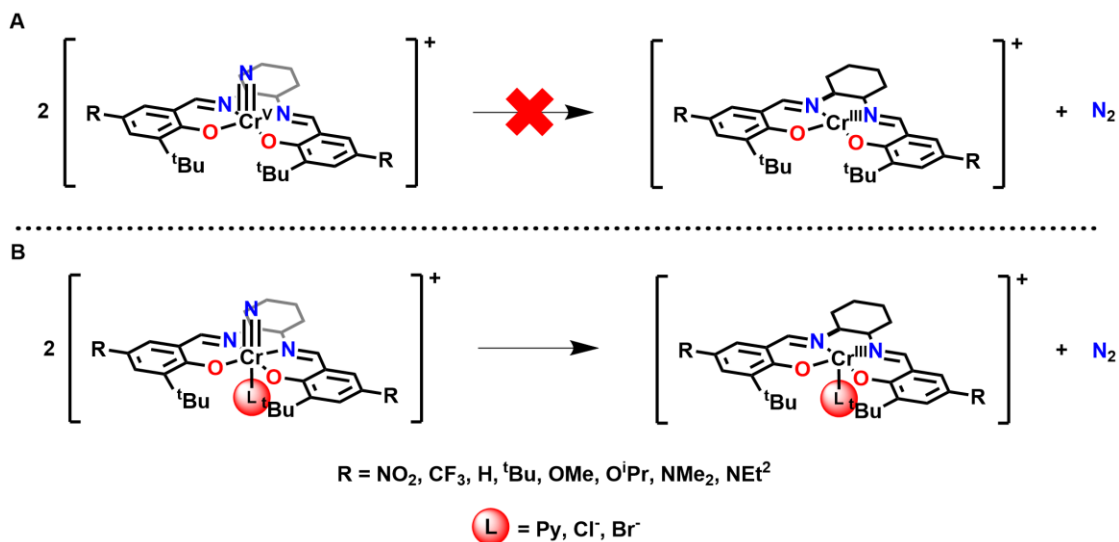


Figure 4.3. [CrNSal<sup>R</sup>]<sup>+</sup> is relatively stable towards homocoupling at room temperature (A). Exogenous ligands should bind *trans* to the nitride and activate it towards homocoupling (B).

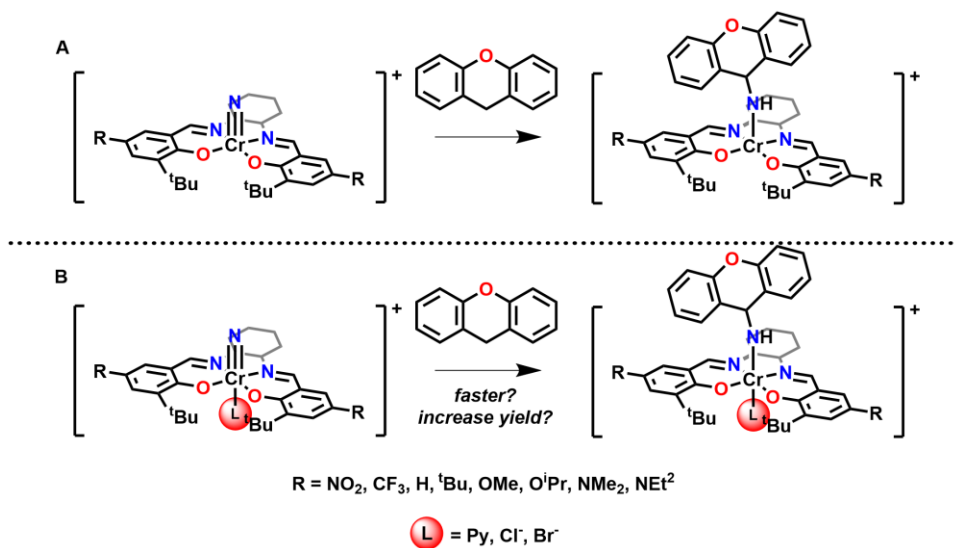


Figure 4.4. [CrNSal<sup>R</sup>]<sup>+</sup> may activate the weak C-H bonds in xanthene and form an N-insertion product (A). The addition of exogenous ligands should activate the nitride and increase reactivity (B).



## 4.2. Results

### 4.2.1. Electronic Absorption Spectroscopy with Ligands

UV-vis-NIR spectroscopy was used to monitor changes as one equivalent of pyridine, bromide and chloride ligands were added to solutions of  $[\text{CrNSal}^{\text{tBu}}]^+$  and  $[\text{CrNSal}^{\text{NMe}_2}]^{*+}$ . Spectral changes are observed when aliquots of each ligand are added to  $[\text{CrNSal}^{\text{tBu}}]^+$  with a decrease in the bands at  $21,800 \text{ cm}^{-1}$  and  $8,100 \text{ cm}^{-1}$  (Figure 4.5). The most significant decrease in the band intensities was observed with the addition of chloride. Addition of a second equivalent of ligand results in full decay of the  $8,100 \text{ cm}^{-1}$  band (Appendix C - Figure C1). We then investigated the change in the  $[\text{CrNSal}^{\text{tBu}}]^+$  spectrum over time after addition of one equivalent of the exogenous ligands (Figure 4.6). In this case immediate changes are observed for both chloride and bromide addition, while a slower change is observed for pyridine. While preliminary, these results suggest that a more significant interaction is observed for the anionic chloride and bromide ligands in comparison to pyridine. Very limited spectral changes are observed when one equivalent of either chloride, bromide, or pyridine are added to  $[\text{CrNSal}^{\text{NMe}_2}]^{*+}$  (Figure 4.7). This indicates that the locus of oxidation and/or donation strength of the salen ligand strongly influences the reaction of exogenous ligands with oxidized chromium salen nitrides. Given that the locus of oxidation is metal-based for  $[\text{CrNSal}^{\text{tBu}}]^+$ , this is in agreement with the metal center being more Lewis acidic.

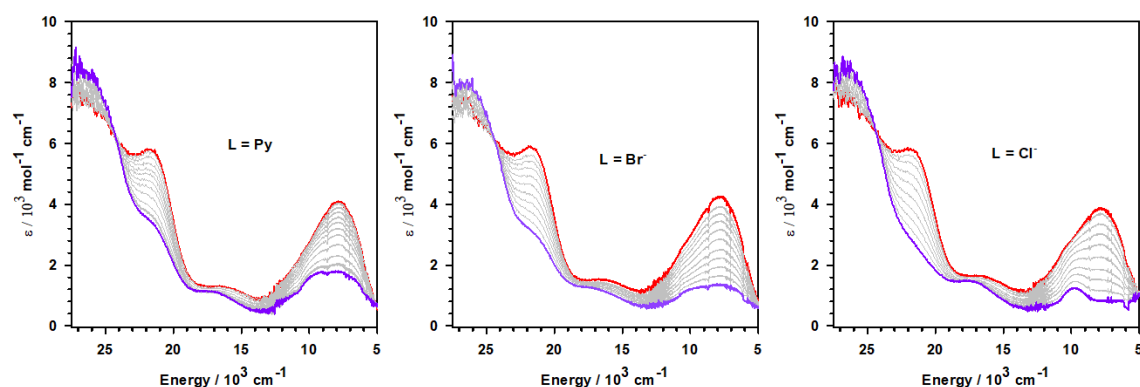


**Figure 4.5.** Titration of one equivalent of pyridine, bromide, and chloride into  $[\text{CrNSal}^{\text{tBu}}]^+$  monitored by UV-vis-NIR spectroscopy. Conditions:  $0.1 \text{ mM } [\text{CrNSal}^{\text{R}}]^+$ ;  $T = 253 \text{ K}$ ;  $\text{CH}_2\text{Cl}_2$ . Red =  $[\text{CrNSal}^{\text{tBu}}]^+$ ; grey = intermediate aliquots of ligand; purple = one equivalent of ligand.

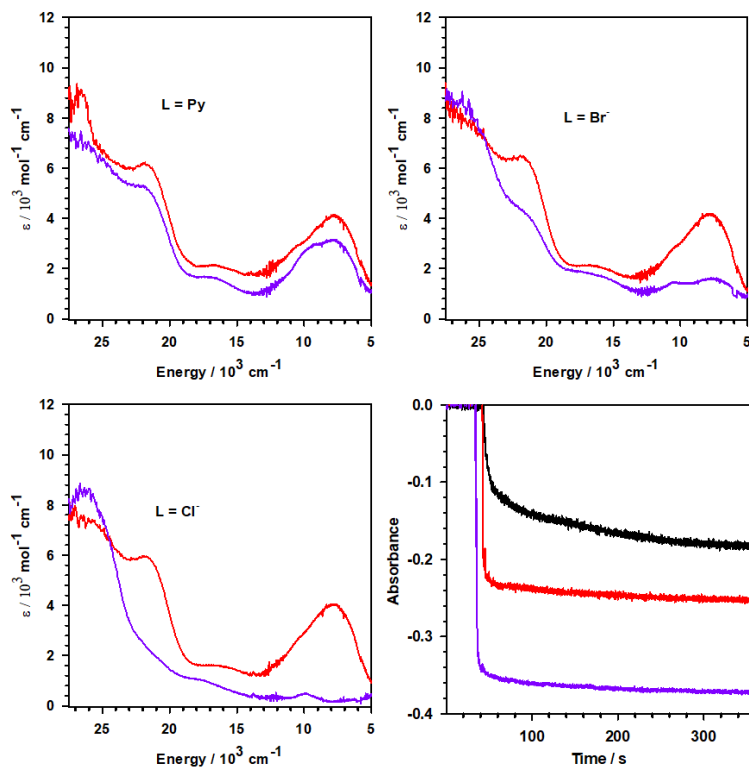


**Figure 4.6.** UV-vis-NIR spectra for  $[\text{CrNSal}^{\text{tBu}}]^+$  after 3 minutes of reaction with 1 equivalent of pyridine, bromide and chloride. Conditions: 0.1 mM  $[\text{CrNSal}^{\text{tBu}}]^+$ ;  $T = 253 \text{ K}$ ;  $\text{CH}_2\text{Cl}_2$ . Red =  $[\text{CrNSal}^{\text{tBu}}]^+$ ; purple = one equivalent of ligand. Decay of the 8,100  $\text{cm}^{-1}$  NIR band was also monitored over time for each ligand (bottom right).

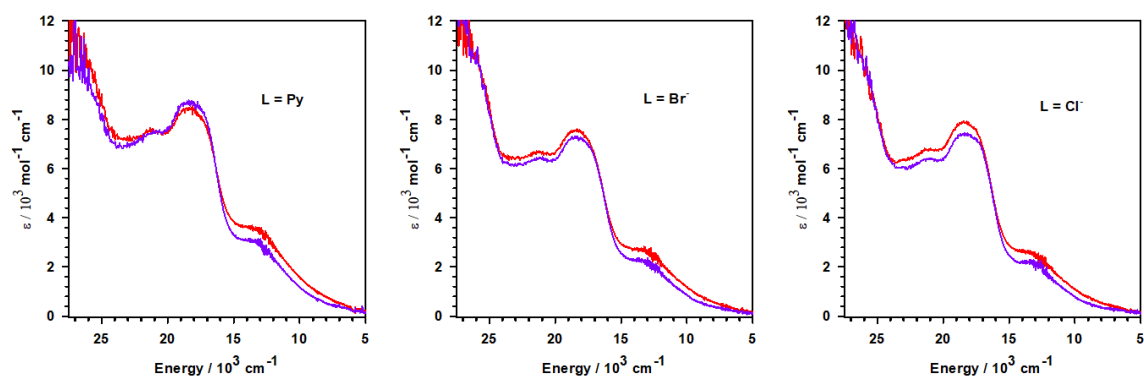


**Figure 4.7.** UV-vis-NIR spectra for  $[\text{CrNSal}^{\text{NMe}_2}]^+$  after 1 hour reaction with 1 equivalent of pyridine, bromide and chloride. Conditions: 0.1 mM  $[\text{CrNSal}^{\text{NMe}_2}]^+$ ;  $T = 253 \text{ K}$ ;  $\text{CH}_2\text{Cl}_2$ . Red =  $[\text{CrNSal}^{\text{tBu}}]^+$ ; purple = one equivalent of ligand.

ESI-MS analysis of the reaction between  $[\text{CrNSal}^{\text{tBu}}]^+$  and exogenous ligands should identify the  $[\text{Cr}^{\text{III}}\text{Lsal}]^+$  product if homocoupling is occurring. Figure 4.8 shows the mass spectrum following addition of pyridine to  $[\text{CrNSal}^{\text{tBu}}]^+$  and key compounds observed. Multiple  $[\text{Cr}^{\text{III}}\text{Sal}^{\text{tBu}}]^+$  species are observed, corresponding to two, one or no pyridine ligands bound. These  $\text{Cr}^{\text{III}}$  cations are consistent with a homocoupling decay pathway, however decay caused by ESI-MS conditions cannot be ruled out. Residual  $[\text{CrNSal}^{\text{tBu}}+\text{H}]^+$  could be due to incomplete oxidation of the starting complex as well as incomplete reaction with pyridine. Attempts to identify the products of the reaction between  $[\text{CrNSal}^{\text{tBu}}]^+$  and  $\text{Cl}^-$  using positive mode ESI-MS were unsuccessful due to the strong tetraethylammonium cation signal (Appendix C – Figure C2).

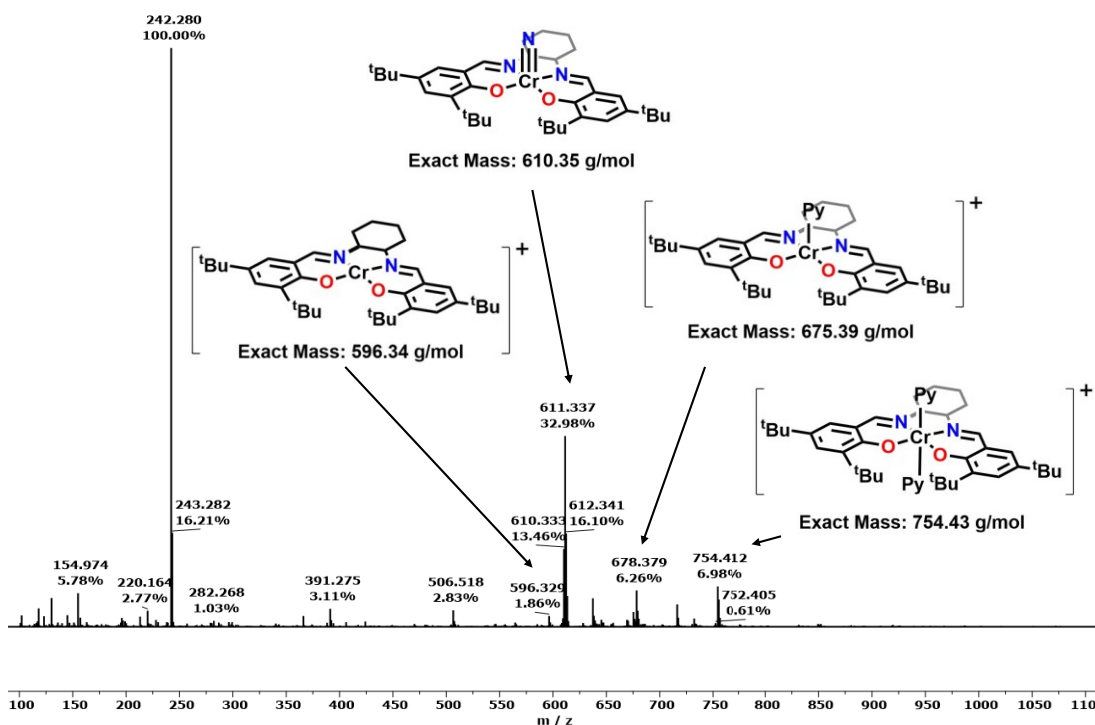


**Figure 4.8.** ESI-MS spectrum of the reaction between  $[\text{CrNSal}^{\text{tBu}}]^+$  and one equivalent of pyridine.  $\text{Cr}^{\text{V}}\text{NSal}^{\text{tBu}}$  starting material and various  $[\text{Cr}^{\text{III}}\text{Sal}]^+$  homocoupling decay products are observed.

#### 4.2.2. GC-MS Headspace Analysis

If homocoupling is occurring, a sample of 50%  $^{15}\text{N}$  labelled  $[\text{Cr}^{15}\text{NSal}^{\text{tBu}}]^+$  will liberate isotopically labelled  $^{29}\text{N}_2$  and  $^{30}\text{N}_2$  in a 2:1 ratio upon addition of exogenous ligand. However, no labelled nitrogen gas was detected via GC-MS headspace analysis after reaction with chloride or pyridine as shown in Figure 4.9. Furthermore, an oxidized sample without exogenous ligand did not generate any labelled nitrogen gas after 48 hours. Irradiation of the oxidized complex with UV light does not trigger homocoupling either, which was observed in an unpublished Storr group study. This is in stark contrast to  $[\text{Mn}^{15}\text{NSal}^{\text{tBu}}]^+$  which rapidly homocouples at room temperature (Figure 4.9). Based on the data collected so far, the oxidized nitride complexes are decaying according to second order kinetics, but homocoupling cannot be confirmed.<sup>108</sup> If homocoupling is occurring, it must be a slow process and the labelled nitrogen gas is escaping at the same rate as formation. The oxidized nitride complexes may be forming dimers, which would follow similar second-order kinetics but could trap the nitride ligands in the dimer. Unfortunately, no isotopically labelled dimer was observed after positive mode ESI-MS analysis of the pyridine reaction GC-MS experiment. The addition of ligands may activate the nitride sufficiently to dimerize, but the resulting dimer is relatively stable and does not appear to decompose to afford  $\text{N}_2$ . Further investigation is needed.

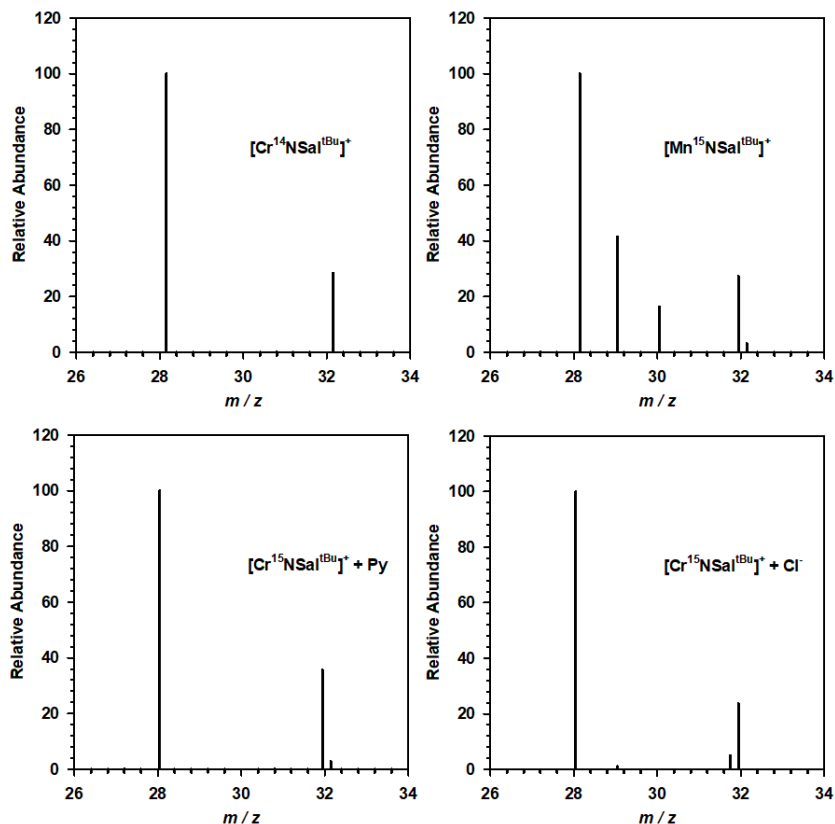


**Figure 4.9** GC-MS hepspace analysis of a  $\text{Cr}^{14}\text{NSal}^{\text{tBu}}$  blank and oxidized  $\text{Mn}^{15}\text{NSal}^{\text{tBu}}$  reference.  $\text{Cr}^{15}\text{NSal}^{\text{tBu}}$  was oxidized with magic green and 100 equivalents of pyridine or 10 equivalents of tetraethylammonium chloride were added.

### 4.2.3. Theoretical Analysis with Exogenous Ligands

Theoretical calculations should reveal any changes in coordination sphere geometry upon binding of an axial ligand to oxidized  $[\text{CrNSal}^{\text{tBu}}]^+$ . Optimizations of  $[\text{CrNSal}^{\text{tBu}}]^+$  with axial ligands were carried out with the UB3LYP functional and 6-31g\* basis set employing the polarizable continuum model (PCM) with DCM as solvent. A frequency job at the same level of theory verified the structure was at the true energetic minimum. For all ligand adducts, an interaction is observed, and key structural information is collected in Tables 4.1 and 4.2. No interaction is predicted between  $[\text{CrNSal}^{\text{NMe}_2}]^{2+}$  and  $\text{Cl}^-$ , consistent with experimental observations (Appendix C - Figure C3). Minor changes were observed for all bonds in the coordination sphere, but elongation of the  $\text{Cr}\equiv\text{N}$  bond was observed for all ligand adducts and is indicative of  $\text{Cr}\equiv\text{N}$  bond weakening. Moreover, all adducts become  $\sim 10\%$  more planar based on the  $\tau_5$  values calculated for the Cr-salen

plane.<sup>174,175</sup> This planarization of Cr and the salen ligand can activate the nitride by reducing the reorganization energy to form products.<sup>40</sup>

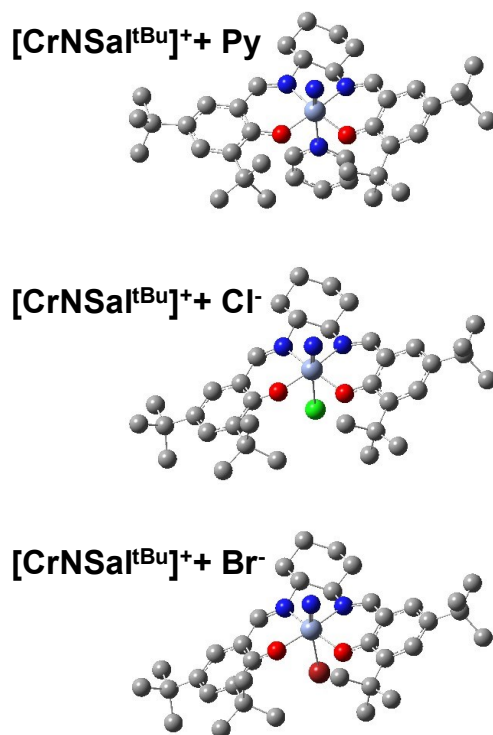


Figure 4.10. Optimized structures for adducts between  $[\text{CrNSal}^{\text{tBu}}]^+$  and pyridine, bromide and chloride.

Table 4.1. Predicted coordination sphere bond lengths (Å) for  $[\text{CrNSal}^{\text{tBu}}]^+$  and ligand adducts. Changes from  $[\text{CrNSal}^{\text{tBu}}]^+$  on ligand coordination (adduct – free complex) in parentheses.

Complex	Cr1-O1	Cr1-O2	Cr1-N1	Cr1-N2	Cr1-N3	O1-C1	O2-C2
$[\text{Cr}^{\text{VI}}\text{NSal}^{\text{tBu}}]^+$	1.819	1.815	2.022	2.062	1.505	1.331	1.343
	-	-	-	-	-	-	-
$[\text{Cr}^{\text{VI}}\text{NSal}^{\text{tBu}}]^+\text{-Py}$	1.802 (-0.017)	1.814 (-0.001)	2.090 (0.0680)	2.044 (-0.017)	1.512 (0.006)	1.335 (0.005)	1.340 (-0.003)
$\text{Cr}^{\text{VI}}\text{NSal}^{\text{tBu}}\text{-Cl}$	1.822 (0.003)	1.827 (0.013)	2.054 (0.033)	2.050 (-0.011)	1.514 (0.009)	1.328 (-0.002)	1.333 (-0.010)
$\text{Cr}^{\text{VI}}\text{NSal}^{\text{tBu}}\text{-Br}$	1.823 (0.004)	1.833 (0.018)	2.058 (0.036)	2.055 (-0.007)	1.517 (0.012)	1.329 (-0.001)	1.332 (-0.011)

**Table 4.2. Additional geometric information for [CrNSal<sup>tBu</sup>]<sup>+</sup>-L coordination sphere.**

Cr <sup>VI</sup> NSal <sup>tBu</sup> -L	No L	L = Py	L = Cl <sup>-</sup>	L = Br <sup>-</sup>
Cr≡N Bond Length (Å)	1.505	1.512	1.514	1.517
Cr-L Bond Length (Å)	-	2.72	2.916	2.936
τ <sub>5</sub> Parameter	0.18	0.04	0.09	0.08

Various Cr≡N bonding parameters can be evaluated to quantify bond strength as summarized in Table 4.3. There is a small increase in Cr≡N bond length by ~0.01Å after any of the ligands bind, consistent with a weakening of the Cr≡N bond. The Mulliken charge on the nitride also increase after ligand binding, showing an increase in nitride electrophilic character which has been reported to afford more rapid nitride homocoupling.<sup>106,108,176</sup> The %N in the Cr≡N π\* orbital suggests the oxidized complex with an axial ligand contains a more reactive nitride, although the trend is not consistent with experimental reaction rates. The Mayer bond order indicates a slightly weaker Cr≡N bond for bromide and chloride adducts, although pyridine appears to increase Cr≡N bond strength. From this data, there is an overall trend for nitride activation upon *trans* ligation.

**Table 4.3. Cr≡N Bonding Metrics for [CrNSal<sup>tBu</sup>]<sup>+</sup>-L.**

Cr <sup>VI</sup> NSal <sup>tBu</sup> -L	No L	L = Py	L = Cl <sup>-</sup>	L = Br <sup>-</sup>
Cr≡N Bond Length (Å)	1.505	1.512	1.514	1.517
Mulliken Nitride Charge	0.15	0.18	0.23	0.23
%N in Cr≡N π*	52.62	53.94	52.78	55.43
Mayer Bond Order	2.93	2.95	2.91	2.89

Further to the bonding analysis above, comparison of the energies between the different adducts can provide insight into the thermodynamics of the reaction. The energy change for adduct formation was determined by subtraction of the combined energy of the free ligand and singlet [CrNSal<sup>tBu</sup>]<sup>+</sup> from the respective adduct according to Figure 4.11.

Formation of the chloride adduct was found to be the most energetically favourable by ~8 kcal/mol and 6 kcal/mol versus the pyridine and bromide adducts respectively as shown in Table 4.4. The unfavorability of pyridine binding could be attributed to sterics and the neutral charge versus the smaller anionic ligands. This energy decrease could account for the more complete decay of the NIR band for  $[\text{CrNSal}^{\text{tBu}}]^+$  after one equivalent of chloride and bromide ligands versus pyridine. Chloride is predicted to bind more strongly, and the equilibrium strongly favors the adduct, whereas the weaker binding ligands form an equilibrium mixture of bound and unbound oxidized chromium complex. Titration of an additional equivalent of ligand into  $[\text{CrNSal}^{\text{tBu}}]^+$  supports this hypothesis, as the chloride spectrum changes less after one equivalent in comparison to pyridine and bromide (Appendix C - Figure C1).

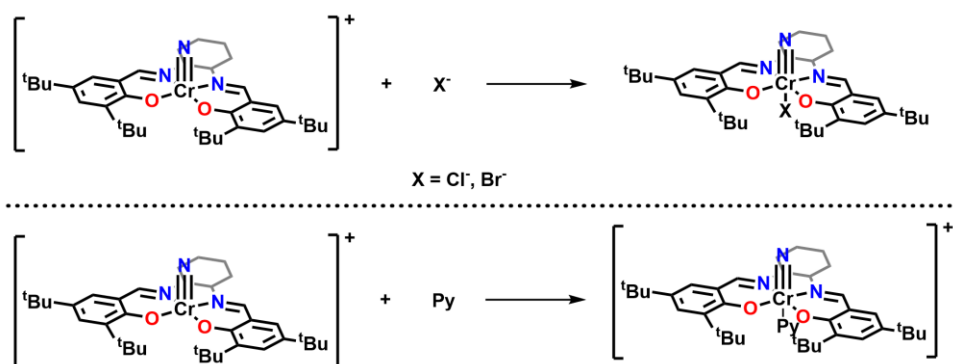


**Figure 4.11.** Reaction between oxidized  $\text{CrNSal}^{\text{tBu}}$  and exogenous ligands to form adducts.

**Table 4.4.** Reaction energetics for the interaction between oxidized  $\text{CrNSal}^{\text{tBu}}$  and pyridine, chloride and bromide ligands.

$[\text{CrNSal}^{\text{tBu}}]^+ + \text{L}$	L = Py	L = Cl <sup>-</sup>	L = Br <sup>-</sup>
$\Delta E_{\text{reaction}} / \text{kcal mol}^{-1}$	2.6	-6.7	-1.1

#### 4.2.4. Electronic Absorption Spectroscopy with Xanthene

To complement the reactivity studies of  $[\text{CrNSal}^{\text{R}}]^+$  with exogenous ligands and previous work with boranes and phosphines, C-H bond activation reactivity was also probed. UV-vis-NIR was used to monitor changes in absorbance over time after the addition of 100 equivalents of xanthene, a substrate with relatively weak C-H bonds (75.2



kcal/mol).<sup>177</sup> A reaction occurs and isosbestic points are observed for all  $[\text{CrNSal}^{\text{R}}]^+$  derivatives, indicating clean conversion to new species (Figure 4.12). The reaction occurs fastest as the electron withdrawing strength of the R-group increases, suggesting the nitride ligand is acting as an electrophile.

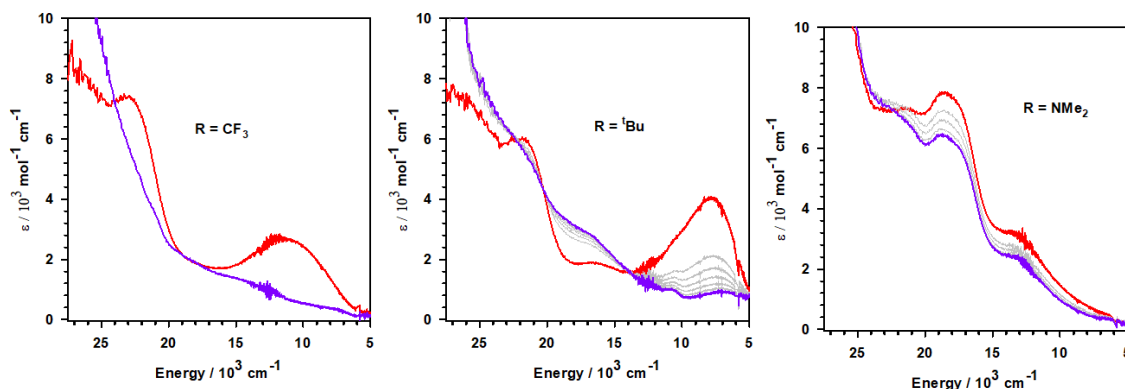


**Figure 4.12.** UV-vis-NIR spectra for the reaction between  $[\text{CrNSal}^{\text{R}}]^+$  and xanthene. Conditions: 0.1 mM  $[\text{CrNSal}^{\text{R}}]^+$ ; 10 mM xanthene; T = 253 K;  $\text{CH}_2\text{Cl}_2$ . Red =  $[\text{CrNSal}^{\text{R}}]^+$ ; grey = intermediate scans over time; purple = 2 hours after addition of xanthene.

#### 4.2.5. Mass Spectrometry of Reaction Between $[\text{CrNSal}^{\text{R}}]^+$ and Xanthene

Isosbestic points observed after reaction of  $[\text{CrNSal}^{\text{R}}]^+$  and xanthene indicate that  $[\text{CrNSal}^{\text{R}}]^+$  is cleanly converting to a new species. ESI-MS was employed to identify the potential N-insertion product(s) of this reaction, and should readily detect amines and imines that could form based on previous work.<sup>68</sup> All  $[\text{CrNSal}^{\text{R}}]^+$  tested (R =  $\text{CF}_3$ ,  $^t\text{Bu}$ ,  $\text{NMe}_2$ ) show a signal at 196.07 m/z corresponding to a free imine N-insertion product, and  $[\text{CrSal}^{^t\text{Bu}}]^+$  and  $[\text{CrSal}^{\text{CF}_3}]^+$  contain weak signals resulting from an N-insertion product bound to  $[\text{CrNSal}^{^t\text{Bu}}]^+$  at 792.409 m/z and 816.251 m/z respectively (Figures 4.13-4.15). No N-insertion adduct between xanthene and  $[\text{CrNSal}^{\text{NMe}_2}]^{++}$  was observed.

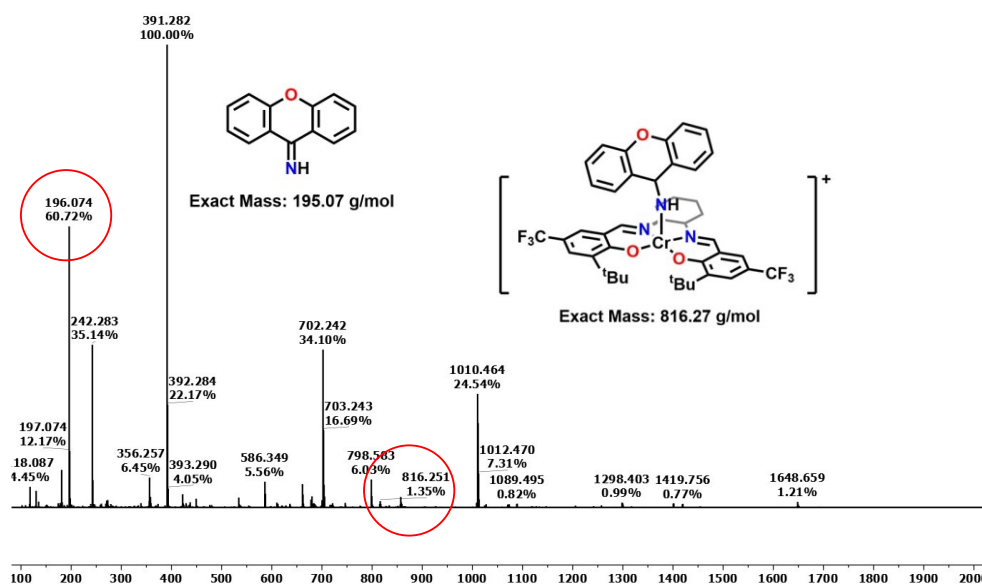


Figure 4.13. Positive-mode ESI-MS spectrum of reaction between  $[\text{CrNSal}^{\text{CF}_3}]^+$  and xanthene.

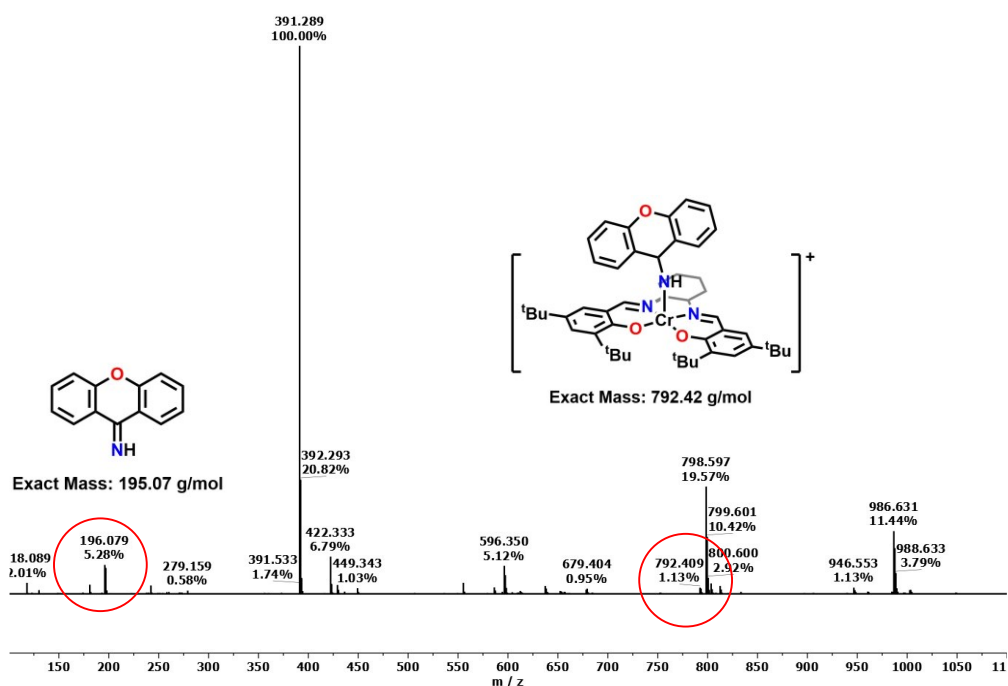
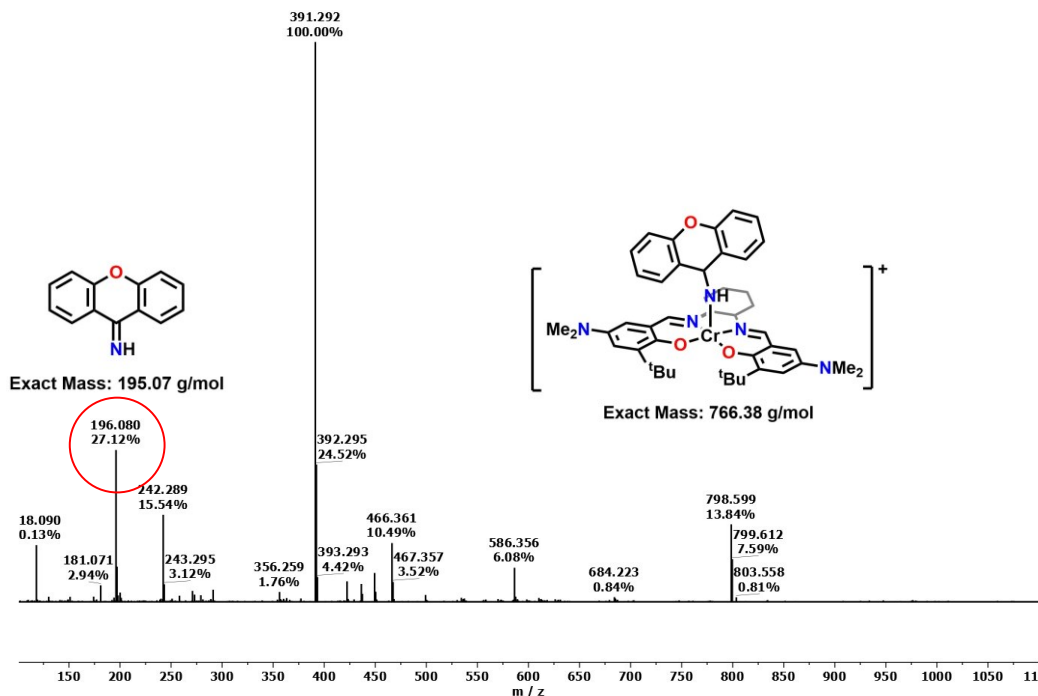
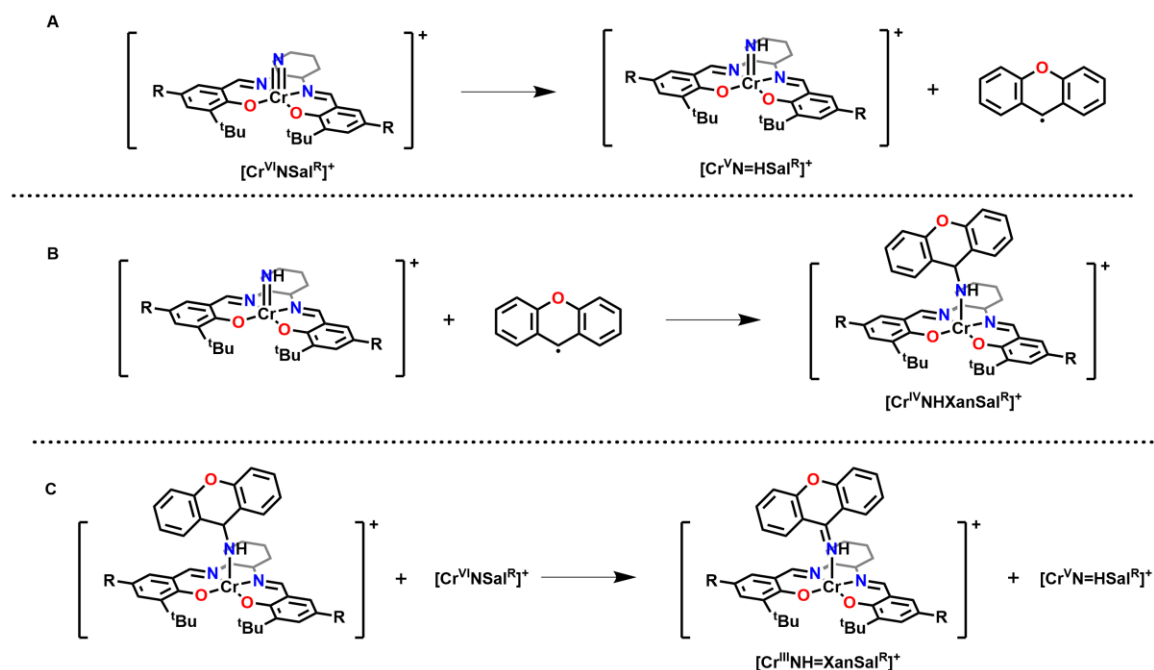


Figure 4.14. Positive-mode ESI-MS spectrum of reaction between  $[\text{CrNSal}^{\text{tBu}}]^+$  and xanthene.



**Figure 4.15. Positive-mode ESI-MS spectrum of reaction between  $[\text{CrNSal}^{\text{NMe}_2}]^+$  and xanthene. No signal corresponding to the  $\text{CrNSal}^{\text{NMe}_2}$ -xanthene N-insertion adduct is observed.**

The C-H bond activation/N-insertion products observed are the same as those observed for  $\text{RuNSal}^{\text{H}}$ , and thus a similar reaction pathway is likely occurring.<sup>68</sup> This pathway is shown in Figure 4.16. First, hydrogen atom transfer (HAT) occurs between  $[\text{CrNSal}^{\text{R}}]^+$  and xanthene to form an alkyl radical and  $[\text{CrN=HSal}^{\text{R}}]^+$  intermediate. The alkyl radical can then react with  $[\text{CrN=HSal}^{\text{R}}]^+$  again in a radical rebound mechanism to form the N-insertion adduct complex. A second hydrogen atom transfer can occur with an additional equivalent of  $[\text{CrNSal}^{\text{R}}]^+$  to form the imine N-insertion product, which exhibits weaker binding and thus is observed as a free ligand under ESI-MS conditions.



**Figure 4.16.** C-H bond activation and N-insertion scheme for the reaction between  $[\text{CrNSal}^{\text{R}}]^+$  ( $\text{R} = \text{CF}_3, \text{tBu}, \text{NMe}_2$ ). The nitride ligand first abstracts hydrogen from xanthene to form an alkyl radical and the imine complex  $[\text{Cr}^{\text{V}}\text{N}=\text{HSal}^{\text{R}}]^+$  (A). Radical rebound occurs next and the  $[\text{Cr}^{\text{IV}}\text{N-HXanSal}^{\text{R}}]^+$  adduct is formed (B). An additional HAT reaction can occur between  $[\text{Cr}^{\text{IV}}\text{N-HXanSal}^{\text{R}}]^+$  and a second equivalent of  $[\text{CrNSal}^{\text{R}}]^+$  to form the weakly coordinated adduct  $[\text{Cr}^{\text{III}}\text{NH}=\text{XanSal}^{\text{R}}]^+$  (C).

### 4.3. Conclusion

$[\text{CrNSal}^{\text{tBu}}]^+$  and  $[\text{CrNSal}^{\text{NMe}_2}]^{*+}$  were reacted with pyridine, chloride and bromide ligands to test whether nitride activation and homocoupling occurs upon binding of an axial ligand to Cr. UV-vis-NIR spectroscopy indicates  $[\text{CrNSal}^{\text{tBu}}]^+$  reacts with all ligands, whereas  $[\text{CrNSal}^{\text{NMe}_2}]^{*+}$  does not react appreciably, highlighting the role the locus of oxidation impacts the reactivity of these complexes. Moreover, chloride appears to exhibit the strongest interaction. DFT studies of the  $[\text{CrNSal}^{\text{tBu}}]^+$ -ligand adducts predict nitride activation with all ligands and similarly provides evidence for the strong chloride binding. Despite the reaction observed via UV-vis-NIR spectroscopy and some evidence for Cr(III) products using ESI-MS, isotopic labelling and GC-MS headspace analysis did not detect  $^{15}\text{N}$  labelled  $\text{N}_2$  gas. Further studies are required to identify the decay pathway of  $[\text{CrNSal}^{\text{R}}]^+$  in the presence of exogenous ligands. The reaction of  $[\text{CrNSal}^{\text{tBu}}]^+$ ,  $[\text{CrNSal}^{\text{CF}_3}]^+$  and  $[\text{CrNSal}^{\text{NMe}_2}]^{*+}$  with xanthene was also investigated. All complexes showed a reaction

based on UV-vis-NIR spectroscopy and ESI-MS, with C-H bond activation/N-insertion products detected. Reaction rate increased with increasing  $\sigma_p$ , suggesting the nitride is acting as an electrophile towards the xanthene substrate. Additional experiments using  $[\text{Cr}^{15}\text{NSal}^{\text{tBu}}]^+$  must be conducted to confirm the origin of the inserted nitrogen atom as the nitride ligand.

## 4.4. Experimental

### 4.4.1. Materials

All chemicals used were obtained from commercial suppliers and used without any further purification unless noted otherwise.  $[(2,4\text{-Br}_2\text{C}_6\text{H}_3)_3\text{N}^+][\text{SbF}_6]^-$  (magic green oxidant) was synthesized according to literature methods.<sup>162</sup> Dry DCM was obtained by refluxing over calcium hydride under  $\text{N}_2$ .

### 4.4.2. Instrumentation

See Section 2.4.2 for full instrumentation details. UV-vis-NIR data was collected on a Cary 5000 spectrophotometer equipped with custom designed immersion fiber-optic probes with a 1 cm path length. GC-MS headspace analysis was performed manually using He carrier gas and an Agilent Technologies 6890 series GC system equipped with a 5973 mass selective detector in splitless injection mode.

### 4.4.3. UV-vis-NIR Monitored Reaction of $[\text{CrNSal}^{\text{R}}]^+$ with Exogenous Ligands

A 5 mL solution of 0.1 mM  $[\text{CrNSal}^{\text{R}}]^+$  in dry DCM was prepared as outlined in Section 3.4.3 under a  $\text{N}_2$  atmosphere and cooled to 253 K. Titrations were performed by adding 10  $\mu\text{L}$  aliquots of 5 mM ligand solutions in dry DCM until one and two equivalents were reached. Spectra were also collected 3 minutes after one equivalent of ligand was added by adding a 100  $\mu\text{L}$  aliquot of 5 mM ligand solutions. The addition of pyridine causes a colour change from brown to orange.

#### 4.4.4. GC-MS Headspace Analysis

Under a N<sub>2</sub> atmosphere, 0.003 mmol of nitride complex was added to a 1.5 mL GC-MS vial and dissolved in 0.3 mL of dry DCM. Stock 0.3 mM ligand solutions were also prepared in 1 mL of dry DCM. A stock solution of magic green oxidant prepared in dry DCM and standardized according to the procedure in Section 3.4.3. All solutions were purged with Ar for 20 minutes before use. The required volume of oxidant solution was added, followed by the addition of 0.1 mL of ligand solution as required. The solution was swirled, then allowed to rest 10 minutes before injection. 1 μL of headspace was injected manually and a peak containing isotopically labelled N<sub>2</sub> gas was detected at 1.10 minutes.

#### 4.4.5. UV-vis-NIR Monitored Reaction of [CrNSal<sup>R</sup>]<sup>+</sup> with Xanthene

A 5 mL solution of 0.1 mM [CrNSal<sup>R</sup>]<sup>+</sup> was prepared as outlined in Section 3.4.3 under a N<sub>2</sub> atmosphere and cooled to 253 K. To this solution was added 100 μL of 0.5 M xanthene in dry DCM and the spectrum was monitored over time. The reaction between [CrNSal<sup>R</sup>]<sup>+</sup> (R = CF<sub>3</sub>, <sup>t</sup>Bu) and xanthene resulted in a colour change from brown to green, in comparison to the reaction between [CrNSal<sup>NMe<sub>2</sub>}]<sup>•+</sup> and xanthene which remained purple.</sup>

#### 4.4.6. Theoretical Analysis

All theoretical analyses were performed using Gaussian 16 (version C.01) software using Compute Canada cluster resources. All analyses used the polarizable continuum model (PCM) with DCM (ε = 8.93) as the solvent. Optimizations and frequency calculations were performed using the B3LYP functional and 6-31g\* basis set. Single point energies and NBO calculations were determined using the UBLYP functional and TZVP basis set. Mayer bond order calculations employed the UBLYP functional and TZVP basis set.

## Chapter 5. Future Directions

### 5.1. Introduction

Chapter 2 focussed on the synthesis and characterization of new CrNSal<sup>R</sup> complexes (R = NO<sub>2</sub>, H, OMe, O<sup>i</sup>Pr, NEt<sub>2</sub>) using XRD, EPR, UV-vis-NIR and theoretical methods. These complexes were then chemically oxidized in Chapter 3 and their loci of oxidation determined using electrochemistry, UV-vis-NIR, EPR and computational methods. Finally, Chapter 4 examined nitride activation and the reactivity of [CrNSal<sup>R</sup>]<sup>+</sup> (R = CF<sub>3</sub>, <sup>t</sup>Bu, NMe<sub>2</sub>) towards exogenous ligands (pyridine, chloride, bromide) and xanthene using UV-vis-NIR, GC-MS headspace analysis, ESI-MS and theoretical methods. Chapter 5 will discuss preliminary work to synthesize new CrNSal<sup>R</sup> derivatives utilizing *para* imine and monoalkylated amine groups, as well as future work regarding nitride activation and C-H bond activation with [CrNSal<sup>R</sup>]<sup>+</sup> (R = NO<sub>2</sub>, CF<sub>3</sub>, H, <sup>t</sup>Bu, OMe, O<sup>i</sup>Pr, NMe<sub>2</sub>, NEt<sub>2</sub>).

### 5.2. Novel R-Group Substituents and Valence Tautomerism

The current series of chromium nitride complexes exhibit ligand radical or high-valent metal center character upon oxidation. Valence tautomer complexes can switch between metal and ligand oxidized states based on environmental stimuli such as temperature and weakly binding ligands. These complexes are desirable for sensing, electronics and reactivity applications. By synthesizing additional oxidized chromium nitride complexes with weakly donating R groups, one can potentially identify the Hammett parameter where this property occurs. However, salen ligands bearing R- groups with sigma Hammett parameter values between -0.83 and -0.45 (corresponding to NMe<sub>2</sub> and O<sup>i</sup>Pr respectively) are unknown in literature. To this end, I propose chromium salen nitride complexes containing R = N=Ph ( $\sigma_p = -0.55$ ) and R = NHPh ( $\sigma_p = -0.56$ ) and will discuss current progress along their synthetic routes.<sup>105</sup>

#### 5.2.1. Synthesis of R = N=Bn Derivative

To synthesize salen ligand derivatives containing nitrogen atom donors, it is often necessary to form primary amine intermediates. However, attempts to hydrogenate the nitro group presumably lead to condensation between the aldehyde and amine formed *in*

*situ*. To circumvent this issue, the aldehyde must be protected using ethylene glycol to form the corresponding acetal. The hydrogenation then proceeds to completion, and the amine can be reacted with aromatic aldehydes to generate the desired imine. Interestingly, the use of further substituted aromatic aldehydes could provide further tuning of donation strength to the metal center. Deprotection in aqueous acetone liberates the target aldehyde.<sup>178</sup> Currently, the protected imine has been synthesized, however protecting group removal to furnish the aldehyde needs further development.

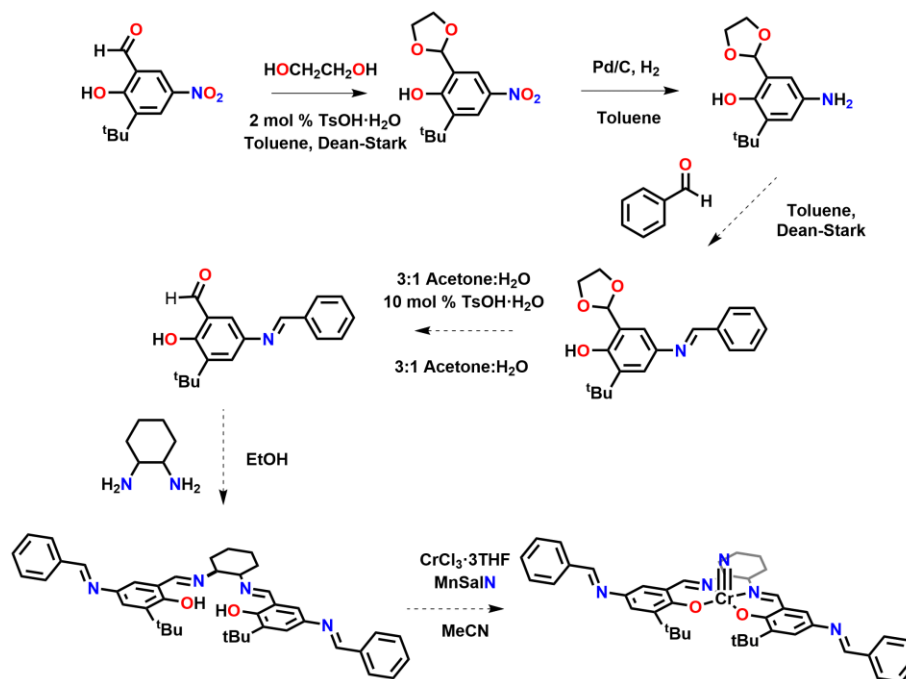


**Figure 5.1.** Proposed synthetic route to chromium salen nitrde complexes bearing para imine groups.

### Synthesis of 2-(tert-butyl)-6-(1,3-dioxolan-2-yl)-4-nitrophenol

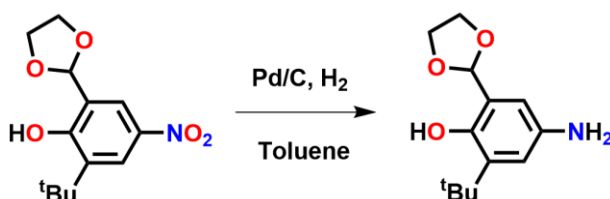


To 1.000 g (4.48 mmol) of 3-(tert-butyl)-2-hydroxy-5-nitrobenzaldehyde was added 0.5 mL (8.97 mmol) ethylene glycol and 0.016 g (0.08 mmol) p-toluenesulfonic acid monohydrate. The solution was refluxed overnight using a Dean-Stark apparatus until all starting material was consumed. The solution was concentrated *in vacuo* to a yellow oil. (Note: The ethylene glycol protecting group is prone to hydrolysis at this step. Best results



were found when the crude product was left in dry toluene from refluxing and directly hydrogenated without further concentration or purification.) Yield: 1.367 g (5.12 mmol, 114%). ESI-MS  $m/z$ : 268.11  $\{M+H\}^+$  100%.  $^1H$  NMR (400 MHz,  $CDCl_3$ ):  $\delta$  (d,  $J = 2.8$  Hz, 1H, ArH [ $H_A$ ]), (d,  $J = 2.8$  Hz, 1H, ArH [ $H_A$ ]), (s, 1H, CH [ $H_B$ ]), (m, 2H,  $CH_2$  [ $H_B$ ]), (m, 2H,  $CH_2$  [ $H_C$ ]), 1.41 (s, 9H,  $C(CH_3)_3$  [ $H_C$ ]). See Appendix D - Figure D1 for full NMR spectrum.

### Synthesis of 4-amino-2-(tert-butyl)-6-(1,3-dioxolan-2-yl)phenol



To approximately 1.000 g (3.74 mmol) of 2-(tert-butyl)-6-(1,3-dioxolan-2-yl)-4-nitrophenol in 30mL toluene was added 0.100 g of 5% Pd/C. The solution was purged and refilled with hydrogen gas and stirred 48 hours until complete disappearance of starting material via TLC. The yellow solution was filtered over celite, after which the solution turned dark purple. The solution was concentrated *in vacuo* to a purple oil. (Note: The ethylene glycol protecting group is prone to hydrolysis at this step. Best results were found when the crude product was left in dry toluene from refluxing and directly hydrogenated without further concentration or purification.) Yield: 0.479 g (2.02 mmol, 54%). ESI-MS  $m/z$ : 238.14  $\{M+H\}^+$  100%.  $^1H$  NMR (400 MHz,  $CDCl_3$ ):  $\delta$  6.73 (d,  $J = 2.8$  Hz, 1H, ArH [ $H_A$ ]), 6.55 (d,  $J = 2.8$  Hz, 1H, ArH [ $H_A$ ]), 5.86 (s, 1H, CH [ $H_B$ ]), 4.17 (m, 2H,  $CH_2$  [ $H_B$ ]), 4.08 (m, 2H,  $CH_2$  [ $H_C$ ]), 1.41 (s, 9H,  $C(CH_3)_3$  [ $H_C$ ]). See Appendix D - Figure D2 for full spectrum.

### 5.2.2. Synthesis of R = NHPH Derivative

Similar challenges to imine substituted salens arise when synthesizing secondary amine derivatives. Any amine intermediates formed will condense with aldehydes present. In addition, the copper catalyzed coupling conditions require further protection of the phenol group to avoid coupling of the aryl bromide to the phenolate. The phenol protected intermediate can then undergo Suzuki coupling with the amine of interest, followed by deprotection in aqueous acetone and Pd/C hydrogenation.<sup>178,179</sup> Protection of the phenol has been achieved, but further protection, Suzuki coupling, and deprotection to obtain the target aldehyde remains incomplete.

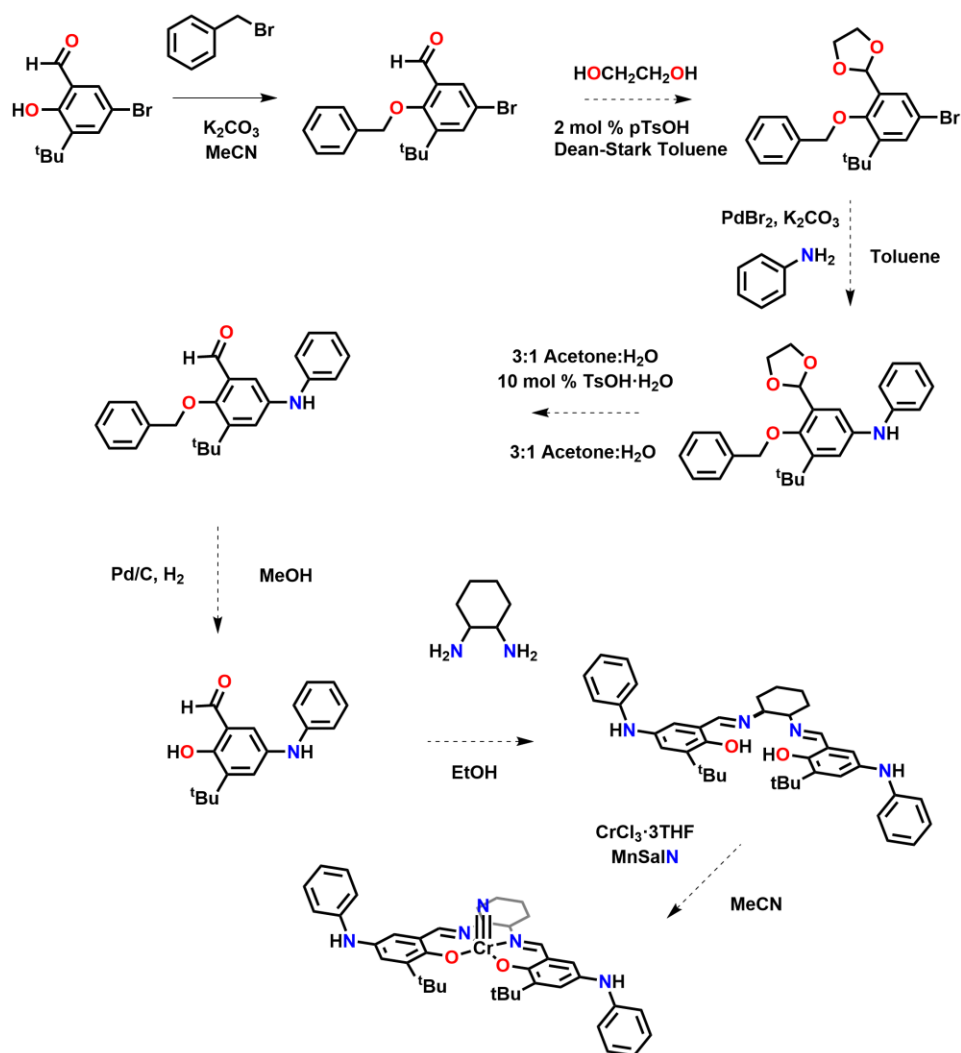
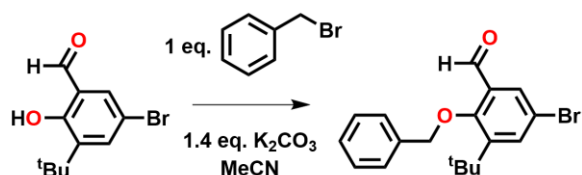


Figure 5.2. Proposed synthetic route to secondary amine groups at *para* positions of the aromatic rings.

### Synthesis of 2-(benzyloxy)-5-bromo-3-(tert-butyl)benzaldehyde



To 3.000 g (11.67 mmol) of 5-bromo-3-(tert-butyl)-2-hydroxybenzaldehyde dissolved in 30mL acetonitrile was added 2.258 g (16.34 mmol) of potassium carbonate. The solution turned green, and 1.39 mL (11.67 mmol) of benzyl bromide was added. A yellow green suspension formed overnight, and the acetonitrile was removed *in vacuo*. The solid was redissolved in dichloromethane and filtered over celite. Removal of filtrate

solvent in vacuo yielded a yellow brown oil. Yield: 4.021 g (11.58 mmol, 99%). ESI-MS  $m/z$ : 347.06 {M+H+} 100%.  $^1\text{H}$  NMR (400 MHz,  $\text{CDCl}_3$ ):  $\delta$  10.27 (s, 1H, O=CH [ $\text{H}_\text{A}$ ]), 7.88 (d,  $J = 2.6$  Hz, 1H, ArH [ $\text{H}_\text{A}$ ]), 7.73 (d,  $J = 2.6$  Hz, 1H, ArH [ $\text{H}_\text{B}$ ]), 7.46 (m, 5H, ArH<sub>5</sub> [ $\text{H}_\text{B}$ ]), 5.07 (s, 2H, CH<sub>2</sub> [ $\text{H}_\text{C}$ ]), 1.46 (s, 9H, C(CH<sub>3</sub>)<sub>3</sub> [ $\text{H}_\text{C}$ ]). See Appendix D - Figure D3 for full spectrum.

## 5.3. Ligand Accelerated C-H Bond Activation and Homocoupling

### 5.3.1. Reactivity Studies Using UV-vis-NIR and GC-MS

Spectroscopic data and ESI-MS indicates C-H bond activation is occurring between oxidized chromium salen nitrides and xanthene. Many transition metal oxo and nitride complexes feature increased reactivity in the presence of exogenous ligands. UV-vis-NIR data suggests a reaction is occurring with  $[\text{CrNSal}^{\text{tBu}}]^+$  and exogenous ligands, but homocoupling could not be confirmed. It is still unknown how the addition of ligands affects the relative rates of homocoupling versus hydrogen atom abstraction, as well as whether the identity of the ligand would favor one pathway (Figure 5.3). In order to minimize homocoupling and favor C-H bond activation, more dilute concentrations of  $\text{CrNSal}^{\text{R}}$  are required in a longer pathlength cell (5 cm). However, we are limited with our current setup in keeping the reaction at low temperatures under inert atmosphere.

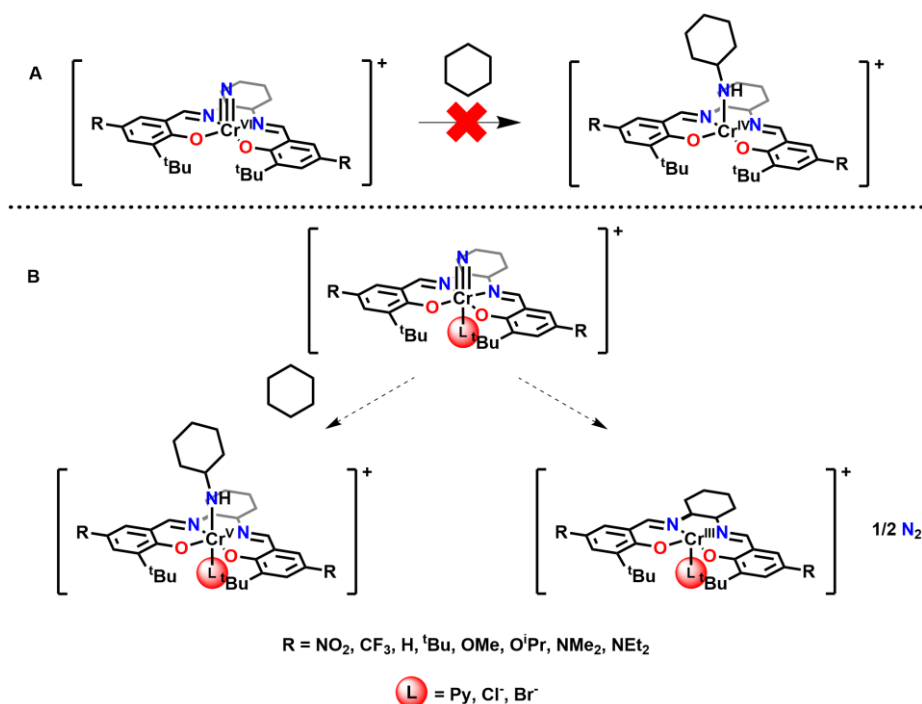


**Figure 5.3.** Potential increase of C-H bond activation reactivity upon axial binding of exogenous ligand. No reaction with stronger C-H bonds substrates such as cyclohexane occurs with oxidized CrNSal<sup>R</sup> in absence of exogenous ligand (A). The addition of exogenous ligand could increase the reactivity of the nitride ligand towards C-H bond activation or could accelerate the competing homocoupling pathway (B).

[CrNSal<sup>R</sup>]<sup>+</sup> and xanthene undergo nitride insertion reactions based on ESI-MS data. Interestingly, a reaction is also observed via UV-vis-NIR spectroscopy between 9,10-dihydroanthracene (C-H BDE: 76.3 kcal/mol) and [CrNSal<sup>CF<sub>3</sub></sup>]<sup>+</sup> and [CrNSal<sup>tBu</sup>]<sup>+</sup>, whereas little reaction is observed with [CrNSal<sup>NMe<sub>2</sub></sup>]<sup>+</sup> as shown in Figure 5.4. Reactions with [CrNSal<sup>CF<sub>3</sub></sup>]<sup>+</sup> and [CrNSal<sup>tBu</sup>]<sup>+</sup> exhibit clear isosbestic points, indicating clean conversion to a new species. In addition, the reaction between 9,10-dihydroanthracene and [CrNSal<sup>CF<sub>3</sub></sup>]<sup>+</sup> occurs significantly faster than with [CrNSal<sup>tBu</sup>]<sup>+</sup>, in agreement with the nitride acting as an electrophile. However, ESI-MS does not reveal a nitride insertion product for any of the complexes tested. This is consistent with Man's ruthenium salen nitride system, where desaturation products are observed as C-H bond strength increases.<sup>68</sup> In order to understand the reaction pathway and verify C-H bond activation is occurring, the predicted anthracene product or other N-insertion product(s) need to be identified via GC-MS. This will both identify the potential desaturation products of the reaction as well as quantify the

products of the reaction, providing insight into how favoured C-H bond activation is over homocoupling.

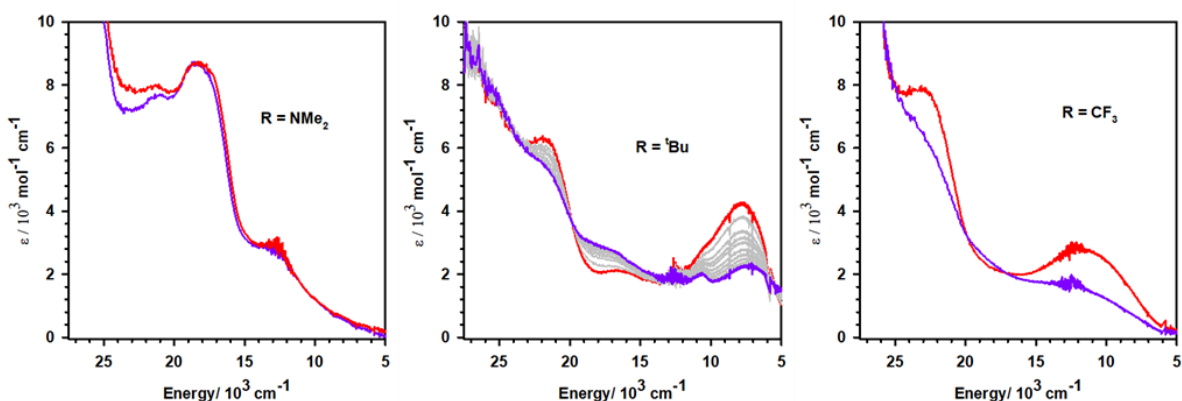


**Figure 5.4.** UV-vis-NIR spectra for the reaction between  $[\text{CrNSal}^{\text{R}}]^+$  and 9,10-dihydroanthracene. Conditions: 0.1 mM  $[\text{CrNSal}^{\text{R}}]^+$ ; 10 mM 9,10-dihydroanthracene;  $T = 253 \text{ K}$ ;  $\text{CH}_2\text{Cl}_2$ . Red =  $[\text{CrNSal}^{\text{R}}]^+$ ; grey = intermediate scans over time; purple = 2 hours after addition of 9,10-dihydroanthracene.

The exogenous ligands investigated in this study included pyridine, bromide and chloride. UV-vis-NIR suggests the strongest interaction occurs between chloride and  $[\text{CrNSal}^{\text{tBu}}]^+$ , which could be attributed to the strong electrostatic interaction between ions and hard Lewis base pairing between Cr(VI). Therefore, the fluoride ion could interact even more strongly with  $[\text{CrNSal}^{\text{tBu}}]^+$  and increase the reactivity of the nitride ligand even further, making it a valuable inclusion to the current ligand series.

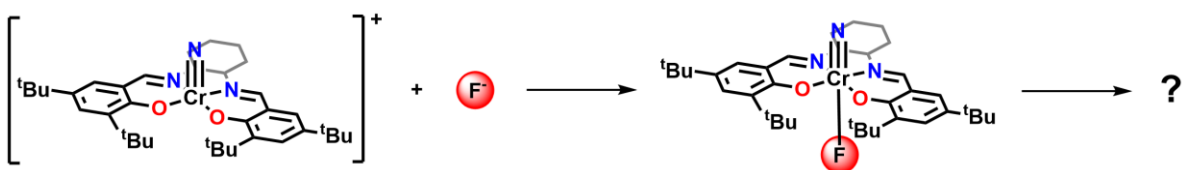


**Figure 5.5.** The reaction of  $[\text{CrNSal}^{\text{tBu}}]^+$  with the fluoride anion ligand.

### 5.3.2. Homocoupling and C-H Bond Activation

GC-MS headspace analysis could not confirm the presence of isotopically labelled nitrogen gas following the addition of chloride to oxidized  $\text{Cr}^{15}\text{NSal}^{\text{tBu}}$ . However, there are significant reaction rate differences depending on whether pyridine, chloride, or bromide is used. Chloride causes the fastest decay, followed by bromide then pyridine. Section

4.2.3 theoretically examined the interaction of one ligand and one  $[\text{CrNSal}^{\text{tBu}}]^+$  complex and investigated changes indicative of nitride activation.

Another method to probe the difference in reaction rate with different ligands is computationally modeling the transition state when two of the oxidized chromium salen nitride complexes come together. Depending on the relative energies of the transition state, a significantly lower transition state may be observed for one of the ligand adducts, and all should be more accessible than in the absence of an exogenous ligand. Moreover, this will provide insight into whether both oxidized chromium salen nitride complexes must be ligated for the decay to occur (Figure 5.5). The results of this study may confirm why kinetics studies are challenging for this system if there are complex equilibria and ligation of all complexes is not required for homocoupling to occur.

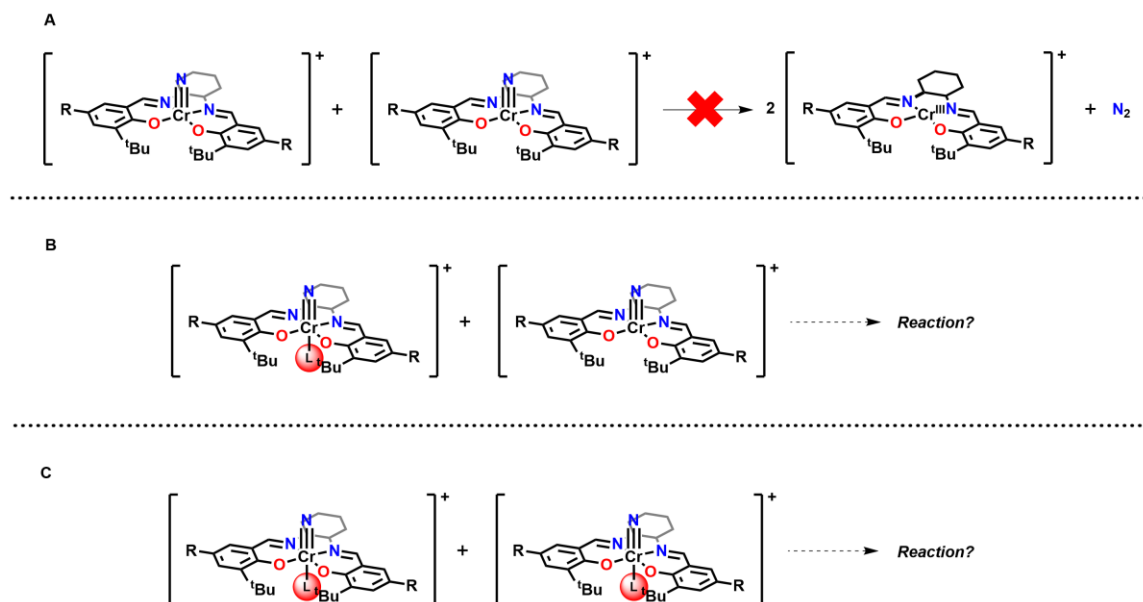


**Figure 5.6.** Future work regarding nitride activation and homocoupling. No reaction occurs in the absence of an exogenous ligand L (A). It is unknown if a reaction will occur if only one of the  $[\text{CrNSal}^{\text{R}}]^+$  complexes contains an axial ligand (B), or if both complexes must be coordinated by axial ligands (C).

## 5.4. Conclusion

Novel Cr salen nitride complexes were synthesized containing *para*  $\text{R} = \text{NO}_2$ , H, OMe, O<sup>i</sup>Pr and  $\text{NEt}_2$  groups. The complexes were chemically oxidized and their electronic structure investigated using electrochemistry, UV-vis-NIR, EPR and DFT. Based on the

data collected so far, oxidation of  $\text{Cr}^{\text{V}}\text{NSal}^{\text{R}}$  ( $\text{R} = \text{NO}_2, \text{H}, \text{OMe}, \text{O}^i\text{Pr}$ ) yields metal oxidized  $\text{Cr}^{\text{VI}}\text{NSal}^{\text{R}}$ , and oxidation of  $\text{Cr}^{\text{V}}\text{NSal}^{\text{NEt}_2}$  yields a ligand radical  $[\text{Cr}^{\text{V}}\text{NSal}^{\text{NEt}_2}]^{\bullet+}$ . Interactions between previously characterized  $[\text{CrNSal}^{\text{tBu}}]^+$  and  $[\text{Cr}^{\text{V}}\text{NSal}^{\text{NMe}_2}]^{\bullet+}$  and exogenous ligands ( $\text{L} = \text{Py}, \text{Cl}^-, \text{Br}^-$ ) were investigated to determine whether nitride activation and homocoupling occurs upon axial ligand binding to Cr. The locus of oxidation strongly influences this interaction, with a reaction observed for  $[\text{CrNSal}^{\text{tBu}}]^+$  and all ligands, whereas no reaction occurs for  $[\text{Cr}^{\text{V}}\text{NSal}^{\text{NMe}_2}]^{\bullet+}$  and any ligands based on UV-vis-NIR spectroscopy. DFT analysis of the different  $[\text{CrNSal}^{\text{tBu}}]^+ \text{-L}$  adducts supports activation of the nitride ligand based on increased  $\text{Cr}\equiv\text{N}$  bond length and planarity of the  $\text{CrSal}$  unit. However, attempts to identify the product(s) of the reaction were unsuccessful.  $[\text{CrNSal}^{\text{R}}]^+$  ( $\text{R} = \text{CF}_3, \text{tBu}, \text{NMe}_2$ ) also react with xanthene to form N-insertion products as detected by UV-vis-NIR and ESI-MS. This C-H bond activation reaction occurs faster as the  $\sigma_{\text{p}}$  increases, in accordance with the nitride acting as an electrophile.

Future work with  $\text{CrNSal}^{\text{R}}$  will continue searching for the  $\sigma_{\text{p}}$  where the locus of oxidation changes by synthesizing new *para* substituted salen ligands. Additional experimental methods such as XAS will help verify the locus of oxidation for  $[\text{CrNSal}^{\text{R}}]^+$ .  $\text{CrNSal}^{\text{R}}$  ( $\text{R} = \text{OMe}, \text{O}^i\text{Pr}, \text{NMe}_2, \text{NEt}_2$ ) exhibit additional redox processes at relatively low potentials which remain poorly explored with respect to electronic structure and reactivity. While homocoupling in the presence of an exogenous ligand could not be confirmed, the product of the reaction remains elusive, and work is ongoing to probe whether a simple ligand-complex interaction is occurring or activation of the nitride towards dimerization. Other methods of nitride activation such as temperature and UV light remain unexplored. In addition to xanthene,  $[\text{CrNSal}^{\text{R}}]^+$  may also react with stronger C-H bonds such as cyclohexane depending on the salen R-group. Moreover,  $[\text{CrNSal}^{\text{R}}]^+$  may perform N-insertion reactions with other substrates such as alkenes and alkynes, highlighting the wide reaction scope of these complexes. While chloride appears to activate the nitride the strongest in comparison to bromide and pyridine, it is unknown whether it is the optimal ligand for reactivity applications.

## References

- (1) Luo, Q.; Lu, C.; Liu, L.; Zhu, M. A Review on the Synthesis of Transition Metal Nitride Nanostructures and Their Energy Related Applications. *Green Energy Environ.* **2023**, *8* (2), 406–437. <https://doi.org/10.1016/j.gee.2022.07.002>.
- (2) Wang, H.; Li, J.; Li, K.; Lin, Y.; Chen, J.; Gao, L.; Nicolosi, V.; Xiao, X.; Lee, J.-M. Transition Metal Nitrides for Electrochemical Energy Applications. *Chem. Soc. Rev.* **2021**, *50* (2), 1354–1390. <https://doi.org/10.1039/D0CS00415D>.
- (3) Guler, U.; Shalaev, V. M.; Boltasseva, A. Nanoparticle Plasmonics: Going Practical with Transition Metal Nitrides. *Mater. Today* **2015**, *18* (4), 227–237. <https://doi.org/10.1016/j.mattod.2014.10.039>.
- (4) Xie, J.; Xie, Y. Transition Metal Nitrides for Electrocatalytic Energy Conversion: Opportunities and Challenges. *Chem. – Eur. J.* **2016**, *22* (11), 3588–3598. <https://doi.org/10.1002/chem.201501120>.
- (5) Shi, J.; Jiang, B.; Li, C.; Yan, F.; Wang, D.; Yang, C.; Wan, J. Review of Transition Metal Nitrides and Transition Metal Nitrides/Carbon Nanocomposites for Supercapacitor Electrodes. *Mater. Chem. Phys.* **2020**, *245*, 122533. <https://doi.org/10.1016/j.matchemphys.2019.122533>.
- (6) Eklund, P.; Kerdsonpanya, S.; Alling, B. Transition-Metal-Nitride-Based Thin Films as Novel Energy Harvesting Materials. *J. Mater. Chem. C* **2016**, *4* (18), 3905–3914. <https://doi.org/10.1039/C5TC03891J>.
- (7) Peng, X.; Pi, C.; Zhang, X.; Li, S.; Huo, K.; K. Chu, P. Recent Progress of Transition Metal Nitrides for Efficient Electrocatalytic Water Splitting. *Sustain. Energy Fuels* **2019**, *3* (2), 366–381. <https://doi.org/10.1039/C8SE00525G>.
- (8) Kumar, D. D.; Kumar, N.; Kalaiselvam, S.; Dash, S.; Jayavel, R. Wear Resistant Super-Hard Multilayer Transition Metal-Nitride Coatings. *Surf. Interfaces* **2017**, *7*, 74–82. <https://doi.org/10.1016/j.surfin.2017.03.001>.
- (9) Tareen, A. K.; Priyanga, G. S.; Behara, S.; Thomas, T.; Yang, M. Mixed Ternary Transition Metal Nitrides: A Comprehensive Review of Synthesis, Electronic Structure, and Properties of Engineering Relevance. *Prog. Solid State Chem.* **2019**, *53*, 1–26. <https://doi.org/10.1016/j.progsolidstchem.2018.11.001>.
- (10) Dehnicke, K.; Strähle, J. Nitrido Complexes of Transition Metals. *Angew. Chem. Int. Ed. Engl.* **1992**, *31* (8), 955–978. <https://doi.org/10.1002/anie.199209551>.
- (11) Rittle, J.; Peters, J. C. An Fe-N<sub>2</sub> Complex That Generates Hydrazine and Ammonia via Fe=NNH<sub>2</sub>: Demonstrating a Hybrid Distal-to-Alternating Pathway for N<sub>2</sub> Reduction. *J. Am. Chem. Soc.* **2016**, *138* (12), 4243–4248. <https://doi.org/10.1021/jacs.6b01230>.
- (12) Roux, Y.; Duboc, C.; Gennari, M. Molecular Catalysts for N<sub>2</sub> Reduction: State of the Art, Mechanism, and Challenges. *ChemPhysChem* **2017**, *18* (19), 2606–2617. <https://doi.org/10.1002/cphc.201700665>.
- (13) Park, S. Y.; Jang, Y. J.; Youn, D. H. A Review of Transition Metal Nitride-Based Catalysts for Electrochemical Nitrogen Reduction to Ammonia. *Catalysts* **2023**, *13* (3), 639. <https://doi.org/10.3390/catal13030639>.
- (14) Galloway, J. N.; Townsend, A. R.; Erisman, J. W.; Bekunda, M.; Cai, Z.; Freney, J. R.; Martinelli, L. A.; Seitzinger, S. P.; Sutton, M. A. Transformation of the Nitrogen Cycle: Recent Trends, Questions, and Potential Solutions. *Science* **2008**, *320* (5878), 889–892. <https://doi.org/10.1126/science.1136674>.
- (15) Liu, D.; Wang, C.; Yu, Y.; Zhao, B.-H.; Wang, W.; Du, Y.; Zhang, B. Understanding the Nature of Ammonia Treatment to Synthesize Oxygen Vacancy-



- Enriched Transition Metal Oxides. *Chem* **2019**, *5* (2), 376–389.  
<https://doi.org/10.1016/j.chempr.2018.11.001>.
- (16) Erdemir, D.; Dincer, I. A Perspective on the Use of Ammonia as a Clean Fuel: Challenges and Solutions. *Int. J. Energy Res.* **2021**, *45* (4), 4827–4834.  
<https://doi.org/10.1002/er.6232>.
- (17) Sonker, M.; Tiwary, S. K.; Shreyash, N.; Bajpai, S.; Ray, M.; Kar, S. K.; Balathanigaimani, M. S. Ammonia as an Alternative Fuel for Vehicular Applications: Paving the Way for Adsorbed Ammonia and Direct Ammonia Fuel Cells. *J. Clean. Prod.* **2022**, *376*, 133960. <https://doi.org/10.1016/j.jclepro.2022.133960>.
- (18) Foster, S. L.; Bakovic, S. I. P.; Duda, R. D.; Maheshwari, S.; Milton, R. D.; Minteer, S. D.; Janik, M. J.; Renner, J. N.; Greenlee, L. F. Catalysts for Nitrogen Reduction to Ammonia. *Nat. Catal.* **2018**, *1* (7), 490–500.  
<https://doi.org/10.1038/s41929-018-0092-7>.
- (19) Kandemir, T.; Schuster, M. E.; Senyshyn, A.; Behrens, M.; Schlögl, R. The Haber–Bosch Process Revisited: On the Real Structure and Stability of “Ammonia Iron” under Working Conditions. *Angew. Chem. Int. Ed.* **2013**, *52* (48), 12723–12726. <https://doi.org/10.1002/anie.201305812>.
- (20) Einsle, O.; Rees, D. C. Structural Enzymology of Nitrogenase Enzymes. *Chem. Rev.* **2020**, *120* (12), 4969–5004. <https://doi.org/10.1021/acs.chemrev.0c00067>.
- (21) Rutledge, H. L.; Cook, B. D.; Nguyen, H. P. M.; Herzik, M. A.; Tezcan, F. A. Structures of the Nitrogenase Complex Prepared under Catalytic Turnover Conditions. *Science* **2022**, *377* (6608), 865–869.  
<https://doi.org/10.1126/science.abq7641>.
- (22) The PyMOL Molecular Graphics System.
- (23) Sippel, D.; Rohde, M.; Netzer, J.; Trncik, C.; Gies, J.; Grunau, K.; Djurdjevic, I.; Decamps, L.; Andrade, S. L. A.; Einsle, O. A Bound Reaction Intermediate Sheds Light on the Mechanism of Nitrogenase. *Science* **2018**, *359* (6383), 1484–1489.  
<https://doi.org/10.1126/science.aar2765>.
- (24) Čorić, I.; Holland, P. L. Insight into the Iron–Molybdenum Cofactor of Nitrogenase from Synthetic Iron Complexes with Sulfur, Carbon, and Hydride Ligands. *J. Am. Chem. Soc.* **2016**, *138* (23), 7200–7211. <https://doi.org/10.1021/jacs.6b00747>.
- (25) Yandulov, D. V.; Schrock, R. R. Catalytic Reduction of Dinitrogen to Ammonia at a Single Molybdenum Center. *Science* **2003**, *301* (5629), 76–78.  
<https://doi.org/10.1126/science.1085326>.
- (26) Anderson, J. S.; Rittle, J.; Peters, J. C. Catalytic Conversion of Nitrogen to Ammonia by an Iron Model Complex. *Nature* **2013**, *501* (7465), 84–87.  
<https://doi.org/10.1038/nature12435>.
- (27) Anderson, J. S.; Cutsail, G. E.; Rittle, J.; Connor, B. A.; Gunderson, W. A.; Zhang, L.; Hoffman, B. M.; Peters, J. C. Characterization of an Fe≡N–NH<sub>2</sub> Intermediate Relevant to Catalytic N<sub>2</sub> Reduction to NH<sub>3</sub>. *J. Am. Chem. Soc.* **2015**, *137* (24), 7803–7809. <https://doi.org/10.1021/jacs.5b03432>.
- (28) Fajardo, J.; Peters, J. C. Tripodal P<sub>3</sub>XFe–N<sub>2</sub> Complexes (X = B, Al, Ga): Effect of the Apical Atom on Bonding, Electronic Structure, and Catalytic N<sub>2</sub>-to-NH<sub>3</sub> Conversion. *Inorg. Chem.* **2021**, *60* (2), 1220–1227.  
<https://doi.org/10.1021/acs.inorgchem.0c03354>.
- (29) Yang, X.; Xu, B.; Chen, J. G.; Yang, X. Recent Progress in Electrochemical Nitrogen Reduction on Transition Metal Nitrides. *ChemSusChem* **2023**, *16* (5), e202201715. <https://doi.org/10.1002/cssc.202201715>.
- (30) Minteer, S. D.; Christopher, P.; Linic, S. Recent Developments in Nitrogen Reduction Catalysts: A Virtual Issue. *ACS Energy Lett.* **2019**, *4* (1), 163–166.  
<https://doi.org/10.1021/acsenerylett.8b02197>.

- (31) Dunn, P. L.; Cook, B. J.; Johnson, S. I.; Appel, A. M.; Bullock, R. M. Oxidation of Ammonia with Molecular Complexes. *J. Am. Chem. Soc.* **2020**, *142* (42), 17845–17858. <https://doi.org/10.1021/jacs.0c08269>.
- (32) Bhattacharya, P.; Heiden, Z. M.; Chambers, G. M.; Johnson, S. I.; Bullock, R. M.; Mock, M. T. Catalytic Ammonia Oxidation to Dinitrogen by Hydrogen Atom Abstraction. *Angew. Chem. Int. Ed.* **2019**, *58* (34), 11618–11624. <https://doi.org/10.1002/anie.201903221>.
- (33) Dunn, P. L.; Johnson, S. I.; Kaminsky, W.; Bullock, R. M. Diversion of Catalytic C–N Bond Formation to Catalytic Oxidation of NH<sub>3</sub> through Modification of the Hydrogen Atom Abstraction. *J. Am. Chem. Soc.* **2020**, *142* (7), 3361–3365. <https://doi.org/10.1021/jacs.9b13706>.
- (34) Habibzadeh, F.; Miller, S. L.; Hamann, T. W.; Smith, M. R. Homogeneous Electrocatalytic Oxidation of Ammonia to N<sub>2</sub> under Mild Conditions. *Proc. Natl. Acad. Sci.* **2019**, *116* (8), 2849–2853. <https://doi.org/10.1073/pnas.1813368116>.
- (35) Li, Y.; Chen, J.-Y.; Miao, Q.; Yu, X.; Feng, L.; Liao, R.-Z.; Ye, S.; Tung, C.-H.; Wang, W. A Parent Iron Amido Complex in Catalysis of Ammonia Oxidation. *J. Am. Chem. Soc.* **2022**, *144* (10), 4365–4375. <https://doi.org/10.1021/jacs.1c08609>.
- (36) Nakajima, K.; Toda, H.; Sakata, K.; Nishibayashi, Y. Ruthenium-Catalysed Oxidative Conversion of Ammonia into Dinitrogen. *Nat. Chem.* **2019**, *11* (8), 702–709. <https://doi.org/10.1038/s41557-019-0293-y>.
- (37) Zott, M. D.; Garrido-Barros, P.; Peters, J. C. Electrocatalytic Ammonia Oxidation Mediated by a Polypyridyl Iron Catalyst. *ACS Catal.* **2019**, *9* (11), 10101–10108. <https://doi.org/10.1021/acscatal.9b03499>.
- (38) Ballhausen, C. J.; Gray, H. B. The Electronic Structure of the Vanadyl Ion. *Inorg. Chem.* **1962**, *1* (1), 111–122. <https://doi.org/10.1021/ic50001a022>.
- (39) Winkler, J. R.; Gray, H. B. Electronic Structures of Oxo-Metal Ions. In *Molecular Electronic Structures of Transition Metal Complexes I*; Mingos, D. M. P., Day, P., Dahl, J. P., Eds.; Structure and Bonding; Springer: Berlin, Heidelberg, 2012; pp 17–28. [https://doi.org/10.1007/430\\_2011\\_55](https://doi.org/10.1007/430_2011_55).
- (40) Smith, J. M. Reactive Transition Metal Nitride Complexes. In *Progress in Inorganic Chemistry Volume 58*; John Wiley & Sons, Ltd, 2014; pp 417–470. <https://doi.org/10.1002/9781118792797.ch06>.
- (41) Anderson, T. M.; Neiwert, W. A.; Kirk, M. L.; Piccoli, P. M. B.; Schultz, A. J.; Koetzle, T. F.; Musaev, D. G.; Morokuma, K.; Cao, R.; Hill, C. L. A Late-Transition Metal Oxo Complex: K<sub>7</sub>Na<sub>9</sub>[O=PtIV(H<sub>2</sub>O)L<sub>2</sub>], L = [PW<sub>9</sub>O<sub>34</sub>]<sup>9-</sup>. *Science* **2004**, *306* (5704), 2074–2077. <https://doi.org/10.1126/science.1104696>.
- (42) Carroll, M. E.; Pinter, B.; Carroll, P. J.; Mindiola, D. J. Mononuclear and Terminally Bound Titanium Nitrides. *J. Am. Chem. Soc.* **2015**, *137* (28), 8884–8887. <https://doi.org/10.1021/jacs.5b04853>.
- (43) Grant, L. N.; Bhunia, M.; Pinter, B.; Rebreyend, C.; Carroll, M. E.; Carroll, P. J.; de Bruin, B.; Mindiola, D. J. Pursuit of an Electron Deficient Titanium Nitride. *Inorg. Chem.* **2021**, *60* (8), 5635–5646. <https://doi.org/10.1021/acs.inorgchem.0c03644>.
- (44) Grant, L. N.; Pinter, B.; Kurogi, T.; Carroll, M. E.; Wu, G.; Manor, B. C.; Carroll, P. J.; Mindiola, D. J. Molecular Titanium Nitrides: Nucleophiles Unleashed. *Chem. Sci.* **2017**, *8* (2), 1209–1224. <https://doi.org/10.1039/C6SC03422E>.
- (45) Tran, B. L.; Singhal, M.; Park, H.; Lam, O. P.; Pink, M.; Krzystek, J.; Ozarowski, A.; Telser, J.; Meyer, K.; Mindiola, D. J. Reactivity Studies of a Masked Three-Coordinate Vanadium(II) Complex. *Angew. Chem. Int. Ed.* **2010**, *49* (51), 9871–9875. <https://doi.org/10.1002/anie.201005029>.

- (46) Tran, B. L.; Pink, M.; Gao, X.; Park, H.; Mindiola, D. J. Low-Coordinate and Neutral Nitrido Complexes of Vanadium. *J. Am. Chem. Soc.* **2010**, *132* (5), 1458–1459. <https://doi.org/10.1021/ja908303k>.
- (47) Clough, C. R.; Greco, J. B.; Figueroa, J. S.; Diaconescu, P. L.; Davis, W. M.; Cummins, C. C. Organic Nitriles from Acid Chlorides: An Isovalent N for (O)Cl Exchange Reaction Mediated by a Tungsten Nitride Complex. *J. Am. Chem. Soc.* **2004**, *126* (25), 7742–7743. <https://doi.org/10.1021/ja0492438>.
- (48) Bindl, M.; Stade, R.; Heilmann, E. K.; Picot, A.; Goddard, R.; Fürstner, A. Molybdenum Nitride Complexes with Ph<sub>3</sub>SiO Ligands Are Exceedingly Practical and Tolerant Precatalysts for Alkyne Metathesis and Efficient Nitrogen Transfer Agents. *J. Am. Chem. Soc.* **2009**, *131* (27), 9468–9470. <https://doi.org/10.1021/ja903259g>.
- (49) Curley, J. J.; Sceats, E. L.; Cummins, C. C. A Cycle for Organic Nitrile Synthesis via Dinitrogen Cleavage. *J. Am. Chem. Soc.* **2006**, *128* (43), 14036–14037. <https://doi.org/10.1021/ja066090a>.
- (50) Bendix, J.; Anthon, C.; Schau-Magnussen, M.; Brock-Nannestad, T.; Vibenholt, J.; Rehman, M.; Sauer, S. P. A. Heterobimetallic Nitride Complexes from Terminal Chromium(V) Nitride Complexes: Hyperfine Coupling Increases with Distance. *Angew. Chem. Int. Ed.* **2011**, *50* (19), 4480–4483. <https://doi.org/10.1002/anie.201008153>.
- (51) Hedegaard, E. D.; Schau-Magnussen, M.; Bendix, J. [Cr(N)(Acac)<sub>2</sub>]: A Simple Chromium Nitride Complex and Its Reactivity towards Late Transition Metals. *Inorg. Chem. Commun.* **2011**, *14* (5), 719–721. <https://doi.org/10.1016/j.inoche.2011.02.015>.
- (52) Groves, J. T.; Takahashi, T. Activation and Transfer of Nitrogen from a Nitridomanganese(V) Porphyrin Complex. Aza Analog of Epoxidation. *J. Am. Chem. Soc.* **1983**, *105* (7), 2073–2074. <https://doi.org/10.1021/ja00345a071>.
- (53) Shi, H.; Lee, H. K.; Pan, Y.; Lau, K.-C.; Yiu, S.-M.; Lam, W. W. Y.; Man, W.-L.; Lau, T.-C. Structure and Reactivity of a Manganese(VI) Nitrido Complex Bearing a Tetraamido Macrocyclic Ligand. *J. Am. Chem. Soc.* **2021**, *143* (38), 15863–15872. <https://doi.org/10.1021/jacs.1c08072>.
- (54) Bolzati, C.; Dolmella, A. Nitrido Technetium-99 m Core in Radiopharmaceutical Applications: Four Decades of Research. *Inorganics* **2020**, *8* (1), 3. <https://doi.org/10.3390/inorganics8010003>.
- (55) Meng, F.; Kuriyama, S.; Egi, A.; Tanaka, H.; Yoshizawa, K.; Nishibayashi, Y. Preparation and Reactivity of Rhenium–Nitride Complexes Bearing PNP-Type Pincer Ligands toward Nitrogen Fixation. *Organometallics* **2023**, *42* (11), 1065–1076. <https://doi.org/10.1021/acs.organomet.2c00312>.
- (56) P. Connor, G.; Delony, D.; E. Weber, J.; Q. Mercado, B.; B. Curley, J.; Schneider, S.; M. Mayer, J.; L. Holland, P. Facile Conversion of Ammonia to a Nitride in a Rhenium System That Cleaves Dinitrogen. *Chem. Sci.* **2022**, *13* (14), 4010–4018. <https://doi.org/10.1039/D1SC04503B>.
- (57) van Alten, R. S.; Wieser, P. A.; Finger, M.; Abbenseth, J.; Demeshko, S.; Würtele, C.; Siewert, I.; Schneider, S. Halide Effects in Reductive Splitting of Dinitrogen with Rhenium Pincer Complexes. *Inorg. Chem.* **2022**. <https://doi.org/10.1021/acs.inorgchem.2c00973>.
- (58) Wang, H.-X.; Wu, L.; Zheng, B.; Du, L.; To, W.-P.; Ko, C.-H.; Phillips, D. L.; Che, C.-M. C–H Activation by an Iron-Nitrido Bis-Pocket Porphyrin Species. *Angew. Chem. Int. Ed.* **2021**, *60* (9), 4796–4803. <https://doi.org/10.1002/anie.202014191>.
- (59) Crandell, D. W.; Muñoz, S. B.; Smith, J. M.; Baik, M.-H. Mechanistic Study of Styrene Aziridination by Iron(IV) Nitrides. *Chem. Sci.* **2018**, *9* (45), 8542–8552. <https://doi.org/10.1039/C8SC03677B>.

- (60) Lindley, B. M.; Bruch, Q. J.; White, P. S.; Hasanayn, F.; Miller, A. J. M. Ammonia Synthesis from a Pincer Ruthenium Nitride via Metal–Ligand Cooperative Proton-Coupled Electron Transfer. *J. Am. Chem. Soc.* **2017**, *139* (15), 5305–5308. <https://doi.org/10.1021/jacs.7b01323>.
- (61) Fajardo, J.; Peters, J. C. Catalytic Nitrogen-to-Ammonia Conversion by Osmium and Ruthenium Complexes. *J. Am. Chem. Soc.* **2017**, *139* (45), 16105–16108. <https://doi.org/10.1021/jacs.7b10204>.
- (62) Thompson, N. B.; Green, M. T.; Peters, J. C. Nitrogen Fixation via a Terminal Fe(IV) Nitride. *J. Am. Chem. Soc.* **2017**, *139* (43), 15312–15315. <https://doi.org/10.1021/jacs.7b09364>.
- (63) Betley, T. A.; Peters, J. C. A Tetrahedrally Coordinated L3Fe–Nx Platform That Accommodates Terminal Nitride (FeIV:N) and Dinitrogen (FeI–N2–FeI) Ligands. *J. Am. Chem. Soc.* **2004**, *126* (20), 6252–6254. <https://doi.org/10.1021/ja048713v>.
- (64) Maity, A. K.; Murillo, J.; Metta-Magaña, A. J.; Pinter, B.; Fortier, S. A Terminal Iron(IV) Nitride Supported by a Super Bulky Guanidinate Ligand and Examination of Its Electronic Structure and Reactivity. *J. Am. Chem. Soc.* **2017**, *139* (44), 15691–15700. <https://doi.org/10.1021/jacs.7b06919>.
- (65) Schendzielorz, F. S.; Finger, M.; Volkmann, C.; Würtele, C.; Schneider, S. A Terminal Osmium(IV) Nitride: Ammonia Formation and Ambiphilic Reactivity. *Angew. Chem. Int. Ed.* **2016**, *55* (38), 11417–11420. <https://doi.org/10.1002/anie.201604917>.
- (66) Man, W.-L.; Lam, W. W. Y.; Yiu, S.-M.; Lau, T.-C.; Peng, S.-M. Direct Aziridination of Alkenes by a Cationic (Salen)Ruthenium(VI) Nitrido Complex. *J. Am. Chem. Soc.* **2004**, *126* (47), 15336–15337. <https://doi.org/10.1021/ja045845f>.
- (67) Man, W.-L.; Xie, J.; Lo, P.-K.; Lam, W. W. Y.; Yiu, S.-M.; Lau, K.-C.; Lau, T.-C. Functionalization of Alkynes by a (Salen)Ruthenium(VI) Nitrido Complex. *Angew. Chem.* **2014**, *126* (32), 8603–8606. <https://doi.org/10.1002/ange.201404421>.
- (68) Man, W.-L.; Lam, W. W. Y.; Kwong, H.-K.; Yiu, S.-M.; Lau, T.-C. Ligand-Accelerated Activation of Strong C–H Bonds of Alkanes by a (Salen)Ruthenium(VI)–Nitrido Complex. *Angew. Chem. Int. Ed.* **2012**, *51* (36), 9101–9104. <https://doi.org/10.1002/anie.201204136>.
- (69) Hojilla Atienza, C. C.; Bowman, A. C.; Lobkovsky, E.; Chirik, P. J. Photolysis and Thermolysis of Bis(Imino)Pyridine Cobalt Azides: C–H Activation from Putative Cobalt Nitrido Complexes. *J. Am. Chem. Soc.* **2010**, *132* (46), 16343–16345. <https://doi.org/10.1021/ja107288x>.
- (70) Zolnhofer, E. M.; Käß, M.; Khusniyarov, M. M.; Heinemann, F. W.; Maron, L.; van Gastel, M.; Bill, E.; Meyer, K. An Intermediate Cobalt(IV) Nitrido Complex and Its N-Migratory Insertion Product. *J. Am. Chem. Soc.* **2014**, *136* (42), 15072–15078. <https://doi.org/10.1021/ja508144j>.
- (71) Vreeken, V.; Siegler, M. A.; de Bruin, B.; Reek, J. N. H.; Lutz, M.; van der Vlugt, J. I. C–H Activation of Benzene by a Photoactivated Ni(II)(Azide): Formation of a Transient Nickel Nitrido Complex. *Angew. Chem. Int. Ed.* **2015**, *54* (24), 7055–7059. <https://doi.org/10.1002/anie.201501437>.
- (72) Scheibel, M. G.; Askevold, B.; Heinemann, F. W.; Reijerse, E. J.; de Bruin, B.; Schneider, S. Closed-Shell and Open-Shell Square-Planar Iridium Nitrido Complexes. *Nat. Chem.* **2012**, *4* (7), 552–558. <https://doi.org/10.1038/nchem.1368>.
- (73) Scheibel, M. G.; Wu, Y.; Stückl, A. C.; Krause, L.; Carl, E.; Stalke, D.; de Bruin, B.; Schneider, S. Synthesis and Reactivity of a Transient, Terminal Nitrido Complex of Rhodium. *J. Am. Chem. Soc.* **2013**, *135* (47), 17719–17722. <https://doi.org/10.1021/ja409764j>.

- (74) Jørgensen, Chr. K. Differences between the Four Halide Ligands, and Discussion Remarks on Trigonal-Bipyramidal Complexes, on Oxidation States, and on Diagonal Elements of One-Electron Energy. *Coord. Chem. Rev.* **1966**, *1* (1), 164–178. [https://doi.org/10.1016/S0010-8545\(00\)80170-8](https://doi.org/10.1016/S0010-8545(00)80170-8).
- (75) de Bruin, B.; Gualco, P.; Paul, N. D. Redox Non-Innocent Ligands. In *Ligand Design in Metal Chemistry*; John Wiley & Sons, Ltd, 2016; pp 176–204. <https://doi.org/10.1002/9781118839621.ch7>.
- (76) D. Ward, M.; A. McCleverty, J. Non-Innocent Behaviour in Mononuclear and Polynuclear Complexes: Consequences for Redox and Electronic Spectroscopic Properties. *J. Chem. Soc. Dalton Trans.* **2002**, *0* (3), 275–288. <https://doi.org/10.1039/B110131P>.
- (77) Lyaskovskyy, V.; de Bruin, B. Redox Non-Innocent Ligands: Versatile New Tools to Control Catalytic Reactions. *ACS Catal.* **2012**, *2* (2), 270–279. <https://doi.org/10.1021/cs200660v>.
- (78) Kaim, W. Concepts for Metal Complex Chromophores Absorbing in the near Infrared. *Coord. Chem. Rev.* **2011**, *255* (21), 2503–2513. <https://doi.org/10.1016/j.ccr.2011.01.014>.
- (79) Chirik, P. J.; Wieghardt, K. Radical Ligands Confer Nobility on Base-Metal Catalysts. *Science* **2010**, *327* (5967), 794–795. <https://doi.org/10.1126/science.1183281>.
- (80) Dzik, W. I.; van der Vlugt, J. I.; Reek, J. N. H.; de Bruin, B. Ligands That Store and Release Electrons during Catalysis. *Angew. Chem. Int. Ed.* **2011**, *50* (15), 3356–3358. <https://doi.org/10.1002/anie.201006778>.
- (81) Denisov, I. G.; Makris, T. M.; Sligar, S. G.; Schlichting, I. Structure and Chemistry of Cytochrome P450. *Chem. Rev.* **2005**, *105* (6), 2253–2278. <https://doi.org/10.1021/cr0307143>.
- (82) Wilderman, P. R.; Shah, M. B.; Liu, T.; Li, S.; Hsu, S.; Roberts, A. G.; Goodlett, D. R.; Zhang, Q.; Woods, V. L.; Stout, C. D.; Halpert, J. R. Plasticity of Cytochrome P450 2B4 as Investigated by Hydrogen-Deuterium Exchange Mass Spectrometry and X-Ray Crystallography\*. *J. Biol. Chem.* **2010**, *285* (49), 38602–38611. <https://doi.org/10.1074/jbc.M110.180646>.
- (83) Ito, N.; Phillips, S. E. V.; Stevens, C.; Ogel, Z. B.; McPherson, M. J.; Keen, J. N.; Yadav, K. D. S.; Knowles, P. F. Novel Thioether Bond Revealed by a 1.7 Å Crystal Structure of Galactose Oxidase. *Nature* **1991**, *350* (6313), 87–90. <https://doi.org/10.1038/350087a0>.
- (84) Ito, N.; Phillips, S. E. V.; Yadav, K. D. S.; Knowles, P. F. Crystal Structure of a Free Radical Enzyme, Galactose Oxidase. *J. Mol. Biol.* **1994**, *238* (5), 794–814. <https://doi.org/10.1006/jmbi.1994.1335>.
- (85) Whittaker, J. W. Free Radical Catalysis by Galactose Oxidase. *Chem. Rev.* **2003**, *103* (6), 2347–2364. <https://doi.org/10.1021/cr020425z>.
- (86) Whittaker, M. M.; Whittaker, J. W. The Active Site of Galactose Oxidase. *J. Biol. Chem.* **1988**, *263* (13), 6074–6080. [https://doi.org/10.1016/S0021-9258\(18\)68751-4](https://doi.org/10.1016/S0021-9258(18)68751-4).
- (87) Whittaker, M. M.; Whittaker, J. W. A Tyrosine-Derived Free Radical in Apogalactose Oxidase. *J. Biol. Chem.* **1990**, *265* (17), 9610–9613. [https://doi.org/10.1016/S0021-9258\(19\)38711-3](https://doi.org/10.1016/S0021-9258(19)38711-3).
- (88) Whittaker, M. M.; DeVito, V. L.; Asher, S. A.; Whittaker, J. W. Resonance Raman Evidence for Tyrosine Involvement in the Radical Site of Galactose Oxidase. *J. Biol. Chem.* **1989**, *264* (13), 7104–7106. [https://doi.org/10.1016/S0021-9258\(18\)83205-7](https://doi.org/10.1016/S0021-9258(18)83205-7).
- (89) Que, L.; Tolman, W. B. Biologically Inspired Oxidation Catalysis. *Nature* **2008**, *455* (7211), 333–340. <https://doi.org/10.1038/nature07371>.

- (90) Kaim, W.; Schwederski, B. Non-Innocent Ligands in Bioinorganic Chemistry—An Overview. *Coord. Chem. Rev.* **2010**, *254* (13), 1580–1588. <https://doi.org/10.1016/j.ccr.2010.01.009>.
- (91) Kleij, A. W. Nonsymmetrical Salen Ligands and Their Complexes: Synthesis and Applications. *Eur. J. Inorg. Chem.* **2009**, *2009* (2), 193–205. <https://doi.org/10.1002/ejic.200800936>.
- (92) Shaw, S.; White, J. D. Asymmetric Catalysis Using Chiral Salen–Metal Complexes: Recent Advances. *Chem. Rev.* **2019**, *119* (16), 9381–9426. <https://doi.org/10.1021/acs.chemrev.9b00074>.
- (93) J. Whiteoak, C.; Salassa, G.; W. Kleij, A. Recent Advances with  $\pi$ -Conjugated Salen Systems. *Chem. Soc. Rev.* **2012**, *41* (2), 622–631. <https://doi.org/10.1039/C1CS15170C>.
- (94) Herasymchuk, K.; Chiang, L.; Hayes, C. E.; Brown, M. L.; Ovens, J. S.; Patrick, B. O.; Leznoff, D. B.; Storr, T. Synthesis and Electronic Structure Determination of Uranium(VI) Ligand Radical Complexes. *Dalton Trans.* **2016**, *45* (31), 12576–12586. <https://doi.org/10.1039/C6DT02089E>.
- (95) Chiang, L.; Savard, D.; Shimazaki, Y.; Thomas, F.; Storr, T. FeIII Bipyrrrodine Phenoxide Complexes and Their Oxidized Analogues. *Inorg. Chem.* **2014**, *53* (11), 5810–5819. <https://doi.org/10.1021/ic500663x>.
- (96) Chiang, L.; Kochem, A.; Jarjays, O.; Dunn, T. J.; Vezin, H.; Sakaguchi, M.; Ogura, T.; Orio, M.; Shimazaki, Y.; Thomas, F.; Storr, T. Radical Localization in a Series of Symmetric NiII Complexes with Oxidized Salen Ligands. *Chem. – Eur. J.* **2012**, *18* (44), 14117–14127. <https://doi.org/10.1002/chem.201201410>.
- (97) Clarke, R. M.; Herasymchuk, K.; Storr, T. Electronic Structure Elucidation in Oxidized Metal–Salen Complexes. *Coord. Chem. Rev.* **2017**, *352*, 67–82. <https://doi.org/10.1016/j.ccr.2017.08.019>.
- (98) Lyons, C. T.; Stack, T. D. P. Recent Advances in Phenoxy Radical Complexes of Salen-Type Ligands as Mixed-Valent Galactose Oxidase Models. *Coord. Chem. Rev.* **2013**, *257* (2), 528–540. <https://doi.org/10.1016/j.ccr.2012.06.003>.
- (99) Thomas, F. Ligand-Centred Oxidative Chemistry in Sterically Hindered Salen Complexes: An Interesting Case with Nickel. *Dalton Trans.* **2016**, *45* (27), 10866–10877. <https://doi.org/10.1039/C6DT00942E>.
- (100) Storr, T.; Wasinger, E. C.; Pratt, R. C.; Stack, T. D. P. The Geometric and Electronic Structure of a One-Electron-Oxidized Nickel(II) Bis(Salicylidene)Diamine Complex. *Angew. Chem. Int. Ed.* **2007**, *46* (27), 5198–5201. <https://doi.org/10.1002/anie.200701194>.
- (101) Kurahashi, T.; Fujii, H. One-Electron Oxidation of Electronically Diverse Manganese(III) and Nickel(II) Salen Complexes: Transition from Localized to Delocalized Mixed-Valence Ligand Radicals. *J. Am. Chem. Soc.* **2011**, *133* (21), 8307–8316. <https://doi.org/10.1021/ja2016813>.
- (102) Storr, T.; Verma, P.; Pratt, R. C.; Wasinger, E. C.; Shimazaki, Y.; Stack, T. D. P. Defining the Electronic and Geometric Structure of One-Electron Oxidized Copper–Bis-Phenoxide Complexes. *J. Am. Chem. Soc.* **2008**, *130* (46), 15448–15459. <https://doi.org/10.1021/ja804339m>.
- (103) Tezgerevska, T.; Alley, K. G.; Boskovic, C. Valence Tautomerism in Metal Complexes: Stimulated and Reversible Intramolecular Electron Transfer between Metal Centers and Organic Ligands. *Coord. Chem. Rev.* **2014**, *268*, 23–40. <https://doi.org/10.1016/j.ccr.2014.01.014>.
- (104) Chiang, L.; Herasymchuk, K.; Thomas, F.; Storr, T. Influence of Electron-Withdrawing Substituents on the Electronic Structure of Oxidized Ni and Cu Salen

- Complexes. *Inorg. Chem.* **2015**, *54* (12), 5970–5980.  
<https://doi.org/10.1021/acs.inorgchem.5b00783>.
- (105) Hansch, Corwin.; Leo, A.; Taft, R. W. A Survey of Hammett Substituent Constants and Resonance and Field Parameters. *Chem. Rev.* **1991**, *91* (2), 165–195. <https://doi.org/10.1021/cr00002a004>.
- (106) Clarke, R. M.; Storr, T. Tuning Electronic Structure To Control Manganese Nitride Activation. *J. Am. Chem. Soc.* **2016**, *138* (47), 15299–15302.  
<https://doi.org/10.1021/jacs.6b09576>.
- (107) Hein, N. M.; MacNeil, G. A.; Storr, T. Elaboration on the Electronics of Salen Manganese Nitrides: Investigations into Alkoxy-Substituted Ligand Scaffolds. *Inorg. Chem.* **2021**, *60* (22), 16895–16905. <https://doi.org/10.1021/acs.inorgchem.1c02668>.
- (108) Martelino, D.; Mahato, S.; VandeVen, W.; Hein, N. M.; Clarke, R. M.; MacNeil, G. A.; Thomas, F.; Storr, T. Chromium Nitride Umpolung Tuned by the Locus of Oxidation. *J. Am. Chem. Soc.* **2022**. <https://doi.org/10.1021/jacs.2c01840>.
- (109) Coggon, P.; McPhail, A. T.; Mabbs, F. E.; Richards, A.; Thornley, A. S. Preparation, Magnetic, and Electronic Spectral Properties of Some Chromium(III)–NN'-Ethylenebis(Salicylideneiminato) Complexes: Crystal and Molecular Structure of NN'-Ethylenebis(Salicylideneiminato)Diaquochromium(III) Chloride. *J. Chem. Soc. Inorg. Phys. Theor.* **1970**, No. 0, 3296–3303. <https://doi.org/10.1039/J19700003296>.
- (110) Bandini, M.; Cozzi, P. G.; Umani-Ronchi, A. [Cr(Salen)] as a 'Bridge' between Asymmetric Catalysis, Lewis Acids and Redox Processes. *Chem. Commun.* **2002**, No. 9, 919–927. <https://doi.org/10.1039/B109945K>.
- (111) Schaus, S. E.; Brånalt, J.; Jacobsen, E. N. Asymmetric Hetero-Diels–Alder Reactions Catalyzed by Chiral (Salen)Chromium(III) Complexes. *J. Org. Chem.* **1998**, *63* (2), 403–405. <https://doi.org/10.1021/jo971758c>.
- (112) Jacobsen, E. N. Asymmetric Catalysis of Epoxide Ring-Opening Reactions. *Acc. Chem. Res.* **2000**, *33* (6), 421–431. <https://doi.org/10.1021/ar960061v>.
- (113) Siddall, T. L.; Miyaura, N.; Huffman, J. C.; Kochi, J. K. Isolation and Molecular Structure of Unusual Oxochromium(V) Cations for the Catalytic Epoxidation of Alkenes. *J. Chem. Soc. Chem. Commun.* **1983**, No. 21, 1185–1186.  
<https://doi.org/10.1039/C39830001185>.
- (114) Jacobsen, E. N.; Zhang, W.; Muci, A. R.; Ecker, J. R.; Deng, L. Highly Enantioselective Epoxidation Catalysts Derived from 1,2-Diaminocyclohexane. *J. Am. Chem. Soc.* **1991**, *113* (18), 7063–7064. <https://doi.org/10.1021/ja00018a068>.
- (115) McGarrigle, E. M.; Gilheany, D. G. Chromium- and Manganese-salen Promoted Epoxidation of Alkenes. *Chem. Rev.* **2005**, *105* (5), 1563–1602.  
<https://doi.org/10.1021/cr0306945>.
- (116) Samsel, E. G.; Srinivasan, K.; Kochi, J. K. Mechanism of the Chromium-Catalyzed Epoxidation of Olefins. Role of Oxochromium(V) Cations. *J. Am. Chem. Soc.* **1985**, *107* (25), 7606–7617. <https://doi.org/10.1021/ja00311a064>.
- (117) McGarrigle, E. M.; Murphy, D. M.; Gilheany, D. G. Ligand Tuning in the Chromium–Salen-Mediated Asymmetric Epoxidation of Alkenes. *Tetrahedron Asymmetry* **2004**, *15* (8), 1343–1354. <https://doi.org/10.1016/j.tetasy.2004.03.010>.
- (118) O'Mahony, C. P.; McGarrigle, E. M.; Renehan, M. F.; Ryan, K. M.; Kerrigan, N. J.; Bousquet, C.; Gilheany, D. G. Asymmetric Alkene Epoxidation with Chromium Oxo Salen Complexes. A Systematic Study of Salen Ligand Substituents. *Org. Lett.* **2001**, *3* (22), 3435–3438. <https://doi.org/10.1021/ol010144y>.
- (119) Venkataramanan, N. S.; Prem Singh, S.; Rajagopal, S.; Pitchumani, K. Electronic and Steric Effects on the Oxygenation of Organic Sulfides and Sulfoxides with Oxo(Salen)Chromium(V) Complexes. *J. Org. Chem.* **2003**, *68* (19), 7460–7470.  
<https://doi.org/10.1021/jo034558b>.

- (120) Groves, J. T.; Kruper, W. J.; Haushalter, R. C.; Butler, W. M. Synthesis, Characterization, and Molecular Structure of Oxo(Porphyrinato)Chromium(IV) Complexes. *Inorg. Chem.* **1982**, *21* (4), 1363–1368. <https://doi.org/10.1021/ic00134a018>.
- (121) Groves, J. T.; Takahashi, T.; Butler, W. M. Synthesis and Molecular Structure of a Nitrido(Porphyrinato)Chromium(V) Complex. *Inorg. Chem.* **1983**, *22* (6), 884–887. <https://doi.org/10.1021/ic00148a009>.
- (122) Du Bois, J.; Hong, J.; Carreira, E. M.; Day, M. W. Nitrogen Transfer from a Nitridomanganese(V) Complex: Amination of Silyl Enol Ethers. *J. Am. Chem. Soc.* **1996**, *118* (4), 915–916. <https://doi.org/10.1021/ja953659r>.
- (123) Du Bois, J.; Tomooka, C. S.; Hong, J.; Carreira, E. M. Nitridomanganese(V) Complexes: Design, Preparation, and Use as Nitrogen Atom-Transfer Reagents. *Acc. Chem. Res.* **1997**, *30* (9), 364–372. <https://doi.org/10.1021/ar960222v>.
- (124) Odom, A. L.; Cummins, C. C.; Protasiewicz, J. D. Nitric Oxide Cleavage: Synthesis of Terminal Chromium(VI) Nitrido Complexes via Nitrosyl Deoxygenation. *J. Am. Chem. Soc.* **1995**, *117* (24), 6613–6614. <https://doi.org/10.1021/ja00129a034>.
- (125) Dreher, A.; Mersmann, K.; Näther, C.; Ivanovic-Burmazovic, I.; van Eldik, R.; Tuczek, F. Structural, Spectroscopic, and Kinetic Investigation of the Molybdenum Dialkylhydrazido Complexes [MoBr(NNC5H10)(Dppe)2]Br and [Mo(NNC5H10)(Dppe)2]: Activation Parameters and Revised Mechanism for N–N Cleavage. *Inorg. Chem.* **2009**, *48* (5), 2078–2093. <https://doi.org/10.1021/ic801952v>.
- (126) Leung, S. K.-Y.; Huang, J.-S.; Liang, J.-L.; Che, C.-M.; Zhou, Z.-Y. Nitrido Ruthenium Porphyrins: Synthesis, Characterization, and Amination Reactions with Hydrocarbon or Silyl Enol Ethers. *Angew. Chem. Int. Ed.* **2003**, *42* (3), 340–343. <https://doi.org/10.1002/anie.200390111>.
- (127) Birk, T.; Bendix, J. Atom Transfer as a Preparative Tool in Coordination Chemistry. Synthesis and Characterization of Cr(V) Nitrido Complexes of Bidentate Ligands. *Inorg. Chem.* **2003**, *42* (23), 7608–7615. <https://doi.org/10.1021/ic034777f>.
- (128) Neely, F. L.; Bottomley, L. A. Inter-Metal Nitrogen Atom Transfer Reactions between Nitridochromium(V) and Chromium(III) Porphyrins. *Inorg. Chem.* **1997**, *36* (24), 5432–5434. <https://doi.org/10.1021/ic960918k>.
- (129) Bottomley, L. A.; Neely, F. L. Stereoelectronic Aspects of Inter-Metal Nitrogen Atom Transfer Reactions between Nitridomanganese(V) and Chromium(III) Porphyrins. *Inorg. Chem.* **1997**, *36* (24), 5435–5439. <https://doi.org/10.1021/ic960919c>.
- (130) Pain, T.; Mondal, S.; Jena, S.; Dutta Gupta, D.; Biswal, H. S.; Kar, S. Synthesis, Characterization, and the N Atom Transfer Reactivity of a Nitridochromium(V) Complex Stabilized by a Corrolato Ligand. *ACS Omega* **2022**, *7* (32), 28138–28147. <https://doi.org/10.1021/acsomega.2c02267>.
- (131) Michel, F.; Hamman, S.; Philouze, C.; Valle, C. P. D.; Saint-Aman, E.; Thomas, F. Galactose Oxidase Models: Insights from <sup>19</sup>F NMR Spectroscopy. *Dalton Trans.* **2009**, No. 5, 832–842. <https://doi.org/10.1039/B813036A>.
- (132) Braun, M.; Fleischer, R.; Mai, B.; Schneider, M.-A.; Lachenicht, S. The Regioisomeric Triphenylaminoethanols –Comparison of Their Efficiency in Enantioselective Catalysis. *Adv. Synth. Catal.* **2004**, *346* (4), 474–482. <https://doi.org/10.1002/adsc.200303178>.
- (133) Leung, W.-H.; Chan, E. Y. Y.; Chow, E. K. F.; Williams, I. D.; Peng, S.-M. Metal Complexes of a Chiral Quadridentate Schiff Base. *J. Chem. Soc. Dalton Trans.* **1996**, No. 7, 1229–1236. <https://doi.org/10.1039/DT9960001229>.



- (134) Belokon', Y. N.; Harrington, R. W.; North, M.; Young, C. In Situ Formation of Heterobimetallic Salen Complexes Containing Titanium and/or Vanadium Ions. *Inorg. Chem.* **2008**, *47* (9), 3801–3814. <https://doi.org/10.1021/ic702451a>.
- (135) Kochem, A.; Kanso, H.; Baptiste, B.; Arora, H.; Philouze, C.; Jarjayes, O.; Vezin, H.; Luneau, D.; Orio, M.; Thomas, F. Ligand Contributions to the Electronic Structures of the Oxidized Cobalt(II) Salen Complexes. *Inorg. Chem.* **2012**, *51* (20), 10557–10571. <https://doi.org/10.1021/ic300763t>.
- (136) Chiang, L.; Kochem, A.; Jarjayes, O.; Dunn, T. J.; Vezin, H.; Sakaguchi, M.; Ogura, T.; Orio, M.; Shimazaki, Y.; Thomas, F.; Storr, T. Radical Localization in a Series of Symmetric NiII Complexes with Oxidized Salen Ligands. *Chem. – Eur. J.* **2012**, *18* (44), 14117–14127. <https://doi.org/10.1002/chem.201201410>.
- (137) Mascarenhas, C. M.; Miller, S. P.; White, P. S.; Morken, J. P. First Catalytic Asymmetric Aldol-Tishchenko Reaction—Insight into the Catalyst Structure and Reaction Mechanism. *Angew. Chem. Int. Ed.* **2001**, *40* (3), 601–603. [https://doi.org/10.1002/1521-3773\(20010202\)40:3<601::AID-ANIE601>3.0.CO;2-W](https://doi.org/10.1002/1521-3773(20010202)40:3<601::AID-ANIE601>3.0.CO;2-W).
- (138) Price, C. C.; Belanger, W. J. The Rate of Saponification of Some Alkyl M- and p-Dialkylaminobenzoates. *J. Am. Chem. Soc.* **1954**, *76* (10), 2682–2684. <https://doi.org/10.1021/ja01639a025>.
- (139) Herkstroeter, W. G. Mechanism of Syn-Anti Isomerization of Azomethine Dyes. *J. Am. Chem. Soc.* **1973**, *95* (26), 8686–8691. <https://doi.org/10.1021/ja00807a030>.
- (140) Azuma, N.; Imori, Y.; Yoshida, H.; Tajima, K.; Li, Y.; Yamauchi, J. Crystal Structure and ESR Study of a Nitrochromium(V) Complex. *Inorganica Chim. Acta* **1997**, *266* (1), 29–36. [https://doi.org/10.1016/S0020-1693\(97\)05528-X](https://doi.org/10.1016/S0020-1693(97)05528-X).
- (141) MATLAB, 2023.
- (142) Stoll, S.; Schweiger, A. EasySpin, a Comprehensive Software Package for Spectral Simulation and Analysis in EPR. *J. Magn. Reson.* **2006**, *178* (1), 42–55. <https://doi.org/10.1016/j.jmr.2005.08.013>.
- (143) M. Roessler, M.; Salvadori, E. Principles and Applications of EPR Spectroscopy in the Chemical Sciences. *Chem. Soc. Rev.* **2018**, *47* (8), 2534–2553. <https://doi.org/10.1039/C6CS00565A>.
- (144) Bendix, J. [Cr(N)Cl<sub>4</sub>]<sup>2-</sup>: A Simple Nitrido Complex Synthesized by Nitrogen-Atom Transfer. *J. Am. Chem. Soc.* **2003**, *125* (44), 13348–13349. <https://doi.org/10.1021/ja0371000>.
- (145) SADABS, 2003.
- (146) TWINABS, 2007.
- (147) TWINABS, 2008.
- (148) SAINT, 1997.
- (149) Altomare, A.; Burla, M. C.; Camalli, M.; Casciarano, G. L.; Giacovazzo, C.; Guagliardi, A.; Moliterni, A. G. G.; Polidori, G.; Spagna, R. SIR97: A New Tool for Crystal Structure Determination and Refinement. *J. Appl. Crystallogr.* **1999**, *32* (1), 115–119. <https://doi.org/10.1107/S0021889898007717>.
- (150) Altomare, A.; Casciarano, G.; Giacovazzo, C.; Guagliardi, A. Completion and Refinement of Crystal Structures with SIR92. *J. Appl. Crystallogr.* **1993**, *26* (3), 343–350. <https://doi.org/10.1107/S0021889892010331>.
- (151) SHELXTL, 1997.
- (152) Farrugia, L. J. ORTEP-3 for Windows - a Version of ORTEP-III with a Graphical User Interface (GUI). *J. Appl. Crystallogr.* **1997**, *30* (5), 565–565. <https://doi.org/10.1107/S0021889897003117>.
- (153) Robin, M. B.; Day, P. Mixed Valence Chemistry-A Survey and Classification. In *Advances in Inorganic Chemistry and Radiochemistry*; Elsevier, 1968; Vol. 10, pp 247–422. [https://doi.org/10.1016/S0065-2792\(08\)60179-X](https://doi.org/10.1016/S0065-2792(08)60179-X).

- (154) Cowan, D. O.; Kaufman, F. Organic Solid State. Electron Transfer in a Mixed Valence Salt of Biferrocene. *J. Am. Chem. Soc.* **1970**, *92* (1), 219–220. <https://doi.org/10.1021/ja00704a047>.
- (155) Cowan, D. O.; LeVanda, C.; Park, J.; Kaufman, F. Organic Solid State. VIII. Mixed-Valence Ferrocene Chemistry. *Acc. Chem. Res.* **1973**, *6* (1), 1–7. <https://doi.org/10.1021/ar50061a001>.
- (156) Creutz, C.; Taube, H. Direct Approach to Measuring the Franck-Condon Barrier to Electron Transfer between Metal Ions. *J. Am. Chem. Soc.* **1969**, *91* (14), 3988–3989. <https://doi.org/10.1021/ja01042a072>.
- (157) Richardson, D. E.; Taube, H. Mixed-Valence Molecules: Electronic Delocalization and Stabilization. *Coord. Chem. Rev.* **1984**, *60*, 107–129. [https://doi.org/10.1016/0010-8545\(84\)85063-8](https://doi.org/10.1016/0010-8545(84)85063-8).
- (158) Parthey, M.; Kaupp, M. Quantum-Chemical Insights into Mixed-Valence Systems: Within and beyond the Robin–Day Scheme. *Chem. Soc. Rev.* **2014**, *43* (14), 5067–5088. <https://doi.org/10.1039/C3CS60481K>.
- (159) Demadis, K. D.; Hartshorn, C. M.; Meyer, T. J. The Localized-to-Delocalized Transition in Mixed-Valence Chemistry. *Chem. Rev.* **2001**, *101* (9), 2655–2686. <https://doi.org/10.1021/cr990413m>.
- (160) D'Alessandro, D. M.; Keene, F. R. Current Trends and Future Challenges in the Experimental, Theoretical and Computational Analysis of Intervalence Charge Transfer (IVCT) Transitions. *Chem. Soc. Rev.* **2006**, *35* (5), 424–440. <https://doi.org/10.1039/B514590M>.
- (161) Connelly, N. G.; Geiger, W. E. Chemical Redox Agents for Organometallic Chemistry. *Chem. Rev.* **1996**, *96* (2), 877–910. <https://doi.org/10.1021/cr940053x>.
- (162) Murata, Y.; Cheng, F.; Kitagawa, T.; Komatsu, K. Generation of Fullereryl Cation (EtO)<sub>2</sub>P+(OH)CH<sub>2</sub>-C<sub>60</sub><sup>+</sup> from RC<sub>60</sub>-H and from RC<sub>60</sub>-C<sub>60</sub>R (R = CH<sub>2</sub>P(O)(OEt)<sub>2</sub>). *J. Am. Chem. Soc.* **2004**, *126* (29), 8874–8875. <https://doi.org/10.1021/ja047483h>.
- (163) Meyer, K.; Bendix, J.; Bill, E.; Weyhermüller, T.; Wieghardt, K. Molecular and Electronic Structure of Nitridochromium(V) Complexes with Macrocyclic Amine Ligands. *Inorg. Chem.* **1998**, *37* (20), 5180–5188. <https://doi.org/10.1021/ic980302q>.
- (164) Orio, M.; Jarjayes, O.; Kanso, H.; Philouze, C.; Neese, F.; Thomas, F. X-Ray Structures of Copper(II) and Nickel(II) Radical Salen Complexes: The Preference of Galactose Oxidase for Copper(II). *Angew. Chem.* **2010**, *122* (29), 5109–5112. <https://doi.org/10.1002/ange.201001040>.
- (165) Dei, A.; Gatteschi, D.; Pardi, L.; Barra, A. L.; Brunel, L. C. Millimeter Band EPR Spectra Reveal Large Zero-Field Splittings in Copper(II)—Semiquinonato Complexes. *Chem. Phys. Lett.* **1990**, *175* (6), 589–592. [https://doi.org/10.1016/0009-2614\(90\)85586-2](https://doi.org/10.1016/0009-2614(90)85586-2).
- (166) Berreau, L. M.; Mahapatra, S.; Halfen, J. A.; Houser, R. P.; Young, V. G., Jr.; Tolman, W. B. Reactivity of Peroxo- and Bis(μ-Oxo)Dicopper Complexes with Catechols. *Angew. Chem. Int. Ed.* **1999**, *38* (1–2), 207–210. [https://doi.org/10.1002/\(SICI\)1521-3773\(19990115\)38:1/2<207::AID-ANIE207>3.0.CO;2-U](https://doi.org/10.1002/(SICI)1521-3773(19990115)38:1/2<207::AID-ANIE207>3.0.CO;2-U).
- (167) Esmael Balaghi, S.; Safaei, E.; Chiang, L.; Y. Wong, E. W.; Savard, D.; M. Clarke, R.; Storr, T. Synthesis, Characterization and Catalytic Activity of Copper(II) Complexes Containing a Redox-Active Benzoxazole Iminosemiquinone Ligand. *Dalton Trans.* **2013**, *42* (19), 6829–6839. <https://doi.org/10.1039/C3DT00004D>.
- (168) Pratt, R. C.; Stack, T. D. P. Intramolecular Charge Transfer and Biomimetic Reaction Kinetics in Galactose Oxidase Model Complexes. *J. Am. Chem. Soc.* **2003**, *125* (29), 8716–8717. <https://doi.org/10.1021/ja035837j>.

- (169) El-Bahraoui, J.; Wiest, O.; Feichtinger, D.; Plattner, D. A. Rate Enhancement and Enantioselectivity of the Jacobsen–Katsuki Epoxidation: The Significance of the Sixth Coordination Site. *Angew. Chem. Int. Ed.* **2001**, *40* (11), 2073–2076. [https://doi.org/10.1002/1521-3773\(20010601\)40:11<2073::AID-ANIE2073>3.0.CO;2-Y](https://doi.org/10.1002/1521-3773(20010601)40:11<2073::AID-ANIE2073>3.0.CO;2-Y).
- (170) Man, W.-L.; Kwong, H.-K.; Lam, W. W. Y.; Xiang, J.; Wong, T.-W.; Lam, W.-H.; Wong, W.-T.; Peng, S.-M.; Lau, T.-C. General Synthesis of (Salen)Ruthenium(III) Complexes via N···N Coupling of (Salen)Ruthenium(VI) Nitrides. *Inorg. Chem.* **2008**, *47* (13), 5936–5944. <https://doi.org/10.1021/ic800263n>.
- (171) Venkataramanan, N. S.; Kuppuraj, G.; Rajagopal, S. Metal–Salen Complexes as Efficient Catalysts for the Oxygenation of Heteroatom Containing Organic Compounds—Synthetic and Mechanistic Aspects. *Coord. Chem. Rev.* **2005**, *249* (11), 1249–1268. <https://doi.org/10.1016/j.ccr.2005.01.023>.
- (172) Daly, A. M.; Renehan, M. F.; Gilheany, D. G. High Enantioselectivities in an (E)-Alkene Epoxidation by Catalytically Active Chromium Salen Complexes. Insight into the Catalytic Cycle. *Org. Lett.* **2001**, *3* (5), 663–666. <https://doi.org/10.1021/ol0069406>.
- (173) Daly, A. M.; Cormac Dalton, T.; Renehan, M. F.; Gilheany, D. G. Unsymmetrical Salen Ligands: Synthesis and Use in Chromium Mediated Asymmetric Epoxidation. *Tetrahedron Lett.* **1999**, *40* (18), 3617–3620. [https://doi.org/10.1016/S0040-4039\(99\)00489-X](https://doi.org/10.1016/S0040-4039(99)00489-X).
- (174) Blackman, A. G.; Schenk, E. B.; Jelley, R. E.; Krenske, E. H.; Gahan, L. R. Five-Coordinate Transition Metal Complexes and the Value of T5: Observations and Caveats. *Dalton Trans.* **2020**, *49* (42), 14798–14806. <https://doi.org/10.1039/D0DT02985H>.
- (175) Addison, A. W.; Rao, T. N.; Reedijk, J.; Rijn, J. van; Verschoor, G. C. Synthesis, Structure, and Spectroscopic Properties of Copper(II) Compounds Containing Nitrogen–Sulphur Donor Ligands; the Crystal and Molecular Structure of Aqua[1,7-Bis(N-Methylbenzimidazol-2'-yl)-2,6-Dithiaheptane]Copper(II) Perchlorate. *J. Chem. Soc. Dalton Trans.* **1984**, No. 7, 1349–1356. <https://doi.org/10.1039/DT9840001349>.
- (176) Johnson, S. I.; Heins, S. P.; Klug, C. M.; Wiedner, E. S.; Bullock, R. M.; Raugei, S. Design and Reactivity of Pentapyridyl Metal Complexes for Ammonia Oxidation. *Chem. Commun.* **2019**, *55* (35), 5083–5086. <https://doi.org/10.1039/C9CC01249D>.
- (177) Xue, X.-S.; Ji, P.; Zhou, B.; Cheng, J.-P. The Essential Role of Bond Energetics in C–H Activation/Functionalization. *Chem. Rev.* **2017**, *117* (13), 8622–8648. <https://doi.org/10.1021/acs.chemrev.6b00664>.
- (178) Wang, Z.-S.; Zhu, L.-J.; Li, C.-T.; Liu, B.-Y.; Hong, X.; Ye, L.-W. Synthesis of Axially Chiral N-Arylindoles via Atroposelective Cyclization of Ynamides Catalyzed by Chiral Brønsted Acids. *Angew. Chem. Int. Ed.* **2022**, *61* (20), e202201436. <https://doi.org/10.1002/anie.202201436>.
- (179) Croft, R. A.; Mousseau, J. J.; Choi, C.; Bull, J. A. Structurally Divergent Lithium Catalyzed Friedel–Crafts Reactions on Oxetan-3-Ols: Synthesis of 3,3-Diaryloxetanes and 2,3-Dihydrobenzofurans. *Chem. – Eur. J.* **2016**, *22* (45), 16271–16276. <https://doi.org/10.1002/chem.201604031>.

## Appendix A. Supporting Information for Chapter 2

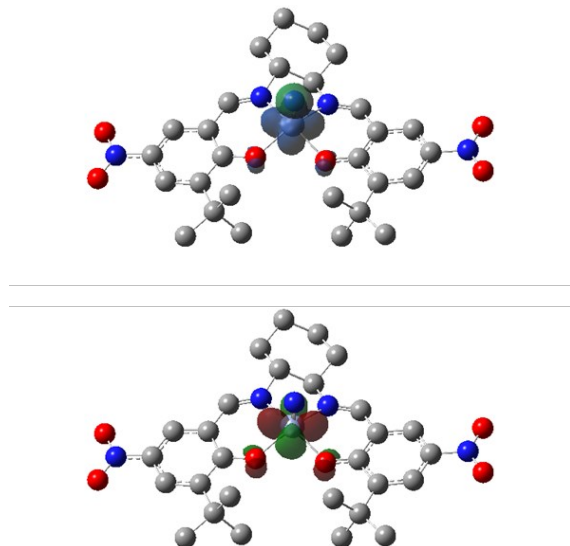


Figure A.1. Spin density (top) and SOMO (bottom) plots for CrNSal<sup>NO2</sup>.

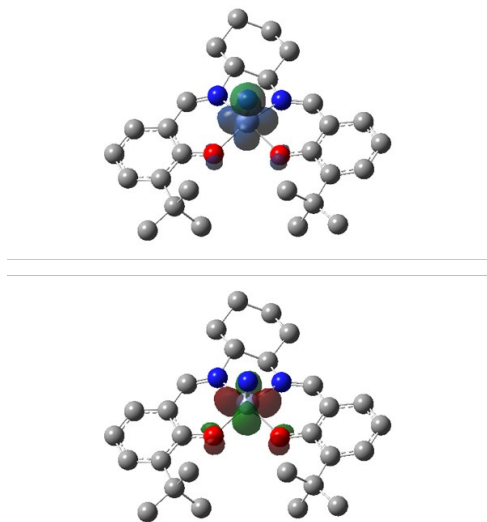


Figure A.2. Spin density (top) and SOMO (bottom) plots for CrNSal<sup>H</sup>.

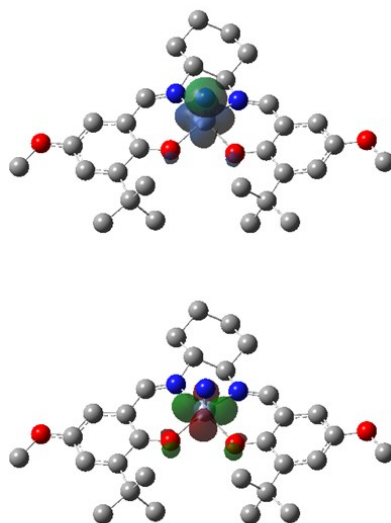


Figure A.3. Spin density (top) and SOMO (bottom) plots for CrNSal<sup>OMe</sup>.

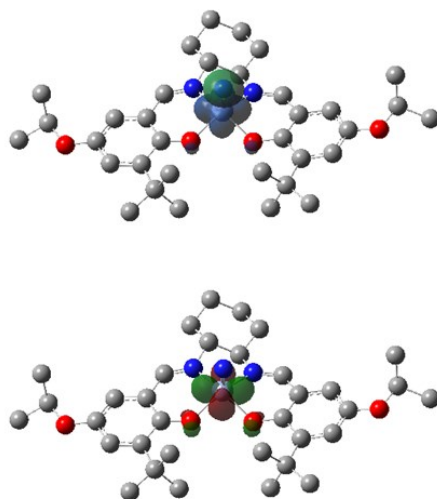


Figure A.4. Spin density (top) and SOMO (bottom) plots for CrNSal<sup>OIPr</sup>.

## Appendix B. Supporting Information for Chapter 3

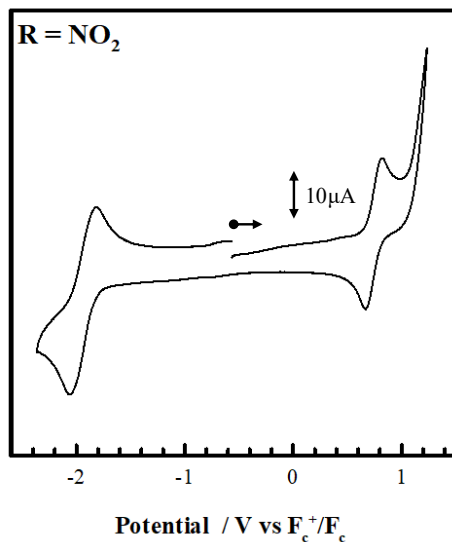


Figure B.1. Full scan window cyclic voltammogram for CrNSal<sup>NO2</sup>. Conditions: 0.1 M TBAP; CH<sub>2</sub>Cl<sub>2</sub>; 1 mM complex; T = 298 K; scan rate = 100 mV/s.

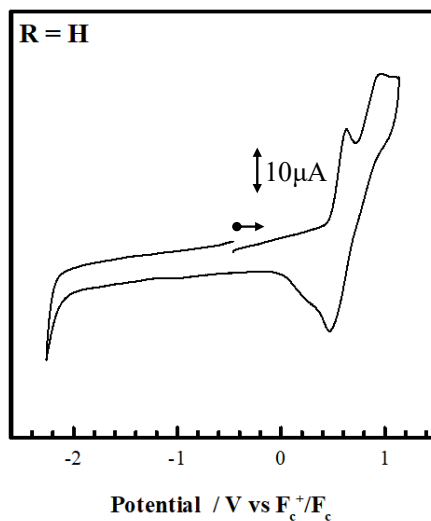


Figure B.2. Full scan window cyclic voltammogram for CrNSal<sup>H</sup>. Conditions: 0.1 M TBAP; CH<sub>2</sub>Cl<sub>2</sub>; 1 mM complex; T = 298 K; scan rate = 100 mV/s.

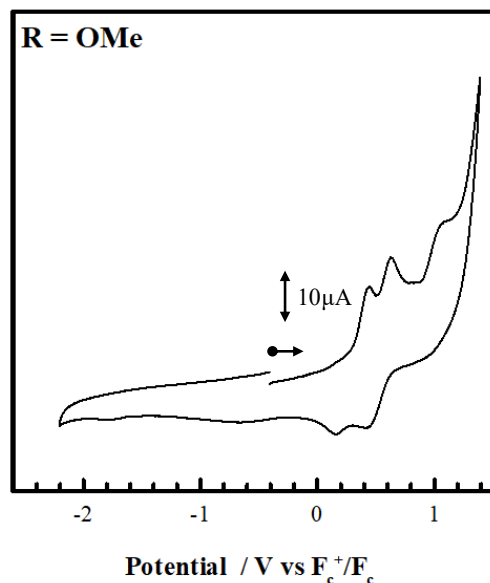


Figure B.3. Full scan window cyclic voltammogram for CrNSal<sup>OMe</sup>. Conditions: 0.1 M TBAP; CH<sub>2</sub>Cl<sub>2</sub>; 1 mM complex; T = 298 K; scan rate = 100 mV/s.

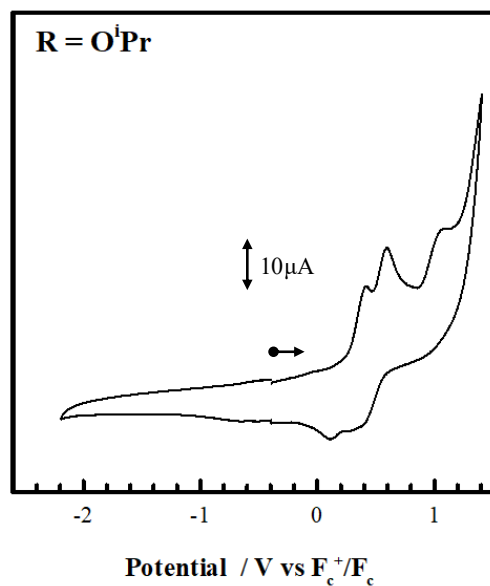


Figure B.4. Full scan window cyclic voltammogram for CrNSal<sup>O<sup>i</sup>Pr</sup>. Conditions: 0.1 M TBAP; CH<sub>2</sub>Cl<sub>2</sub>; 1 mM complex; T = 298 K; scan rate = 100 mV/s.

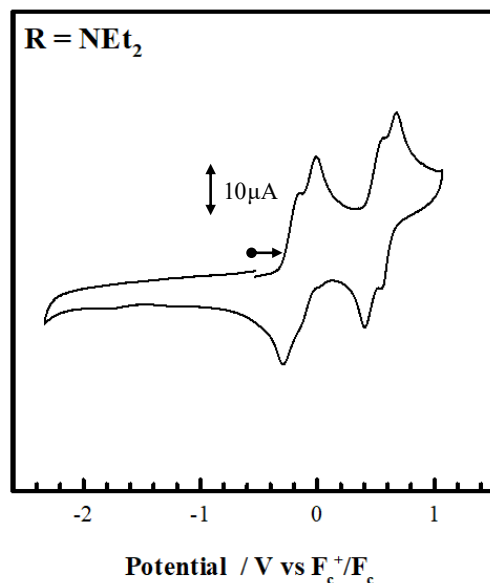


Figure B.5. Full scan window cyclic voltammogram for  $\text{CrNSal}^{\text{NEt}_2}$ . Conditions: 0.1 M TBAP;  $\text{CH}_2\text{Cl}_2$ ; 1 mM complex;  $T = 298 \text{ K}$ ; scan rate = 100 mV/s.

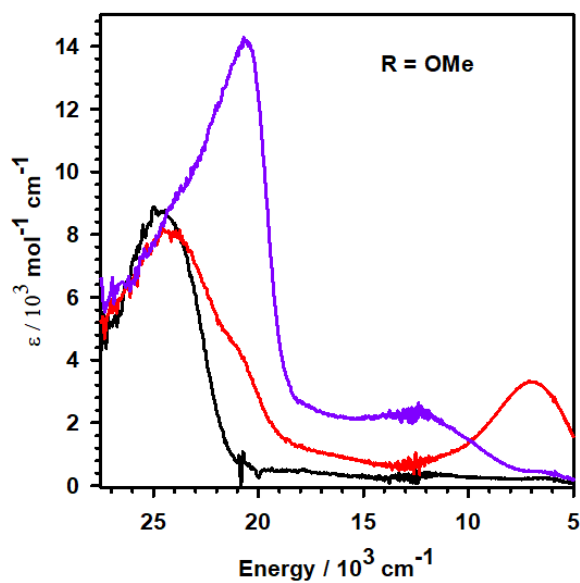


Figure B.6. UV-vis-NIR spectra for chemically oxidized  $\text{CrNSal}^{\text{OMe}}$ . Black = neutral; red = mono-oxidized; purple = bis-oxidized. Conditions: 0.45 mM  $\text{CrNSal}^{\text{OMe}}$ ;  $\text{CH}_2\text{Cl}_2$ ;  $T = 253 \text{ K}$ .



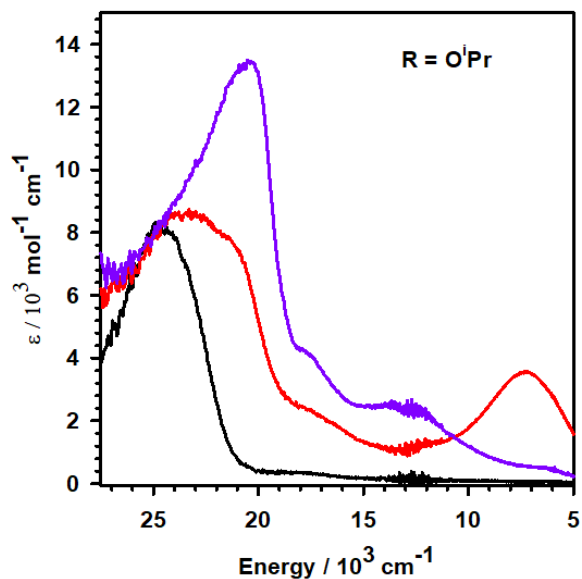


Figure B.7. UV-vis-NIR spectra for chemically oxidized CrNSal<sup>O<sup>iPr</sup></sup>. Black = neutral; red = mono-oxidized; purple = bis-oxidized. Conditions: 0.45 mM CrNSal<sup>O<sup>iPr</sup></sup>; CH<sub>2</sub>Cl<sub>2</sub>; T = 253 K.

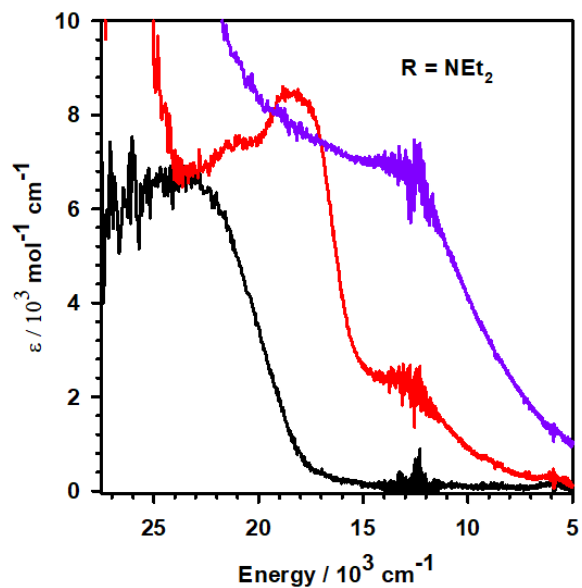
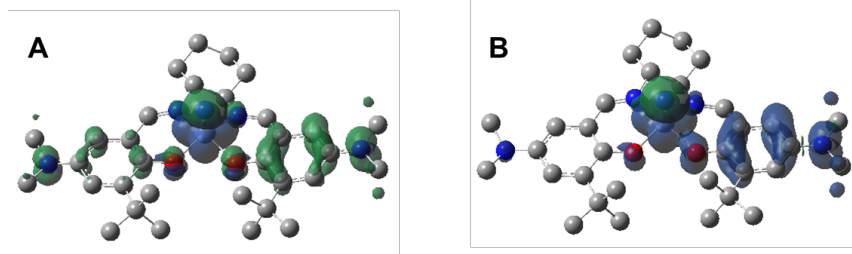


Figure B.8. UV-vis-NIR spectra for chemically oxidized CrNSal<sup>NEt<sub>2</sub></sup>. Black = neutral; red = mono-oxidized; purple = bis-oxidized. Conditions: 0.45 mM CrNSal<sup>NEt<sub>2</sub></sup>; CH<sub>2</sub>Cl<sub>2</sub>; T = 253 K.



**Figure B.9.** Spin density plots for oxidized CrNSal<sup>NMe<sub>2</sub></sup> in the BSS (A) and triplet (B) spin states.

## Appendix C. Supporting Information for Chapter 4

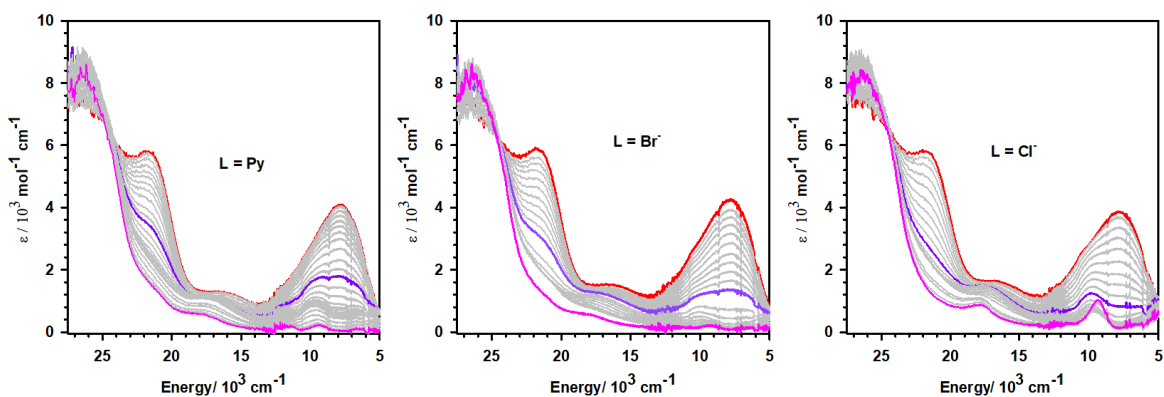


Figure C.1. Titration of two equivalents of pyridine, bromide, and chloride into  $[\text{CrNSal}^{\text{tBu}}]^+$  monitored by UV-vis-NIR spectroscopy. Red = no ligand; purple = one equivalent ligand; magenta = two equivalents of ligand; grey = intermediate scans. Conditions: 0.1 mM  $[\text{CrNSal}^{\text{R}}]^+$ ; T = 253 K;  $\text{CH}_2\text{Cl}_2$ .

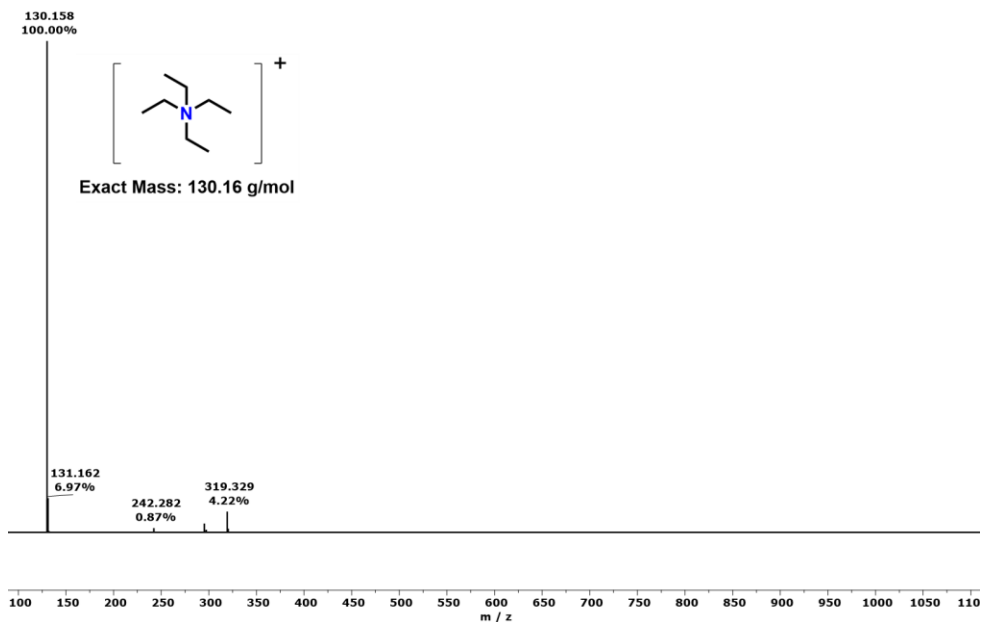
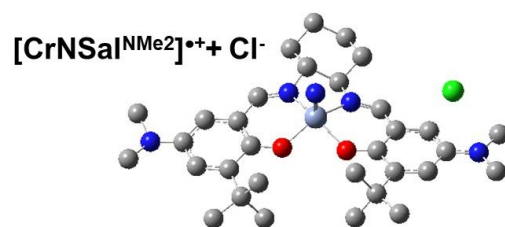


Figure C.2. Positive mode ESI-MS spectrum of reaction between  $[\text{CrNSal}^{\text{tBu}}]^+$  and tetraethylammonium chloride.



**Figure C.3.** Attempt to generate an optimized structure of  $[\text{CrNSa}^{\text{NMe}_2}]^{2+}$  with  $\text{Cl}^-$  bound axially. An optimization was first performed with the Cr-Cl bond locked at 2.9Å, then unlocked.

## Appendix D. Supporting Information for Chapter 5

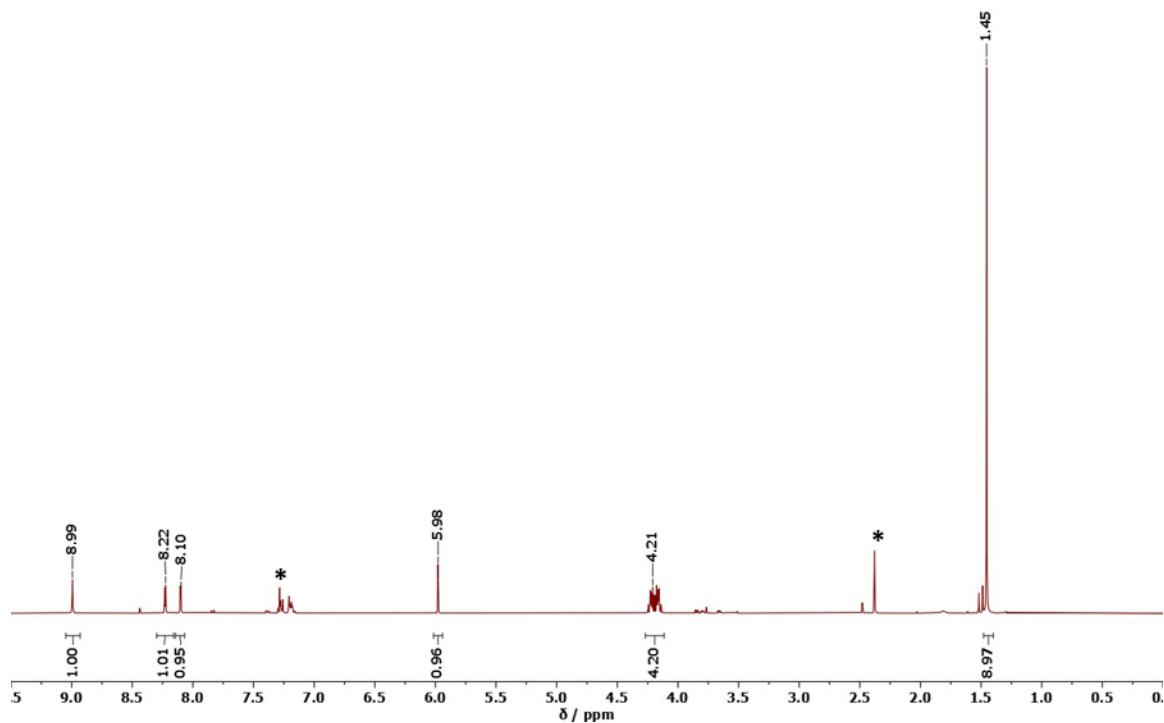


Figure D.1. <sup>1</sup>H NMR spectrum of 2-(tert-butyl)-6-(1,3-dioxolan-2-yl)-4-nitrophenol in CDCl<sub>3</sub>. \* = residual solvent.

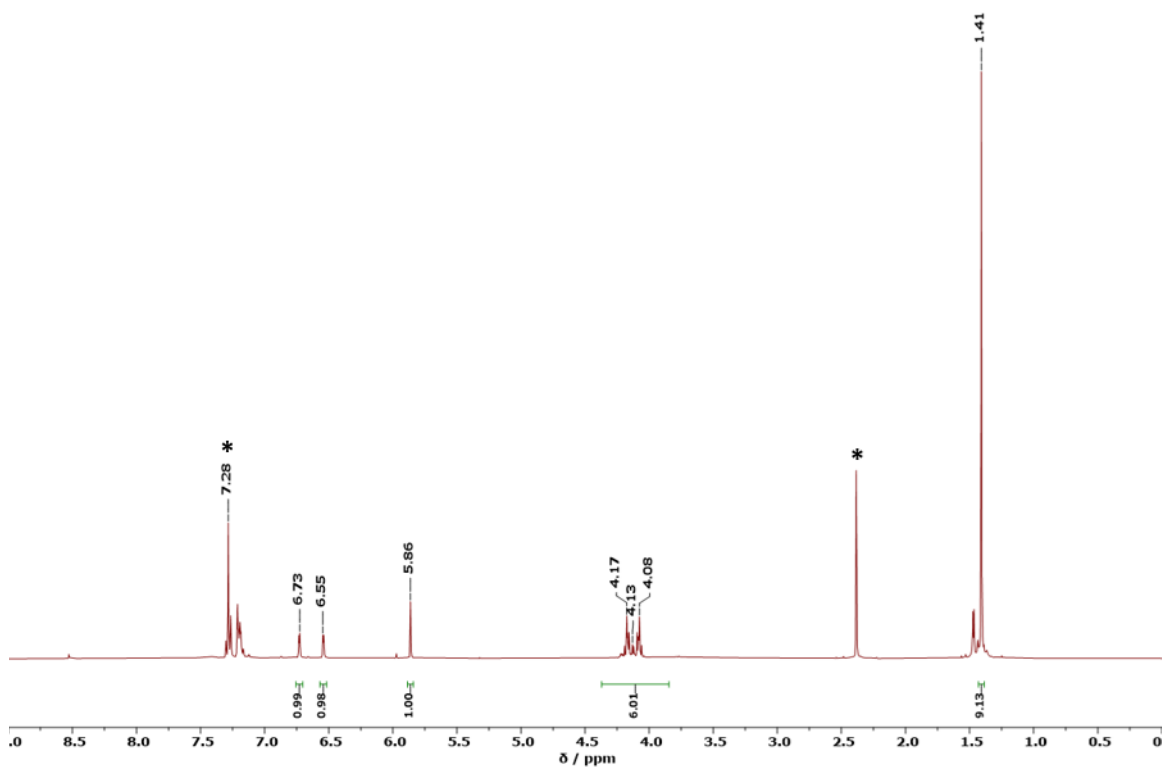


Figure D.2.  $^1\text{H}$  NMR spectrum of 4-amino-2-(tert-butyl)-6-(1,3-dioxolan-2-yl)phenol in  $\text{CDCl}_3$ . \* = residual solvent.

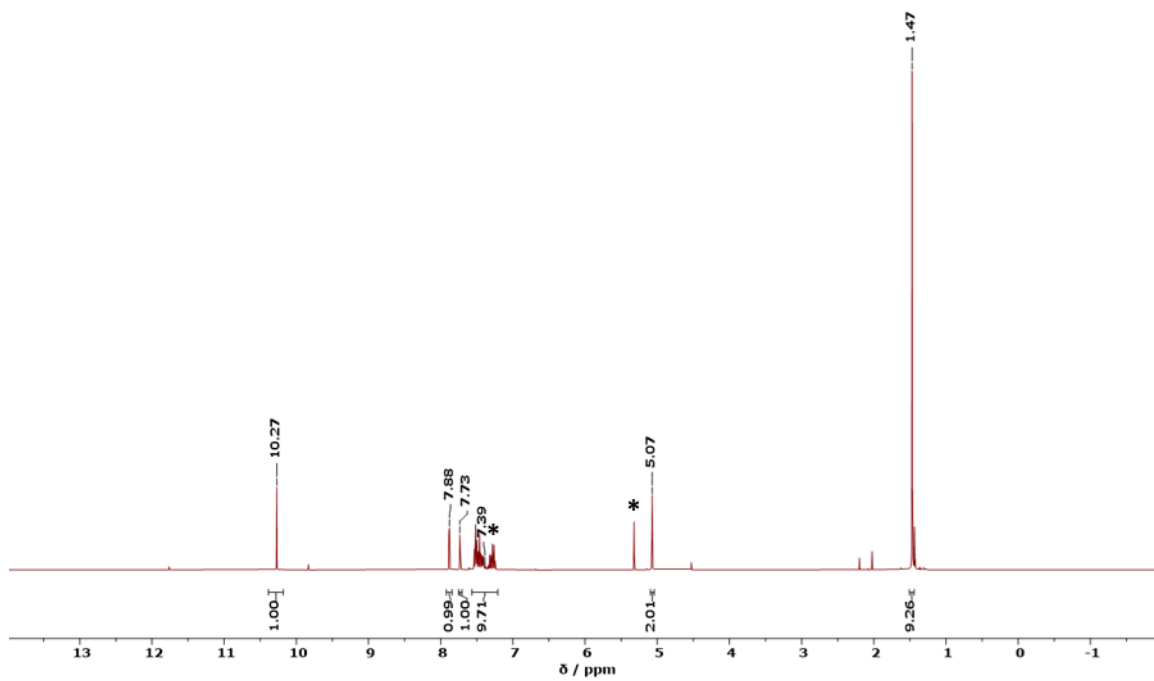


Figure D.3. <sup>1</sup>H NMR spectrum of 2-(benzyloxy)-5-bromo-3-(tert-butyl)benzaldehyde in CDCl<sub>3</sub>. \* = residual solvent.